

ÁDÁM LÁSZLÓ GERA
FINAL PROJECT

BUDAPEST UNIVERSITY OF TECHNOLOGY AND ECONOMICS
DEPARTMENT OF APPLIED MECHANICS



FINAL PROJECT

BUDAPEST UNIVERSITY OF TECHNOLOGY AND ECONOMICS

ÁDÁM LÁSZLÓ GERA

FINAL PROJECT

Reliability of Multiwire proportional chambers in field measurements: thermal and mechanical limits

Supervisor
Bálint Magyar
Assistant professor

Advisor
Dezső Varga
Scientific advisor

Budapest, 2020



Budapest University of Technology and Economics

Faculty of Mechanical Engineering

Department of Applied Mechanics

<http://www.mm.bme.hu/>


FINAL PROJECT ASSIGNMENT

Publicly Available

Identification	Name: Gera Ádám László		ID: 73240216059	
	Code of the Curriculum: 2N-MW0		Specialisation:	Document ref. number:
	Curriculum: Gépészeti modellezés mesterképzési szak		2N-MW0-SM	GEMM:2020-1:2N-MW0:QIZ4M0
	Final Project issued by: Department of Applied Mechanics		Final exam organised by: Department of Applied Mechanics	
	Supervisor: Dr. Bálint Balázs Magyar (71949870698), assistant professor			

Project Description	Title	Reliability of multiwire proportional chambers in field measurements: thermal and mechanical limits Sokszálas kamrák megbízhatósága a terepen, hő- és mechanikai igénybevételek hatása a rendszerre
	Details	<ol style="list-style-type: none">1. Introduce the imaging technique with cosmic rays.2. Present the construction and measurement with the REGARD group detectors.3. Investigating the effects of environmental parameters.4. Study the properties of the two-component epoxy adhesive.5. Simulate and test the vibration effects during transportation.6. Summarize the results in English and in Hungarian. Prepare a poster presentation of the work.
	Advisor	Advisor's Affiliation: Wigner Fizikai Kutatóközpont 1121 Budapest, Konkoly-Thege Miklós út 0 Advisor: VARGA Dezső, Group leader

Final Exam	1 st subject (group)	2 nd subject (group)	3 rd subject (group)	4 th subject (group)
	ZVEGEMMMW02 Finite Element Analysis	ZVEGEMMMW03 Continuum Mechanics	ZVEGEMMMW06 Nonlinear Vibrations	ZVEGEMMMW05 Elasticity and Plasticity

Authentication	Handed out: 15 September 2020		Deadline: 11 December 2020			
	Compiled by: Dr. Bálint Balázs Magyar (71949870698) Supervisor		Verified by: Dr. Tamás Insperger (signed) Head of Department		Approved by: Dr. Péter Bihari (signed) Vice-Dean	
	The undersigned declares that all prerequisites of the Final Project have been fully accomplished. Otherwise, the present assignment for the Final Project is to be considered invalid. Gera Ádám László					

STUDENT DECLARATION

I, Ádám László Gera, the undersigned, hereby declare that the present thesis work has been prepared by myself without any unauthorized help or assistance such that only the specified sources (references, tools, etc.) were used. All parts taken from other sources word by word or after rephrasing but with identical meaning were unambiguously identified with explicit reference to the sources utilized.

I authorize the Faculty of Mechanical Engineering of the Budapest University of Technology and Economics to publish the principal data of the thesis work (author's name, title, abstracts in English and in Hungarian, year of preparation, supervisor's name, etc.) in a searchable, public, electronic and online database and to publish the full text of the thesis work on the internal network of the university (or for authenticated users). I declare that the submitted hard copy of the thesis work and its electronic version are identical. Full text of thesis works classified upon the decision of the Dean will be published after two years.

Done at Budapest, 01.12.2020

Sign

A handwritten signature in blue ink, appearing to read 'Gera Ádám', is written below the 'Sign' label.

Contents

Abstract	vii
Used notations	viii
1. Introduction.....	1
1.1. Different applications of an imaging technique with cosmic-rays	2
2. The REGARD detectors	9
2.1. The principles of muography	9
2.2. Catching muons: the measurement of ionizing particles.....	10
2.3. The Hungarian-Japanese collaboration	13
2.4. Large MWPC for muography	14
2.5. The construction of the chambers.....	18
2.6. Cosmic muon detection with REGARD MWPCs.....	23
3. The effects of the environmental parameters	26
3.1. The properties of the gain.....	26
3.2. The effect of the environmental parameters	30
3.2.1. First measurements with our system.....	30
3.2.2. Temperature dependence of the electrical components.....	31
3.2.3. Effect of temperature, pressure and the current on the chambers	36
4. The properties of the glue.....	49
4.1. Basics of adhesives.....	49
4.2. Testing of different adhesives	52
4.3. The testing of UVERAPID 5 with different mixing ratios	55
4.4. Testing the UVERAPID 5 with different materials.....	58
5. Study of vibration effects during transportation	61
5.1. Modal testing of one chamber.....	63
5.2. Simulation of the transportation with random vibration	71
5.2.1. Modal analysis.....	71
5.2.2. Random Vibration	75
5.2.3. Comparison of results from the tensile test and the vibration simulation	80
6. Summary.....	82
6.1. Outlook.....	83
7. Összefoglalás.....	84
8. References	85
9. Appendix	90

ABSTRACT

The first effective multiwire proportional chamber (MWPC) was developed and operated in 1967-68 at the European Organization for Nuclear Research (CERN) by George Charpak. This important discovery successfully replaced the bubble chambers in the experiments with its good time and space resolution and also opened new paths for application. One of the main outcome was the birth of imaging techniques to get information from inside of a physical non-transparent object. For example, muon radiography or just muography, which uses the energy loss of the particle muon to make this image.

In 1965 Louis Alvarez investigated the Chefren's Pyramid with this technique. Nowadays with the evolution of technology, the muography is applied to study caves, mountains and active volcanoes. The REGARD group is focused on the research and development of gaseous detectors through Charpak's idea which resulted the usage of the MWPCs as the core element of an imaging system. The Hungarian-Japanese collaboration helped to establish the Multiwire proportional chamber-based Muon Observatory System (MMOS) in Japan near the Sakurajima volcano which is a member of the Decade Volcanoes. This few years of work during the upgrade of the MMOS brought us a lot of experiences in this area including the possible limits of the system. This thesis aims to investigate the effects of the environmental parameters to our chambers and the effectiveness in a mechanical sense of the used adhesive.

* * *

I would like to express my gratitude to my advisor Dezső Varga for all the guidance and technical background and to my supervisor Bálint Magyar for all the help with my thesis and the support in the mechanical measurements, without them this thesis would not be realized. Also I want to mention my colleagues Gergő Hamar and Gábor Nyitrai and thank to them for the fruitful discussions and support. I would like to express my gratitude to my family for the endless encouragement and assist. I would like to thank to Gábor Szabó and Szabolcs Pántya for the opportunity to measure in the department of polymer engineering.

1 December 2020 ,Budapest

Ádám László Gera

USED NOTATIONS

Latin letters

Notation	Description	Unit
E	Electric field strength	N/C
p	Pressure	bar
r	Radius	m
N	Number of electrons	1
G	Gain	1
T	Temperature	Kelvin
I	Current	A
U	Voltage	V
Q	Gas flow	l/h
t	Time or time-bin	s or min
m	Mass	kg
s	Stiffness	N/m
c	Damping coefficient	Ns/m
D	Damping ratio	1

Greek letters

Notation	Description	Unit
α	First Townsend coefficient	1
ρ	Density	kg/m ³
λ	Linear charge density	C
ϵ_0	Vacuum permittivity	F/m
κ	Correction factor of the current	1
η	Correction factor of the temperature and pressure	1

1. INTRODUCTION

The famous experiment of Victor Francis Hess in 1912 proved the existence of cosmic rays. In the beginning of the 20th century the scientists thought that the Earth is the main source of the radiations and with distance it would decrease. Hess successfully reached 5350 m and with his measurements showed that the radiation is about twice as much as on the surface [1]. Later Robert Andrews Millikan confirmed the state that radiation is coming from outer space and gave the name „cosmic-rays“. For these efforts Hess won a Nobel Prize in 1936 and at the same time muons were discovered by Carl D. Anderson and Seth Neddermeyer at Caltech [2]. A few more decades later, with the investigation of cosmic-rays and their properties, the ideas of possible applications started to spread such as imaging techniques.

My project aims to investigate the reliability of our muography system including the chambers and the electronics. First, in a mechanical sense, there are vibrations and stresses during transportation and the presence of pressure due to its operation principle. Second, in an environmental sense which means the constant (sometimes rapid) changing of the temperature, outer pressure and humidity. The changing of these parameters have direct and indirect effects on electron gain, nominal voltage and current. The investigation will result in a much more plannable and secure system against extreme conditions.

I would like to show how the discovery of cosmic-rays ended up with muography with different detector technologies in the first section. This is continued by the principles of muography and the development of REGARD detectors for volcano monitoring. After that, I will show the properties of gain, and the effect of temperature and pressure to our system will be investigated with different measurements. In the next step, different adhesives and joints will be tested, and the effect of the mixing ratio to

the tensile strength will be discussed for the currently used glue. Then the modal testing of the chamber will be performed for validating the finite element simulation. In the last step I will simulate the random vibration and its effect to the chamber, after that the results will be compared to the tensile test results assuming a conservative approach.

1.1. Different applications of an imaging technique with cosmic-rays

The first idea was in 1965, when Luis W. Alvarez sent a proposal to a representative group of cosmic-ray physicists and archaeologists, with the idea to search for hidden chambers in the Pyramids via cosmic-ray absorption. The curiosity came from the fact that Chephren's pyramid compared to his father's, Cheop's pyramid is much simpler. The archaeologists simply explained this in terms of „period of experimentation“, however Alvarez had a different theory in mind. His concept for the sudden decrease in internal complexity was about the architect's success in hiding the upper chambers. In the early 19th-century investigators tried to locate new chambers by hole blasting with gunpowder, on the other hand the damage it caused in the Pyramids is a high disadvantage. The favourable response to the proposal led to the installation of cosmic-ray detectors in the Belzoni Chamber in 1966. Figure 1 shows the measurement setup.

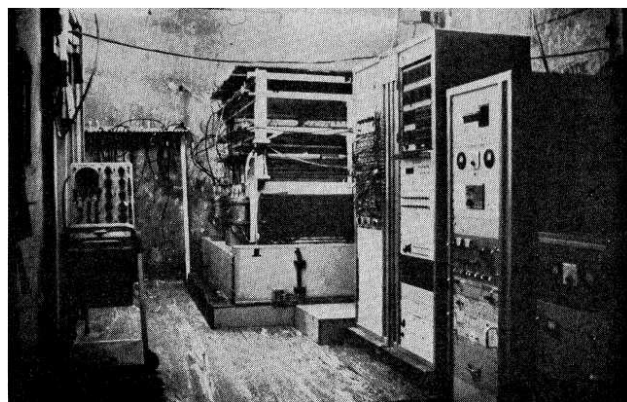


Figure 1. The measurement equipment in the Belzoni Chamber under Chephren's pyramid [3].

Several months of operation with active detector area of 4 m² showed, that no chambers with volumes similar to the already known chambers exist [3].

Another possible application is to explore the inner-structure of gigantic geophysical substances, for example a throat of a volcano. In 1994 K.Nagamine investigated the Mt. Tsukuba with a simple and inexpensive detection system consist of plastic scintillators and successfully tested his equipment. The measurement involved three plastic scintillation counters which detected the near-horizontal cosmic-ray muons passing through the mountain. The schematic setup can be seen on Figure 2.

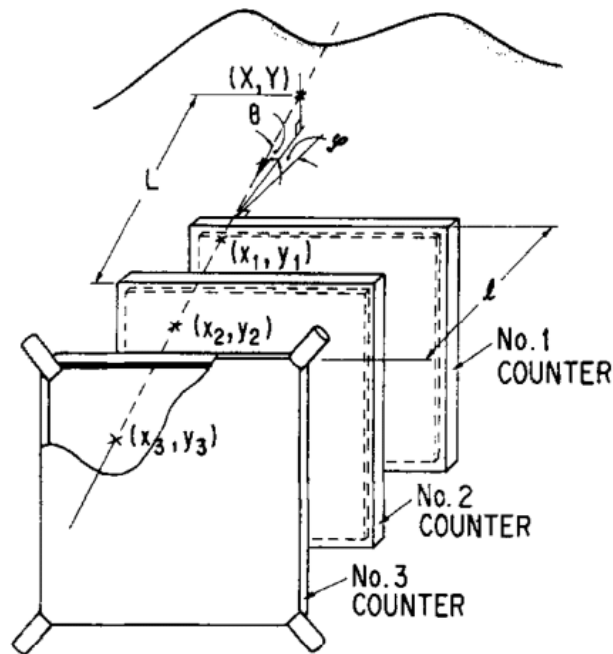


Figure 2. The muon telescope with three plastic scintillator Nagamine used for the investigation of Mt. Tsukuba [4].

Although this mountain is not volcanic, they proposed an idea to use this method in the perspective for volcanic eruption predictions. The possible change in the density along the magma channel can be observed and estimated quantitatively by cosmic muons. With an expanded system and proper spatial resolution an anomaly of few per-

cent in a specified structure can be detected in a few days. This time-dependence measurement suggests a powerful, new prediction method for volcanic activities instead of conventional electromagnetic or seismic techniques [4]. A decade later H. Tanaka with the assistance of Nagamine managed to develop the system with the use of iron absorbers and performed measurements on Mt. Asama. The absorber was important in terms of decreasing the background (noise) and enabled to reduce the detector number from three to two. Figure 4 shows the setup. They confirmed the ability of long-term observation during a 3-month measurement period and also the density of the volcano with 30% accuracy [5].

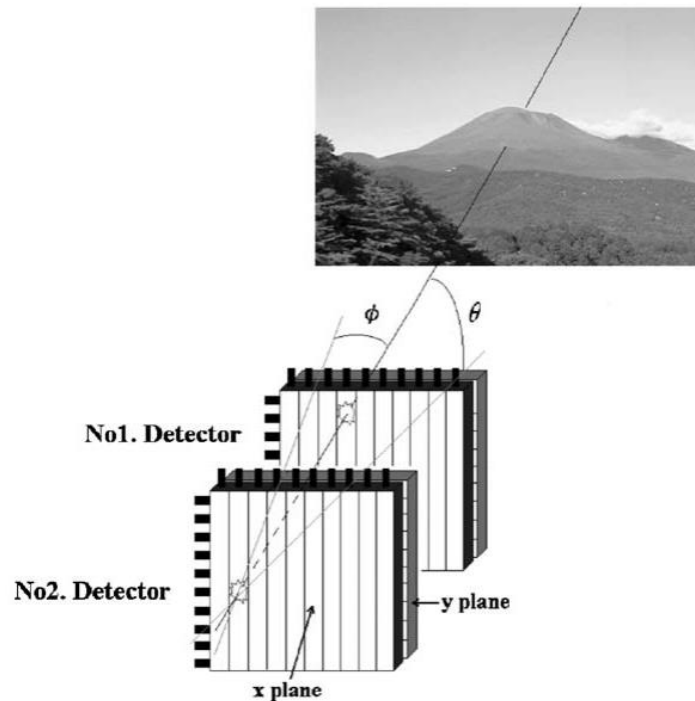


Figure 4. The segmented detector system with two scintillators that was used for Mt. Asama [5]. The two important angles for these detectors are the azimuth φ and zenith θ .

Due to the reliability of the system, muon radiography has been studied in Mt. West Iwate for a 1-year observation period. Tanaka could determine the average density

with 10% precision which was in agreement with gravimetric measurements. Movements of magma have been observed and they wanted to move towards the area of eruption dynamics with further development of the system [6]. To create more highly resolved images in a shorter observation period, a closer measurement place to the crater is necessary, although normal electric power in these area is not available in general. They developed a simple emulsion cloud chamber (ECC) [11] which is a completely power-free particle tracking device and the spatial resolution is also higher than with scintillation detectors. The total detection area was 0.4 m² and the observation has been performed from August to October in 2006. The ECC can be used to measure cosmic-ray muons and the density could be determined with 5 % accuracy [7]. These successful measurements motivated the further collaboration between particle physics and geophysics. On the other hand, to image a larger volcano in shorter time, a larger detector needed to collect muon events, because the area is proportional to the time required for imaging. In 2009 Tanaka investigated the Mt. Iwodake volcano to get information about the density distribution. A quite similar plastic scintillator was used as in the case of Mt. Asama, but the area was 1 m². Through a one-month period of measurement the system collected more than 1 million event and they managed to distinguish the lava from the rock. Also the density was given with around 3% accuracy [8]. The density map can be seen on Figure 5.

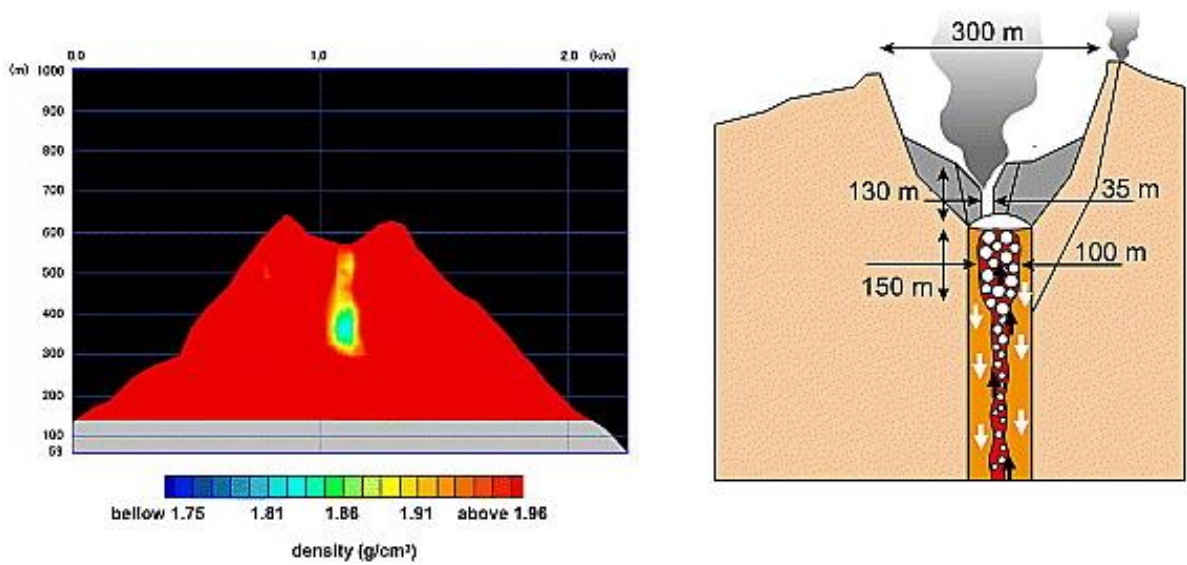


Figure 5. The average density map of Mt. Iwodake. The magma can be clearly distinguished from the rock [8].

In parallel, after Alvarez's experiment Charpak and collaborators at [CERN](#) successfully operated the first effective multiwire proportional chambers. They used the stacking of many independent counters, which was previously feared due to its mechanical difficulties. In the late 1970s the operation and properties of these kind of detectors were well known. Namely the effect of different gas mixtures, the proper geometrical parameters, the attributes of the electric field and gain (the ratio of the number of detected electrons to the electrons produced in ionization by the charged particle) [9]. They started to use in High Energy Physics (HEP) as a replacement of bubble chambers. The improvement of electronics implied to have a detector with fast read-out. After a few decades in 2009 the world-wide RD51 collaboration were initiated by CERN with common goals, information sharing and tests in common facilities to develop new gaseous detectors [10]. Among the founders we can find the Eötvös Loránd University (ELTE) and Research Institute for Particle and Nuclear Physics (MTA RMKI) and with their collaboration the REGARD (RMKI ELTE Gaseous detector Research and Development) group was formed in Hungary. Their focus was the basic

research and applications of multiwire chambers based on Charpak's results. Dezsó Varga and Gergő Hamar studied an asymmetric-type MWPC prototype for one of the biggest CERN experiments, ALICE (A Large Ion Collider Experiment) detector system. The reasonable advantages of the system were the low material budget and stable operation with optimal settings. They also studied the system on different wire voltages and the effect of wire positioning [12]. This modified multiwire chamber called „Close Cathode Chamber” later also used for investigating underground caves due to the proper position resolution. A measurement device for the field must have important features such as portability, detection efficiency, low energy consumption and relatively low cost. For the appropriate statistics the sensitive area must be as large as it can be, although natural caves are often hard to access and it limits the size. The geophysical interest implied to investigate the Ajándék cave in Pilis Mountain, Hungary and therefore a setup with $51 \times 46 \times 32 \text{ cm}^3$ dimensions and 13 kg weight resulted a relatively easy manual handling as Figure 6 shows.

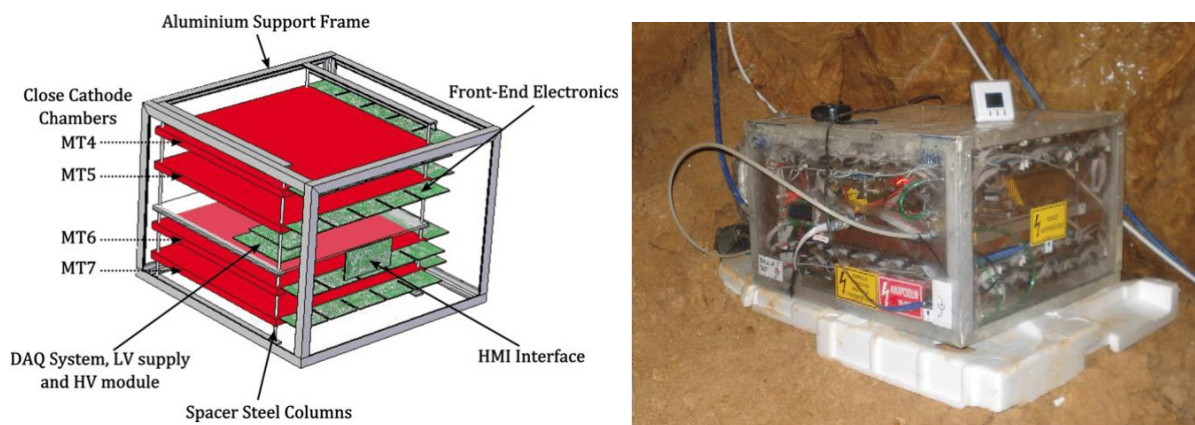


Figure 6. The structure of the Muontomograph consists CCCs (left) and the actual device in the Ajándék Cave (right) [13].

During the 50 days long measurement, they collected 170,000 events with well identifiable muon tracks. The system could determine the two dimensional angular distribution map which allowed tomographic mapping. The power consumption was only

5 W and the gas consumption, which is necessary to the operation, only 3-4 l/h in extremely humid environment (100%). After the analysis, no evidence was found for unknown cave above the detector [13]. Simultaneously classical type of MWPCs were also developed for educational purposes with low cost and relatively easy construction. These smaller detectors have shown great efficiency and it was a springboard for larger versions that can be the soul of a muon telescope [14].

2. THE REGARD DETECTORS

2.1. *The principles of muography*

As Millikan stated the cosmic-rays or more accurately primary cosmic-rays are originated from outer space from astronomical objects such as the Sun or galaxies. They generally consist of hadrons, mainly protons and alpha particles, however heavier nuclei can also show up. After entering the Earth's atmosphere, through collision with other elements they create secondary particles. Three major components can be distinguished in the atmosphere, namely the hadronic-, the photon-electron and the muon component as Figure 7 shows. In the case of muography the third component is involved and can be a promising technique due to the relatively long life time (10^{-6} s) and penetrating power of muons. The penetration flux is only influenced by the density and the length along the trajectory which means, that only muons with high energy can go through a denser geological object [15]. As mentioned before Japanese scientist relied on the near-horizontal muons that went over the mountain. The reason is the difference between the open-sky spectrum (when muons only interact with the atmosphere elements) and the actual measurement, which is in direct connection with the amount of matter along the path. This simply means, that thickness will determine the number of muons passing through the object of interest. On the other hand, we have to deal with the so called "background noise" which consists of the other components of cosmic rays and particles, that did not go over the investigated target. Later, one of the possible methods will be given in detail which used by the REGARD group.

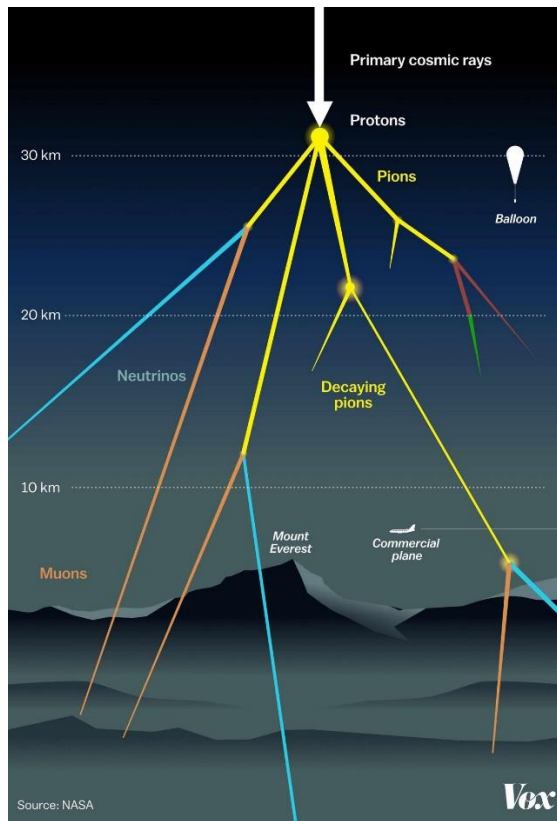


Figure 7. The development of the air shower from primary cosmic ray (Source: Javier Zarracina/Vox;NASA).

2.2. *Catching muons: the measurement of ionizing particles*

It is well-known, when a charged particle flies through a specified gas, there is chance that electron-ion pairs will be created. The number depends on the type of gas, for example in 1 cm layer of argon, around 120 ion pairs created. Although, this is extremely far from the possibility of detection because the signal is not strong enough. It is the reason, why the Townsend avalanche is important which can boost this signal by several orders of magnitude. Let us consider a thin metal wire which is stretched in the axis of a cylindrical gas volume. Applying positive voltage on the wire (anode), the electric field will move the charged particles towards the anode and the ions towards the cathode. Due to its thickness, the field can be really strong near the anode. Very close to it (few wire radii) the particles can have enough energy to release another

electron. The number of electrons increases exponentially along the path of the electrons and this multiplication process is called the Townsend avalanche as Figure 8 shows. This important effect is the soul of gaseous detectors with boosting the initially weak signal to a detectable level. In general, the avalanche can take place in any kind of gas or gas mixture used in the detector, although some parameters corresponding to the usage of the system can restrict the choice on the operating gas. These requirements can be for example working voltage, the level of gain, lifetime, environmental conditions, rate capability, size, etc. [9].

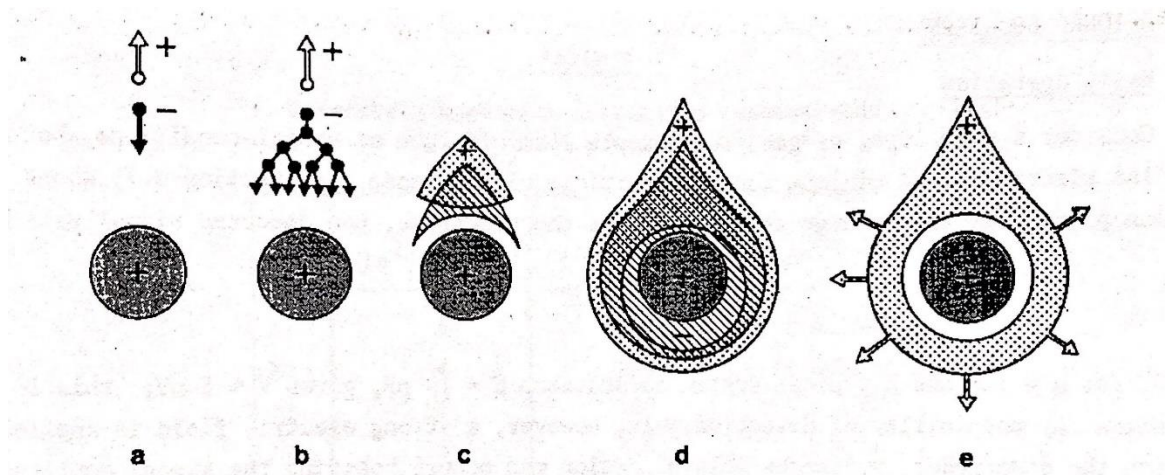


Figure 8. The development of the electron avalanche around a thin anode wire. After the electrons are collected a cloud of slowly migrating positive ions is left [9].

To achieve a somehow optimal mixture, a few information have to be added. In noble gases for example, the multiplication process appears at lower electric fields than in other molecules, because in polyatomic molecules there are many dissipation modes. Thus to choose some kind of noble gas is reasonable as primary component such as the expensive xenon or krypton or the much cheaper argon. Without any other component the gain (the number of electrons produced during the avalanches by the charged particle) is limited in 10^3 - 10^4 interval and above that permanent discharge is induced due to secondary avalanches. Therefore, another polyatomic molecule is added to the mixture for example CO_2 or BF_3 , to make the processes more stable via

photon absorption and secondary emission suppression. With the mixing, which is called quenching in HEP, even the order of 10^6 can be achieved in terms of gain without discharges. It is also important that any other gases with high electronegativity must be forbidden, because these can capture the free electrons producing negative ions, which cannot induce avalanches in normal conditions and the effectivity of the detector will be reduced. Thus without gas-tightness and continuous gas flow the proportional counter will not work properly. As discussed earlier, Charpak used parallel anode wires in the chamber and recognized, that the induced signals by the avalanche fully compensate the capacitive coupling between the independent counters. The electric field can be seen on Figure 9 which also shows the cross-section of the structure and the general layout of the anodes that are stretched between the cathodes. Two parameters, namely the wire spacing s and the distance from the cathode plate l , which is called "gap", specify the operation of the detector for example the space resolution [9]. Luckily the inventor and his colleges managed to understand the aspects of proportional counters deeply, and with their experiences and measurements, the classical MWPC detectors could be adapted beyond HEP.

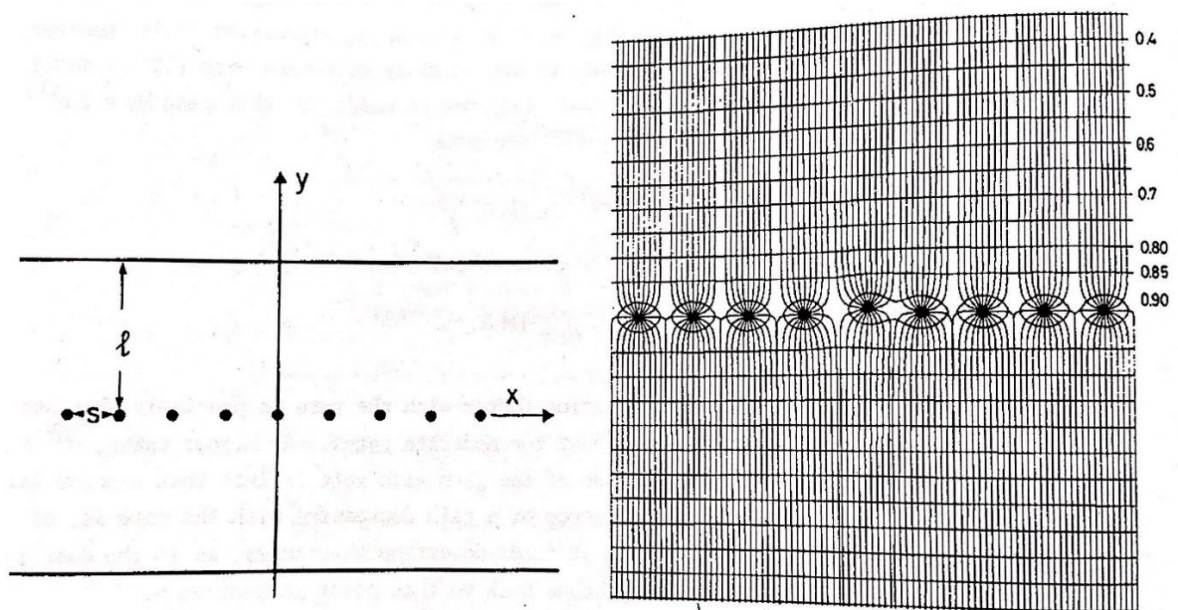


Figure 9. The construction parameters, the electric field and the equipotential lines by the set of parallel anode wires in a multiwire proportional chamber. [9].

2.3. The Hungarian-Japanese collaboration

In 2016 an international collaboration about muography between Earthquake Research Institute (ERI) and Wigner RCP was started to form. As earlier was shown, Japanese scientist tried to use the properties of muons for investigating volcanos. The goal of the collaboration is to investigate the Sakurajima volcano in Japan, therefore a common patent was made about using the REGARD's MWPCs for monitoring the volcano continuously [16]. Figure 10 shows the first detector system, which was installed in January 2017 and the structure was extended and upgraded year by year. During that time, a multinational company NEC Corporation has also joined and a licence agreement was made about the industrial production of these detectors. With these extensions not only more chambers were installed, but the whole system improved in many ways. For example the gas system, the high voltage unit and the data acquisition, the storage and the power supply.



Figure 10. The first MWPC system which was installed in a strong steel framed box approximately 3 km from the crater. There are lead absorber walls between the detectors which improves the noise performance [17].

2.4. Large MWPC for muography

As discussed before, smaller type of MWPCs were constructed for educational purpose and these detectors indicated a way for the possibility of outside or field use. Although the dedicated tracking system for muography had to be optimized from the very beginning as an innovative approach to the classical MWPCs, but with simplifications and additional design features compared to the chambers in HEP. First of all, considering that the rate of muons is much lower near the surface (in the order of 100 particles/ m^2s) than in the usual experiments. This rate is further reduced by the large object of interest, therefore relatively large sized detectors are essential for sufficient statistics. Of course, cost is also very important, in the sense of producing, transporting and maintaining. Secondly, leaving the laboratory means, we must consider environmental effects appearing in the form of temperature, pressure and humidity changes. This phenomenon includes slow or rapid and moderate or huge differences, which have to be tolerated by the system in a long term operation. The two types of chambers constructed by the REGARD group, based on previous experiences with gaseous detectors, have a sensitive area of about 0.6 m² (MWPC-80) and 0.9 m² (MWPC-120). Through many years of measurements with the “80-type” system, we could extend the design for an even larger chamber, which resulted the “120-type” detectors. The two MWPCs in the sense of construction are quite similar, the inner structure can be seen on Figure 11.

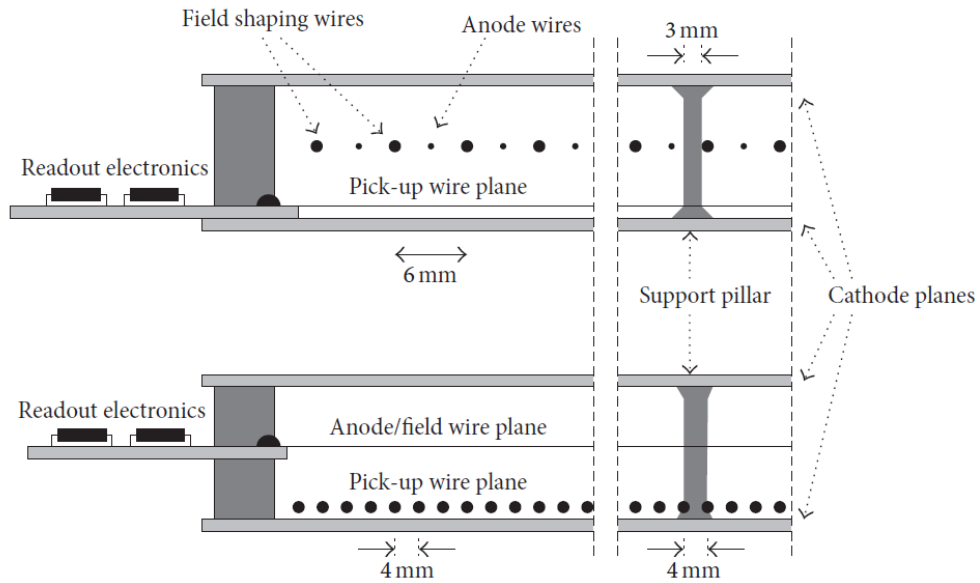


Figure 11. Cross section of the REGARD MWPCs [18].

The two different wire planes which are perpendicular to each other as Figure 11 shows, is stretched between two cathode plates. These are made of glass fibre reinforced epoxy which is a standard material called FR-4. The names for the different type of detectors are coming from the area of the cathode, MWPC-80 uses 80 cm \times 80 cm cathode, while the MWPC-120 has 120 cm \times 80 cm cathode, both with a thickness of 1.5 mm and has copper layer on each side for grounding purposes. Due to the relatively small thickness and large size, these plates could be easily bent by the pressure of the operating gas mixture. Therefore, to outweigh this bulging effect, an internal support structure has been developed and implemented into the chambers. Further reasons lie in the construction of the detectors. As mentioned earlier, the wire spacing and the distance from the cathode are strongly determine the characteristics for example the accuracy of localization or the operational voltage. In our case the distance between the cathodes is 22 mm, which is relatively larger considering the classical versions. The voltage is applied to the anode – or sense wire, so the avalanches are generated near there, thus they are used as trigger and amplitude measurement. Nearly halfway, the so-called “upper wire plane” is also consists field shaping wires and they are placed in an alternating way with 6 mm from each other. The “lower wire plane”,

which is 2 mm from one of the cathodes, include the “pick-up wires” with 4 mm spacing. These last two wires give the information about the position. In general, the detectors are made with sense wires thickness between 20 and 27 microns and made of tungsten plated with gold. The other two wires are both have a 100 micrometre diameter and made of brass. The MWPC-80 detectors use 64 field shaping wires and 192 pick-up wires connected in groups of 3 (64 groups) which covers a 768 mm region. In the case of MWPC-120, one dimension is 1.5 times longer, which results that 288 (96 groups) pick-up wires are used, while the number of the field shaping wires are the same, the only difference is the length, that is approximately 1152 mm [18]. This way the area of the chambers is sufficiently large in both cases for the statistics, although the relatively long wires can cause problems in the stability of the electric field for example the displacement by its own weight.

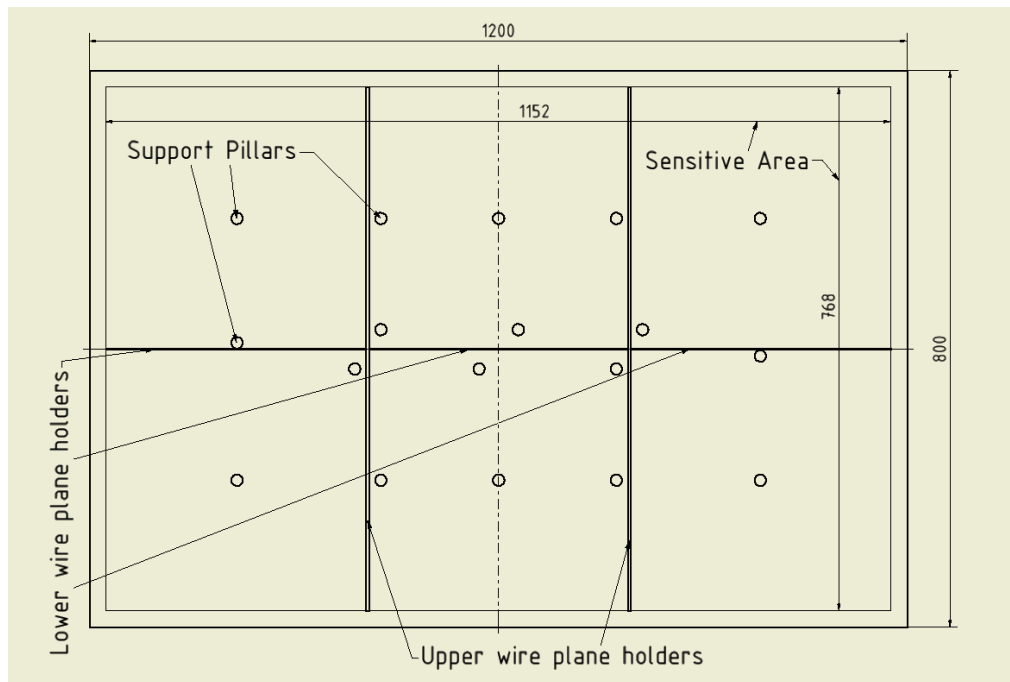


Figure 12. Schematic view of the MWPC-120 internal support structure and the sensitive area. The MWPC-80 has similar construction.

The schematic view of the internal support structure can be seen on Figure 12 which has two major features. First that the wires have to be placed with a serious spacing

accuracy in the corresponding wire plane to avoid the electrostatic instability and achieve uniform gain characteristic at the same time. The stretching of the wires and the developed construction method somewhat helps, but further support features required. The so called “wire plane holders” are important parts of every large-sized chamber. The pick-up wires lean on the 2 mm high lower holders, while the sense – and field wires are supported by the upper holders which have the height of 12 mm. In this way the long wires can be glued on the holders and have more fix points which can counteract to the effect of the gravitational force. The MWPC-120 has two upper holders at the one-third and two-thirds of the side and the lower holder is placed at the centreline as Figure 12 shows. In the case of MWPC-80, one upper holder is enough in the middle, while the lower holder is the same just shorter [18]. Second that the distance between the two cathodes have to be kept constant. For that purpose support pillars is used in a defined pattern as Figure 12 shows. In 2017, I had the opportunity to investigate the optimization process of these pillars, namely the number and the arrangement. My BSc thesis used analytical and numerical methods even measurements to examine the stress field and reduce the displacement of the cathodes to a tolerated level. These pillars have a 3 mm by 4 mm rectangular cross section and made with 3-D printing technology. The material is an ABS based polymer which has promising properties like durability, resistance to high temperatures and impact. Figure 13 shows the displacement field in a MWPC-120 chamber with the internal support. For safety reasons the middle pillars are doubled to avoid any failure during travelling and measuring in the field. A lot of different patterns were tested. The maximal displacement in the optimal case is around 0.63 mm when the internal pressure is 1000 Pa. The positioning of the pillars will be discussed in the construction [19].

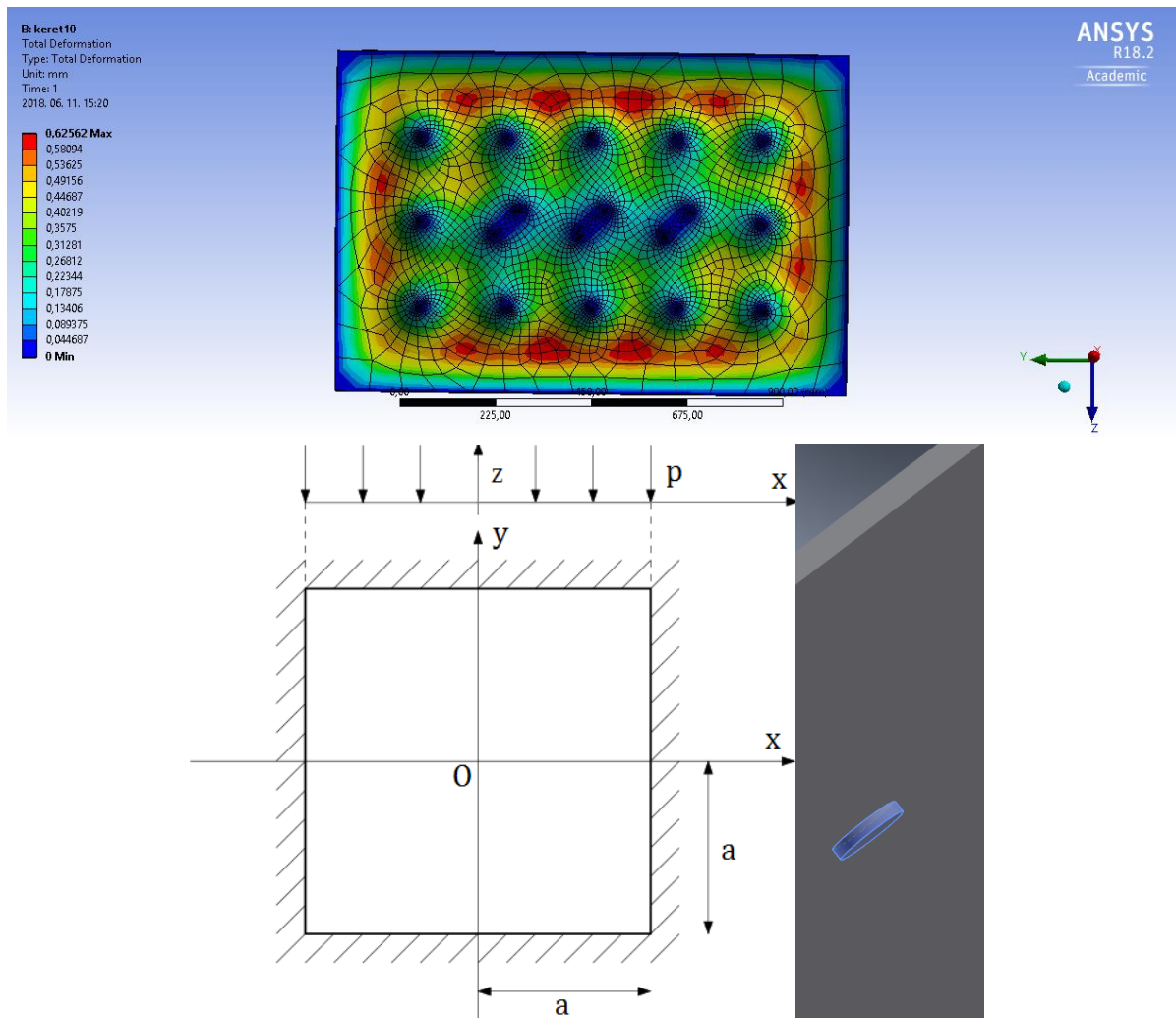


Figure 13. The displacement field of a MWPC-120 chamber (top) and the basic configuration with the boundary condition and the loading (bottom left). Each pillar is modelled using the symmetry properties. The cathode can be imagined as a fixed plate around its perimeter. The finite element analysis is made with ANSYS. The internal pressure is 100 Pa which comes from the usual continuous gas flow [19].

2.5. The construction of the chambers

As mentioned before the gas-tightness is a critical point therefore somehow a closed gas volume is required. The detector mainly uses a composite material glass fibre reinforced epoxy, thus the thermal behaviour is consistent. The side walls are G-10, while

the electronic components (soldering points for the wires, electronics support) are made of FR-4. To keep together the chamber and the gas volume, we are using a two component epoxy glue, which is an excellent choice because in that case the gas-tightness is guaranteed [18]. On top of that it has high mechanical resistance, can fill large gaps if needed, highly resistant against humidity, constant volume during the curing process and relatively low cost. The construction always takes place on a high accurate optical table, in that way the gluing procedure will be appropriate. The first step is the making of the base plate which has the electronics support and the wire holders. Figure 14 shows the base plate for MWPC-80 and MWPC-120 type chambers.

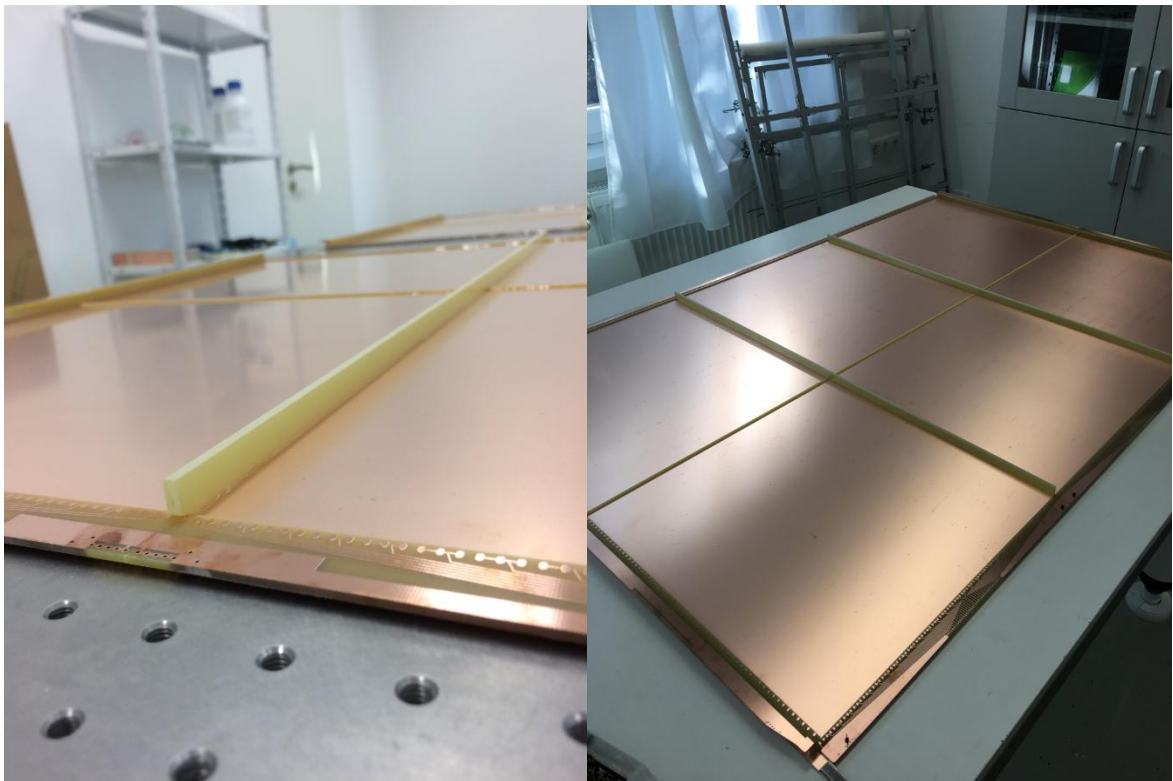


Figure 14. The base plate with the wire holders and the support electronics (printed circuit boards) for MWPC-80 (left) and MWPC-120 (right) type detectors.

After that comes the placement of the pick-up wires (lower wire plane) where proper positioning and tensioning is done. Each type of detector has its own “winding” frame that fixes two chambers at both sides. This structure can be rotated easily while the

wire is tensioned by an electric motor as Figure 15 shows. The wire spool is fixed on the motor and a calibration was done with a fixed weight on the wire. In this manner a constant torque is produced and can be tuned for different wire diameters. Typical wire tension for the 25 micron wire can be between 15 g and 30 g (0.15 N-0.3 N) and for the 100 micron wire between 50 g and 100 g (0.5 N-1 N) [14,20]. The stretching will be permanent after soldering each fixing point. The wires which are not used in the chambers have to be removed by cutting.

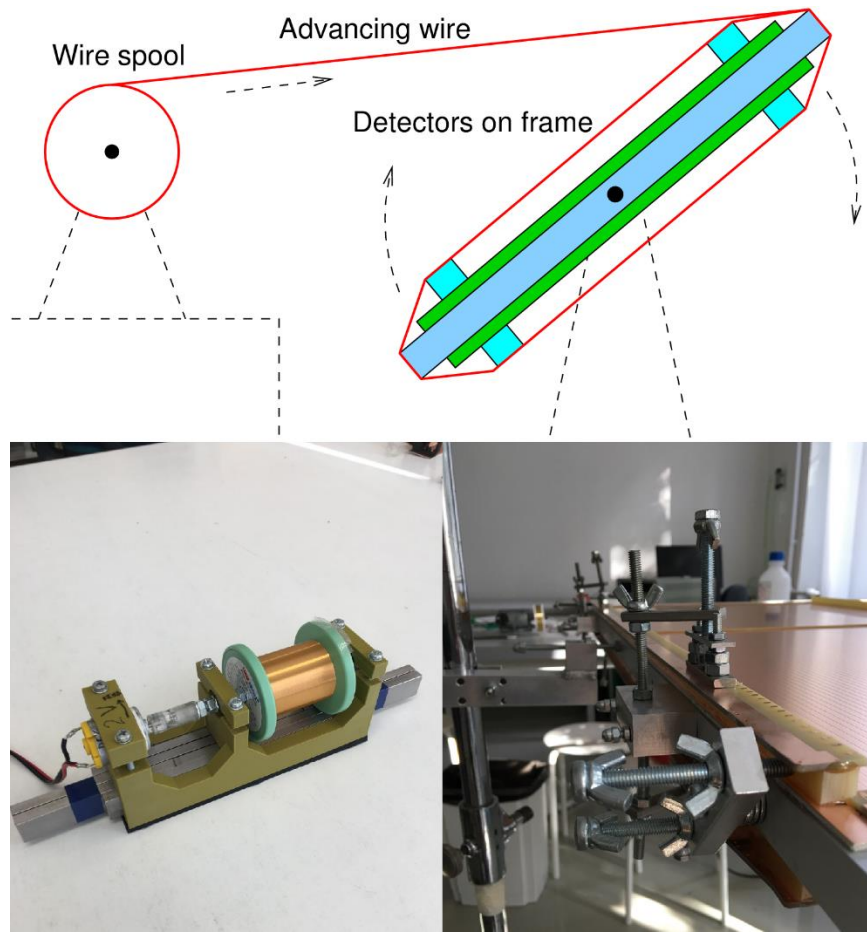


Figure 15. The winding process and its components: the electric motor (left), winding frame (right) with fixing mechanism [14].

The gas inlet and outlet is maintained through plexiglass pipes that is placed and glued in one of the taller side walls. Currently a new development is ongoing to re-

place this solution with a quick release hose coupling for better handling on the measurement sites. After gluing the side walls and the wires on the lower wire holders, the winding of the upper wire plane can be started. The winding frame is similar to the first one, although the sense and the field wires must alternate. For this purpose two bars made of polyoxymethylene with grooves are screwed at both ends and the wires are positioned to the soldering spots. Actually this means that the two wires must be stretched separately. The next step is to glue the wires on the upper wire holder and the shorter side walls. Before closing the gas volume with the top cathode, the support pillars have to be installed in the correct pattern as shown in Figure 16. The actual placement requires a lot of experience to fit between the wire planes and to not touch any of the field or sense wires [18]. After the glue has become hard enough leak tightness of every detector have to be confirmed, otherwise the system will not work properly because of the presence of the oxygen.

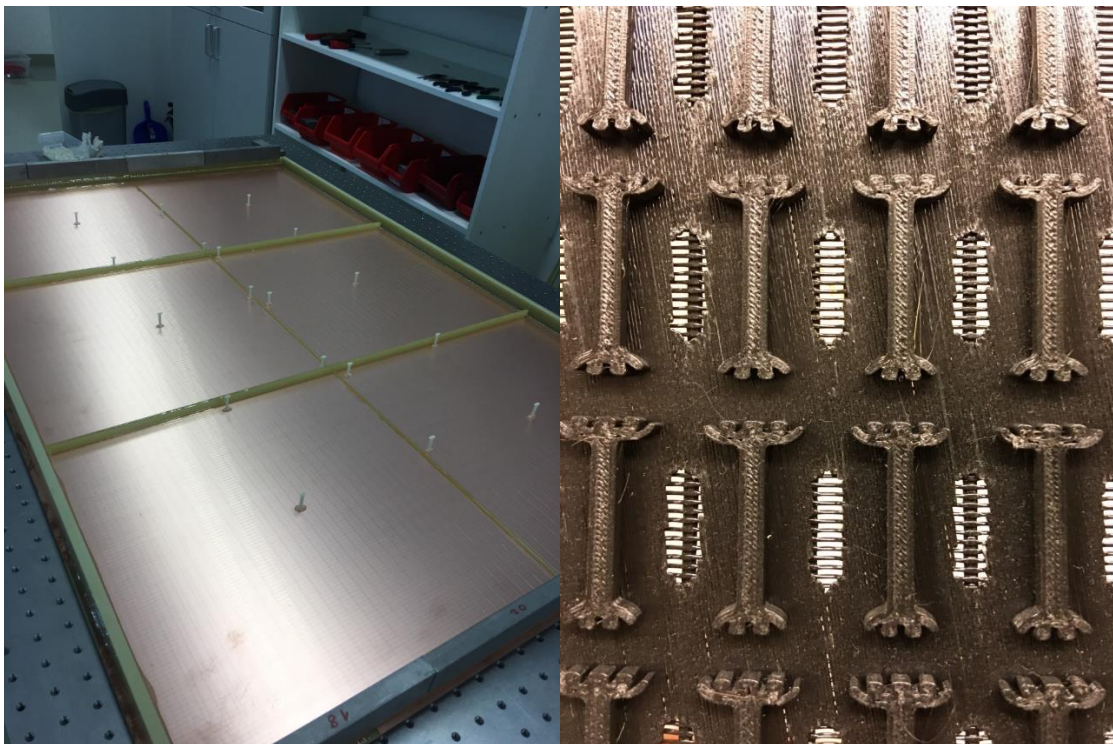


Figure 16. The inner support structure before closing the gas volume (left) and the 3D-printed support pillars (right).

The next step is to prepare and connect the electronic components to the detectors namely the high voltage connector, front-end electronics (FECs), the shielding and the cables. All the field and pick up wires are connected to an amplifier (FECs) and the sense wires are connected to an RC circuit because the noise from the input high voltage must be filtered somehow. Also good grounding is essential for a proper noise performance, because the sense wires are on positive high voltage and everything else are on ground potential [14]. Every FECs and the filtered trigger signal is connected to the so called “ADA adapter”, which is transmitting the information to the Data-Acquisition board (DAQ-board) [18]. The basic idea of the high voltage connector and the actual design can be seen on Figure 17.

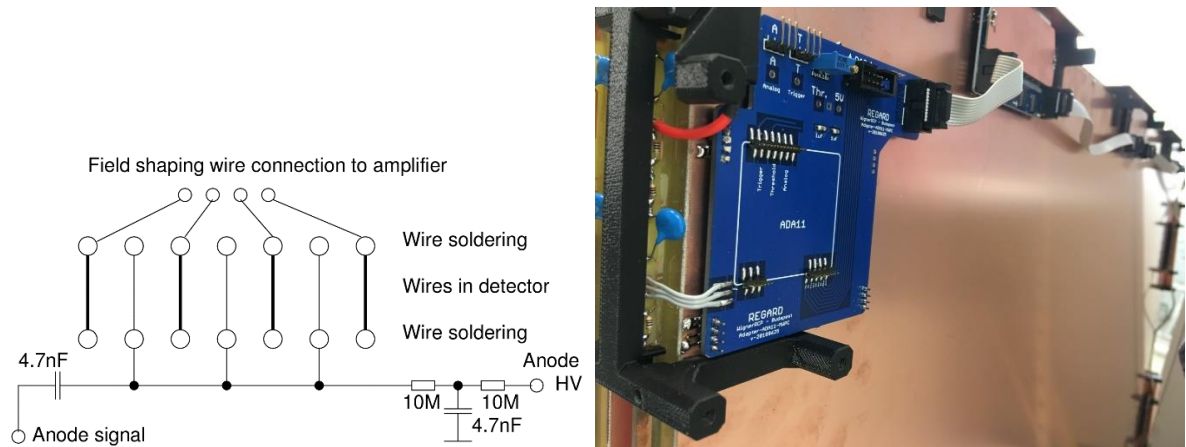


Figure 17. The basic idea behind the high voltage and the signal extraction (left) and the actual design with the ADA adapter and the FECs connected with each other. The ADA amplifier receive the information about the signal (such as gain) (right) [14].

For working gas, we use industrial argon and carbon dioxide mixture in 82:18 rate which is used in the welding industry as shielding gas, therefore cost-efficient and easily accessible. Furthermore, non-flammable and non-toxic mixture. The chambers can be connected with plastic tubes (e.g. polyurethane) and the gas has to be circulated

in the system with a flow between 0.5-6 l/h, it depends on the purity of the gas in the chambers.

2.6. Cosmic muon detection with REGARD MWPCs

Each chamber can provide position information in two dimensions (usually denoted with x and y) with a spatial resolution around 1 cm. To acquire the third dimension (denoted with z) a few chambers have to be stacked with a specified distance from each other and with multiple measurement points, straight lines can be fit which results particle tracks. The detectors have the same anode high voltage provided by the high voltage unit and the data lines are connected to the DAQ-board which integrate triggering logic and timing. This is controlled by a Raspberry Pi 3 (RPI) microcomputer - in a large system with multiple MWPCs - as the core of the data acquisition. Without any logic rule the system would produce a lot of unnecessary data and we are interested in muon tracks. Therefore, coincidence level is applied with at least 4 chambers, which means that minimum this amount of detectors has to send trigger signal at the same time to record that event [18, 21]. In the field a setup usually contains 7 or 9 MWPCs and has its own Data Acquisition system, which contains the high voltage unit, low voltage power supply, the DAQ-board, the RPI and a dedicated sensor for registering environmental parameters. The arrangement and the connection are shown by Figure 18. The low voltage power supply converts the mains electricity to 12 V and 5 V DC voltage for the FECs and the RPI. The high voltage unit uses an ISEG BPP-30304-5 module which is able to maintain the voltage up to 3 kV and can be adjusted with a potentiometer. There are two displays for monitoring the voltage and current values [22]. To register the environmental conditions, a Temperature Humidity Pressure (THP) sensor was developed by Szabolcs Balogh and adapted for every system [23]. In this way the total power consumption is around 8 W per module.

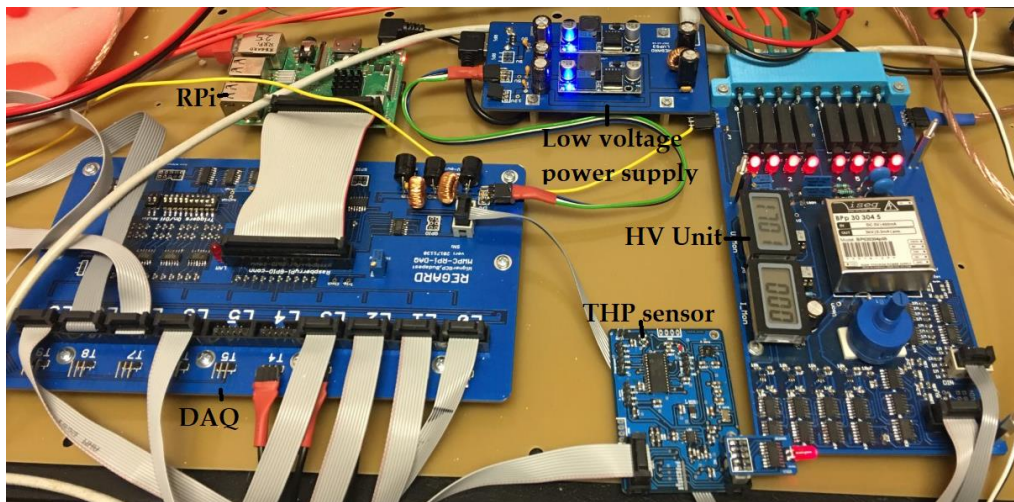


Figure 18. The usual measurement arrangement for the electronics.

The Sakurajima Muon Observatory (SMO) currently uses 10 modules of MWPCs with tracking layers 7 or 9 besides two scintillator systems which was installed earlier by our Japanese colleges. Currently this is the biggest MWPC-based muography system with an active area 8 m^2 and the imaging quality is sufficiently high to see inside the mountain in detail [22]. Also absorber lead walls are used between the detectors to deflect the trajectories of particles, thus physical background (electrons, protons and low-energy muons which we are not interested in) can be decreased [24]. A critical feature of a particle detector system is the detection efficiency. It is referring to a single detector and defined by the probability that a valid particle hit (position) is detected indeed. This can be done by choosing one of the chambers and checking the particle trajectory formed from the rest of the detectors excluding the one under study. If this pattern is a straight track, one can check if there is a hit or not at the expected position within 5 sigma of the position resolution. The performance of the 10 MMOS is shown by Figure 19 with the registered environmental changes in a 6-month period. Although the tracking efficiencies are excellent, it is reasonable to define quantitatively the effect of the environmental parameters to the detector system.

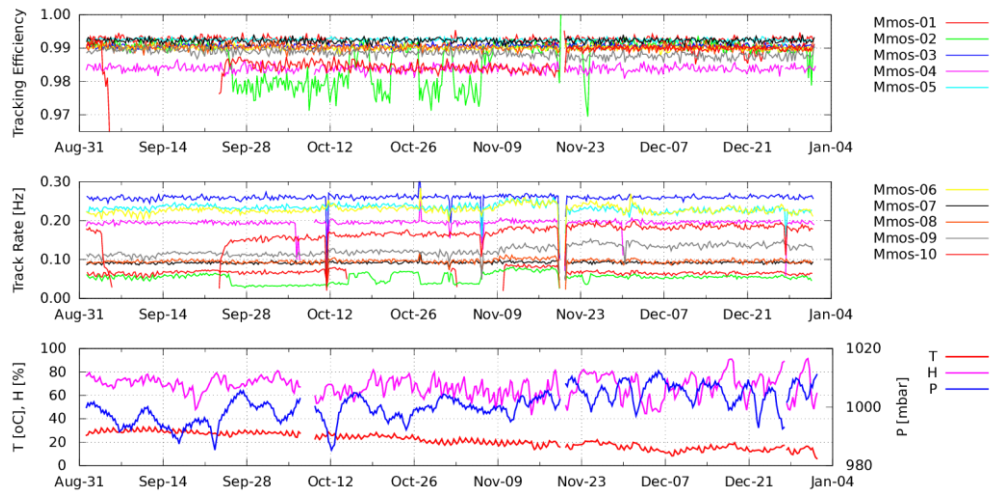


Figure 19. Performance of the 10 modules in a 6-month period. The detector efficiencies are calculated numerically using the single layer efficiencies for tracks with at least $N-2$ hits (N is the number of chambers in the system). The gradient of the environmental parameters is shown at the bottom [22].

3. THE EFFECTS OF THE ENVIRONMENTAL PARAMETERS

3.1. *The properties of the gain*

As mentioned in Chapter 2, after Charpak's invention they started to use the MWPCs widely as detectors of ionising radiation and with the geometric flexibility of sensitive volume, a lot of different chambers have been used in a huge range of applications. Not only in archaeological or geological implementation but in nuclear or biomedicine due to its imaging capability. Of course the development of the electrical industry was fundamental to produce precise electric structures such as printed circuit boards which was needed in many designs. Although to design a chamber which is appropriate for each application, the value of the gain as a function of operating gas density, voltage and geometry is necessary to know. The wide literature about the properties of the gain mainly consist of experimental studies with different gas mixtures and devices from many authors for example Rose and Korff [25], Diethorn [26], Williams and Sara [27], Zastawny [28], Charles [29] and Aoyama [30]. These formulas were derived independently from each other and has no relation between them. Some of them lay on models about the behaviour of electrons and some of them without any theoretical considerations, just assuming an analytical form. The only common surmise is the functional dependence between α/ρ and E/ρ , where α is the first Townsend coefficient which describes the multiplication process, ρ is the density of the gas and E is the electric field strength. The electrons drift towards the anode wire in an increasing electric field which can be formulated as:

$$E = \frac{\lambda}{2\pi\epsilon_0} \frac{1}{r}, \quad (1)$$

where r is the distance from the wire, ε_0 is the permittivity and λ is the linear charge density on the wire which can be calculated. Under normal gas conditions, the whole process develops in a nanosecond until the electrons are collected on the wire. The avalanche itself is quite complex and can contain single or multiple ionization, recombination, space charge and photoelectric effects. Usually the secondary effects are neglected in the simplest models and only the direct ionisation is counted. After a multiplication, the increased number of electron per path ds can be calculated as:

$$dN = N\alpha ds. \quad (2)$$

The first Townsend coefficient is related to the ionization process where the electrons have sufficient energy and the gas properties such as the mixture and the density. This complex relationship implies the fact that no theoretical formula exists for α and it is different for every mixture. Furthermore it is also increases with the electric field E , due to the increase of the collision energy. It is reasonable to fix the E/ρ ratio, which was used by many authors, because in that way α changes proportionally with the density and the relationship can be described as [31]:

$$\alpha\left(\frac{E}{\rho}, \rho\right) = \frac{\alpha_0}{\rho_0} \rho = f\left(\frac{E}{\rho}\right) \rho. \quad (3)$$

For the visualization Figure 20 shows measurements with noble gases acquired by A. von Engel where coefficient α over the gas pressure is presented as the function of the electric field over the gas pressure. Instead of the density, the gas pressures are shown in both denominator, because normal temperature was used [32].

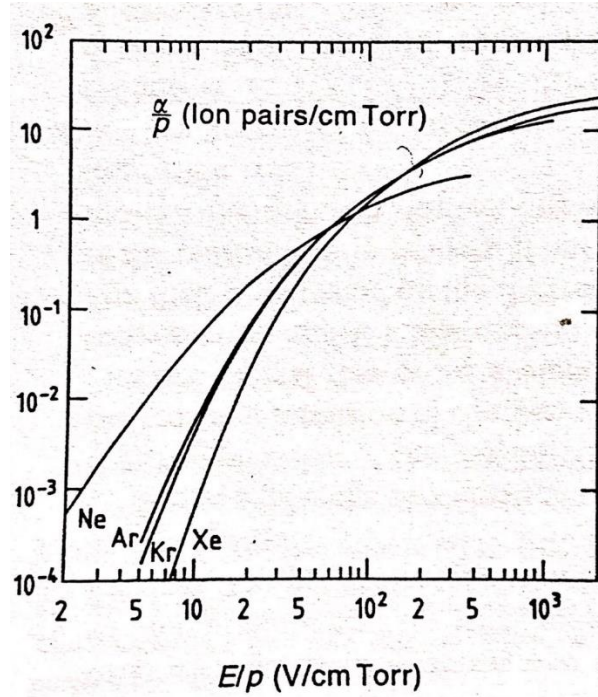


Figure 20. The measurements of the first Townsend coefficient in different noble gases as a function of the electric field. The horizontal axe is shown in logarithmic scale. Our first impression is that the functional dependence is complicated [32].

Considering a wire, the amplification factor or gain can be obtained by integrating (2) between s_{min} and a , where s_{min} is the point where the avalanche starts, and a is the wire radius:

$$G = \frac{N}{N_0} = e^{\int_{s_{min}}^a \alpha(s) ds} = e^{\int_{E_{min}}^{E(a)} \frac{\alpha(E)}{dE/ds} dE}. \quad (4)$$

In the previous equation N and N_0 are the final and initial number of electrons. Combining (1) and (4) we get:

$$G = e^{\int_{E_{min}}^{E(a)} \frac{\lambda \alpha(E)}{2\pi \epsilon_0 E^2} dE}. \quad (5)$$

Of course it works with different type of detectors if the electric field can be calculated. From here, every authors in the literature assumed a relationship between α/ρ and E/ρ as mentioned before and derived the final formula from that. It can be seen that

the calculation of the gain is quite complex and have to be measured directly with our system, later it can be verified with the experimental results from the past. Although to get acquainted with the tendencies of each parameter, I will briefly summarize the simplest formula which is related to Diethorn. The statement was, that α is proportional to E , which is not unreasonable in short ranges if we look at Figure 19. In that way $\alpha = \beta E$ can be substituted into (5), thus:

$$\ln G = \frac{\beta\lambda}{2\pi\epsilon_0} \ln \frac{\lambda}{2\pi\epsilon_0 a E_{min}}. \quad (6)$$

The potential difference between s_{min} and a :

$$\phi(a) - \phi(s_{min}) = \int_a^{s_{min}} E(r) dr = \frac{\lambda}{2\pi\epsilon_0} \ln \frac{s_{min}}{a} = \frac{\lambda}{2\pi\epsilon_0} \ln \frac{\lambda}{2\pi\epsilon_0 a E_{min}}, \quad (7)$$

that will drive the doubling of electrons from a number of Z (generations of doubling the electrons) in the avalanche. Thus:

$$Z = (\phi(a) - \phi(s_{min}))/\Delta V \quad (8)$$

where ΔV is the average energy required to create one more electron. Hence the gain can be obtained as:

$$G = 2^Z \quad (9)$$

$$\ln G = \frac{\ln 2}{\Delta V} \frac{\lambda}{2\pi\epsilon_0} \ln \frac{\lambda}{2\pi\epsilon_0 a E_{min}} \quad (10)$$

The minimal field needed for ionization must be proportional to the gas density, thus:

$$E_{min} = E_{min}(\rho_0) \frac{\rho}{\rho_0} \quad (11)$$

where ρ_0 is the normal gas density. After combining (10) and (11) we could get an expectation about the variation of the gain with the density:

$$\frac{dG}{G} = -\frac{\lambda \ln 2}{\Delta V 2\pi\epsilon_0} \frac{d\rho}{\rho}. \quad (12)$$

We can clearly see that the gain increases with temperature if we fix the pressure and decreases with pressure if the temperature is fixed in these kind of detectors [31].

3.2. *The effect of the environmental parameters*

3.2.1. FIRST MEASUREMENTS WITH OUR SYSTEM

In 2016, before the first MWPC system was installed in Japan, our colleague László Oláh tested the setup under ambient outdoor conditions. The tracking system was placed with a frame on a flat roof building and was lightly covered, therefore it could receive sunlight. The 6 days long measurement included daily temperature variations more than 25 °C. This changes correspond to approximately 10 % change in absolute temperature which means in gas density. To avoid massive difference in gain, in this setup the anode high voltage was adjusted by 1 V for 1°C temperature increase. This compensation resulted in a slight, 10% mean amplitude variation with sufficient tracking efficiency at the whole time as Figure 21 shows [18]. It is reasonable to distinguish every component which could have effect on the gain.

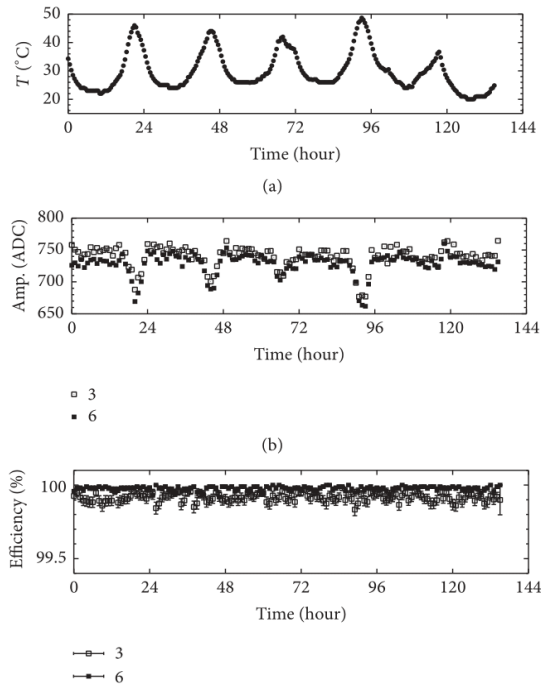


Figure 21. The measurement with the first system in outdoor condition. The signal amplitude is proportional to the gain. The effect of the temperature is clearly visible although partial compensation of the HV was also present to keep the efficiency sufficiently high [18].

3.2.2. TEMPERATURE DEPENDENCE OF THE ELECTRICAL COMPONENTS

As mentioned before there are many different key components of the system outside the detector for example the DAQ, the high voltage unit and the ADA amplifier. These items could have effect on the chamber due to environmental changes. Like every electrical system, they consists of resistors, capacitors and inductors that usually have temperature dependence itself and also the extreme humidity (above 85%) can have consequences. Although, these should be separated from the “physical” dependencies of gain to investigate the properties of our chambers because they come from the not ideal elements and the system design and not related to the gas density. First let’s examine the characteristics of the ADA11 amplifier, this measurement was made by RE-

GARD group and the setup can be seen on Figure 22. The amplifier and two THP sensors were put in a box with basic thermal insulation and two light bulbs to raise the temperature high enough with the modification of the voltage on the power supply. The signal generator that was connected to the amplifier could sent zero- or 1 Me^- (1 million electron) output, to have a reasonable value and to check the zero-point displacement. A similar DAQ to the MWPC setup controlled the measurement as shown before.

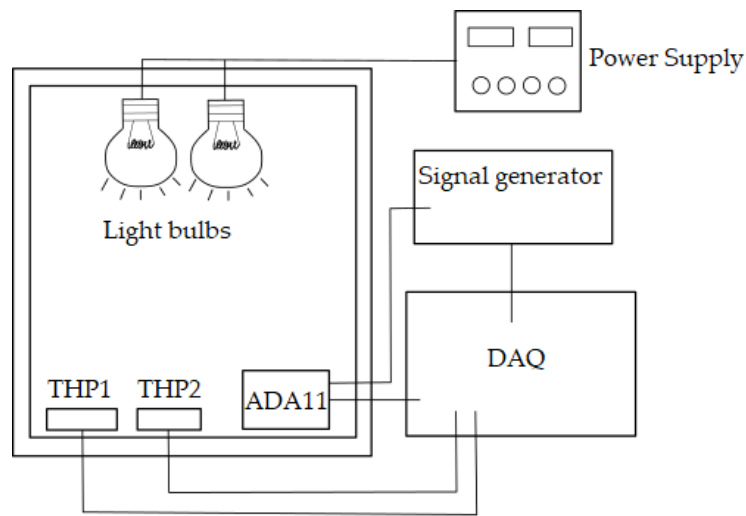


Figure 22. Measurement setup for the temperature dependence of the ADA11 amplifier.

The temperature was raised above $55 \text{ }^\circ\text{C}$ in 2 hours from ambient $28 \text{ }^\circ\text{C}$ and then decreased back to the starting point in another 2 hours. The aspects of the signals and the THPs during the measurement are shown on Figure 23. It is visible that the zero line is constant and does not depend on the temperature changes. Figure 24 is showing the relative change of the signal amplitude to the zero line as the function of temperature. A straight line was fitted with least squares method and resulted a $-0.6\%/^\circ\text{C}$ decrease in amplitude. This means more than 10% change if the temperature changes with $20 \text{ }^\circ\text{C}$ which is quite large and this can be a reason behind the difference between the temperature and the pressure correction coefficients which will be discussed later.

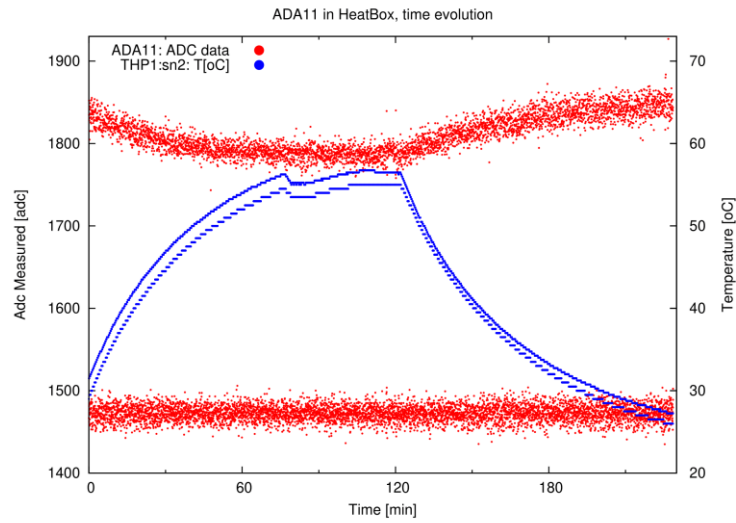


Figure 23. The measurement of the ADA11 amplifier in the small heat box made by the REGARD group. In the horizontal axis both the measured ADC, which is proportional to the amplification, and the temperature are denoted as a function of time. The upper line is related to the 1 Me^- output and the line below is related to the zero output.

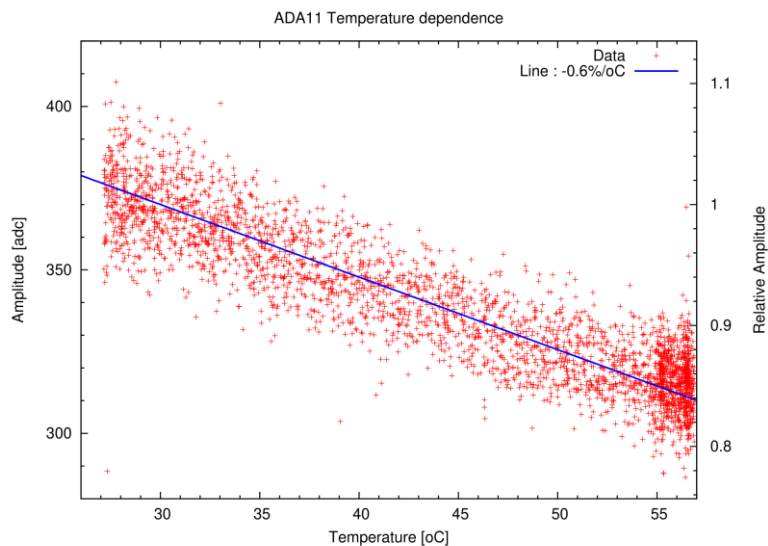


Figure 24. The relative change of the signal amplitude to the zero line as the function of temperature.

Second, the high voltage unit must be investigated because the value of the potential difference determines essentially the gain as shown before. The existence of the temperature dependence would mean an indirect effect on the gain through the voltage besides the direct effect. For this purpose the same box was used as for the amplifier. The measurement setup can be seen on Figure 25.

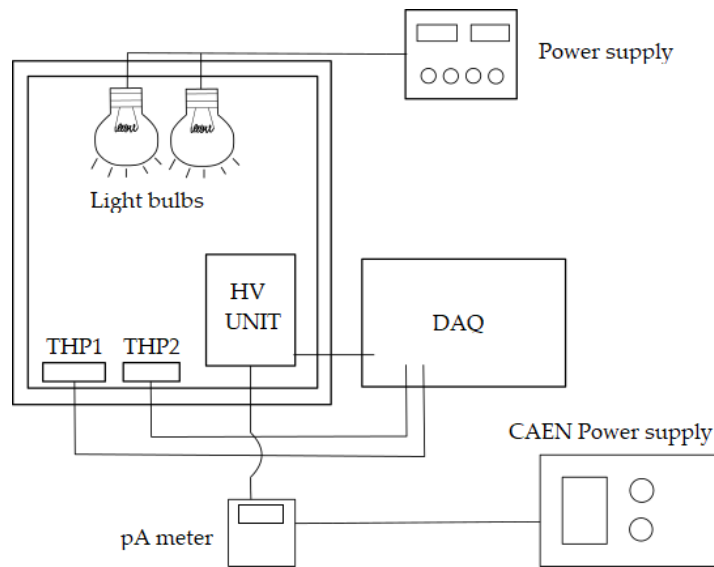


Figure 25. The measurement for the temperature dependence of the HV unit

The HV unit was put next to the THP sensors inside the box and it was connected to a highly accurate CAEN power supply¹ through a picoamper meter. The idea is to put the standard voltage value (1700 V) on both the HV unit and the power supply and measure the current on the pA meter. In normal circumstances this current is zero due to the equal voltages and if the value changes inside due to the temperature some current should appear. The first step is to calibrate the light bulbs without the HV unit, to know the equilibrium temperature at each voltage. The actual values can be seen in Table 1.

¹ CAEN 4 Ch NIM/Desktop Programmable HV Power Supply, Model: NDT1471H

U [V]	T [°C]	t [h]
2	32.75	0.5
3	34.5	1
4	38.75	1
5	44.25	1.5
6	49.75	2
7	54	2
8	59.75	2

Table 1. The calibration for the light bulbs. The voltage of the power supply and the corresponding temperature and time for the equilibrium are shown.

In Japan at the measurement site, the highest values of the temperatures was around 50 °C, thus let's use it as the maximum. To achieve that level 7 V was applied on the power supply. As the temperature increased, the current on the pA meter decreased slowly, which means the voltage on the HV unit was getting larger than the CAEN voltage, although this slight effect won't have any influence on the gain, because the temperature has another much more stronger indirect effect on the nominal voltage during the measurement, this will be discussed later. Table 2 shows the results and the conclusion is that the HV unit alone doesn't have significant temperature dependency.

T [°C]	U [V] HV display	U [V] HV software	U [V] CAEN	I [nA] pA meter
24.5	1701	1701	1701	0
28	1701	1701		-14
31	1701	1701		-23
34	1701	1702		-32
37	1701	1702		-39
40	1701	1702		-45
43	1701	1702		-50
46	1702	1702		-56
49	1702	1702		-62

Table 2. Each step of the temperature changes and the corresponding voltages are shown. The first column is the displayed value on the HV unit, the second is the measured value and the third is the CAEN voltage.

3.2.3. EFFECT OF TEMPERATURE, PRESSURE AND THE CURRENT ON THE CHAMBERS

It is reasonable to summarize a few thoughts before the further investigation of this problem. The first thing is the missing theoretical expression of the first Townsend coefficient α , which was mentioned before, because in that way the analytical calculation is out of the question. Second, that these various effects usually occur at the same time and it is hard to see what is really happening inside the detector system. Third, as it was shown in Section 3.1, these phenomena are not exactly linear in the entire scale of the parameters, although the gradients we are facing, always happen in

smaller ranges which can be approximated as linear. For example more extreme conditions can be imagined like around or below 0 degree centigrade or at a few thousand meter higher level where the pressure is much smaller. The pressure usually changes with the ambient conditions because the chambers have an opened end section (with enough volume to counterweight the “breathing” effect, will be discussed later), so in these measurements only the actual weather changes it. In order to vary the temperature, a larger version of the previous heat box was needed with the following properties:

- Homogeneous temperature everywhere inside the box
- The maximal value should be around 50 °C
- The chambers must fit inside while fixed mechanically and tracks are essential (1 chamber is not enough)
- To be able to measure with high humidity later
- Easy handling.

Our group agreed, that four chambers are acceptable for the tracks (for the z coordinate four measurement points are used for the straight line fit) and these can be put as close as possible to each other, because I’m not interested in angle resolution where the distance matters, furthermore too much layers would result a huge heat box. First I built the rack using a bunch of slotted angle iron. We have a testing setup for the newly built chambers and a similar but smaller version of it was constructed for this purpose. The reason behind is the relatively easy assembling process via metal screws, thus we can measure outside in rough terrains. The chambers weights are 8 kg for the MWPC-80 and 10 kg for the MWPC-120 each and with even many layers the structure is fixed mechanically. I continued with the heat box itself and the material choice was an XPS (extruded polystyrene) basis and EPS (expanded polystyrene) for the box, because of the great thermal properties and low density. Standard EPS elements was used with the size of 50 cm x 100 cm x 4 cm and fixed with each other by polyurethane foam. The

final size of the box is 70 cm x 152 cm x 102 cm which includes some place for the “heating”. The measurement setup is shown by Figure 25. The XPS was placed on a long table and the horizontality was set to a tolerable level to ensure smooth join between the box and the base. After that four calibrated MWPC-120 type detectors were installed into the rack and a dedicated DAQ for this measurement outside. I calibrated and used three THP sensors, two inside diagonally from each other to monitor the temperature changes and one outside for the ambient values. To control the temperature, two power resistors were implemented and a cooler fan to circulate the air inside for the homogeneous heating as Figure 26 shows. These were connected to a power supply unit² outside, where the DC voltage and current limits could be set.

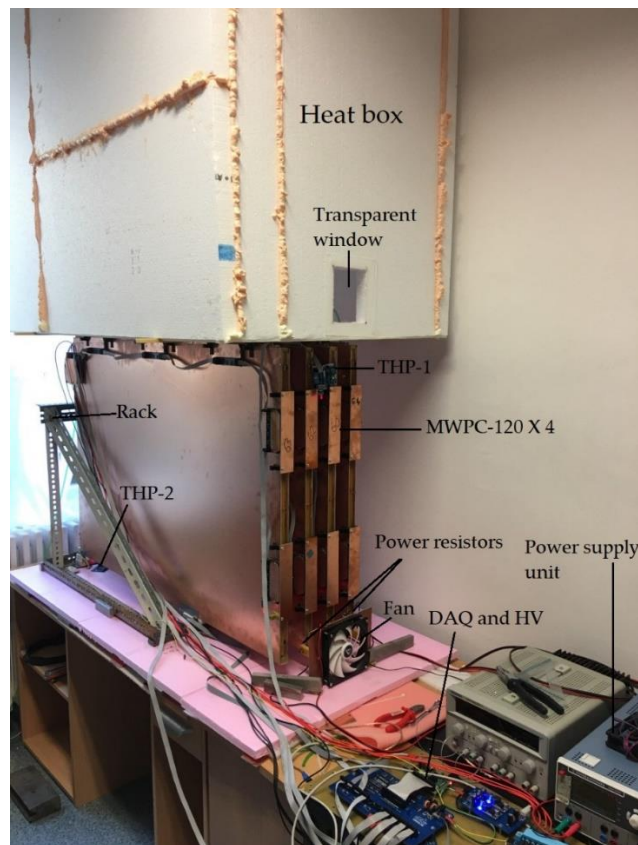


Figure 26. The measurement setup for the heatbox. A small transparent window is also installed to be able to check the fan. The THP sensors were placed at two different location inside to monitor the temperature field.

² Rhode Shwartz HMP4040 Programmable power supply

The order of the detectors are the following: 63 at the front, 62, 60 and 64 next to the wall. The gas line was installed in the same way and after 64 a buffer tube was also applied. The reason behind that is the so called “breathing” effect, when the density changes in the chambers the gas volume also changes according to it. This means that the last chamber in the line can suck air back in to the gas volume when the density decreases too rapidly and the constant flow cannot balance it. It can be easily recognized with the sudden gain drop of the last chamber due to the presence of oxygen. In one way it can be controlled by stepped cooling to avoid large changes or with a buffer tube, where the air is sucked into the tube and not inside the chamber. In my setup both of them was applied. The power resistors have a nominal power $P_n = 50\text{ W}$ and resistance $R = 10\ \Omega$ each. The settings for the reference measurement are the following:

- Nominal high voltage: $U_n = 1700\text{ V}$
- Gas flow (Volumetric flow rate): $Q = 2.5\ \frac{\text{l}}{\text{h}}$
- Coincidence level (how many chambers detected the particle at the same time): 3
- Triggering with 4 chambers.

Before the real measurements it is reasonable to calibrate the system and make reference measurements to avoid any external effect (e.g. the gas is not pure enough) which is not part of my investigation. Table 3 shows the power values from the voltage and current settings and the corresponding temperature.

P[W]	T[°C]
0	27-29
40	35
80	41.5
120	48

Table 3. The calibration for heating. With the active fan, I was able to increase the power above the nominal values safely by 10-15%.

Figure 27 shows a 36 days measurement with 30 minutes time bins, containing temperature changes from the weather and the heating cycles, the pressure changes from the weather and a secondary effect from the current change. Our experiences from the Sakurajima measurement also show that at higher temperatures, few orders higher currents occur which decreases the nominal voltage. The normal current for these systems should be in the order of nanoamperes, however at high temperatures and humidity it can be three orders of magnitude higher (few microamperes). This effect comes from the change in resistance of the glue and/or the FR-4 elements due to the extreme environmental changes and they start to behave more “conductive”, same as a semiconductor. To summarize this indirect effect, when the temperature increases after a certain point the current starts to rapidly increase and induces a decrease in the nominal voltage, which results a gain decrease.

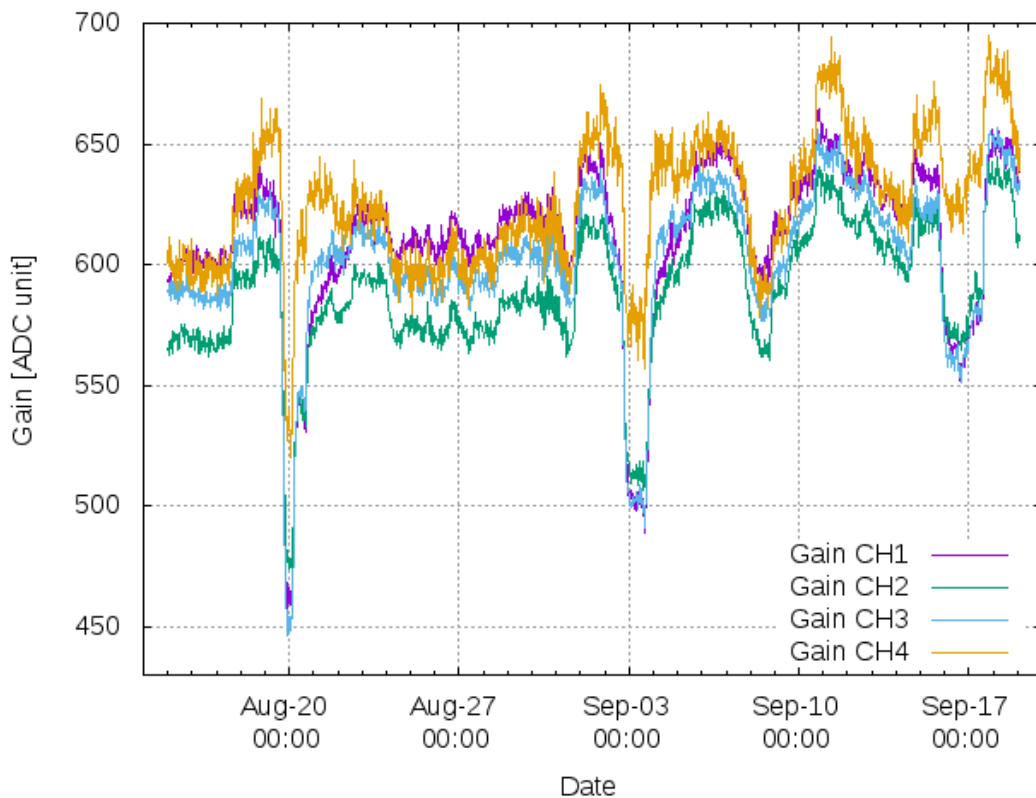


Figure 27. The gain values of the four chambers in a 36 days measurement period. All of the effects are included. Also the difference can be recognized between each chamber. The gain values are calculated every 30 minutes.

To formulate the phenomena, I used Diethorn's idea as a linear approximation and took care of each effect separately. This can be modelled as:

$$\ln G = G_0 - \kappa I + \eta T - \eta p, \quad (13)$$

where G is the measured gain, G_0 is the nominal gain, I is the current, T is the temperature, p is the pressure inside and κ, η are the corresponding correction factors for the effects. In ideal case the constants for the temperature and the pressure are the same with opposite sign, although in reality it won't be the same because of other effects. The chambers in general are not perfectly the same, therefore the gain values can be different as Figure 27 shows. This implied to make the corrections individually for the four detectors. On Figure 28 the change of the environmental parameters are shown.

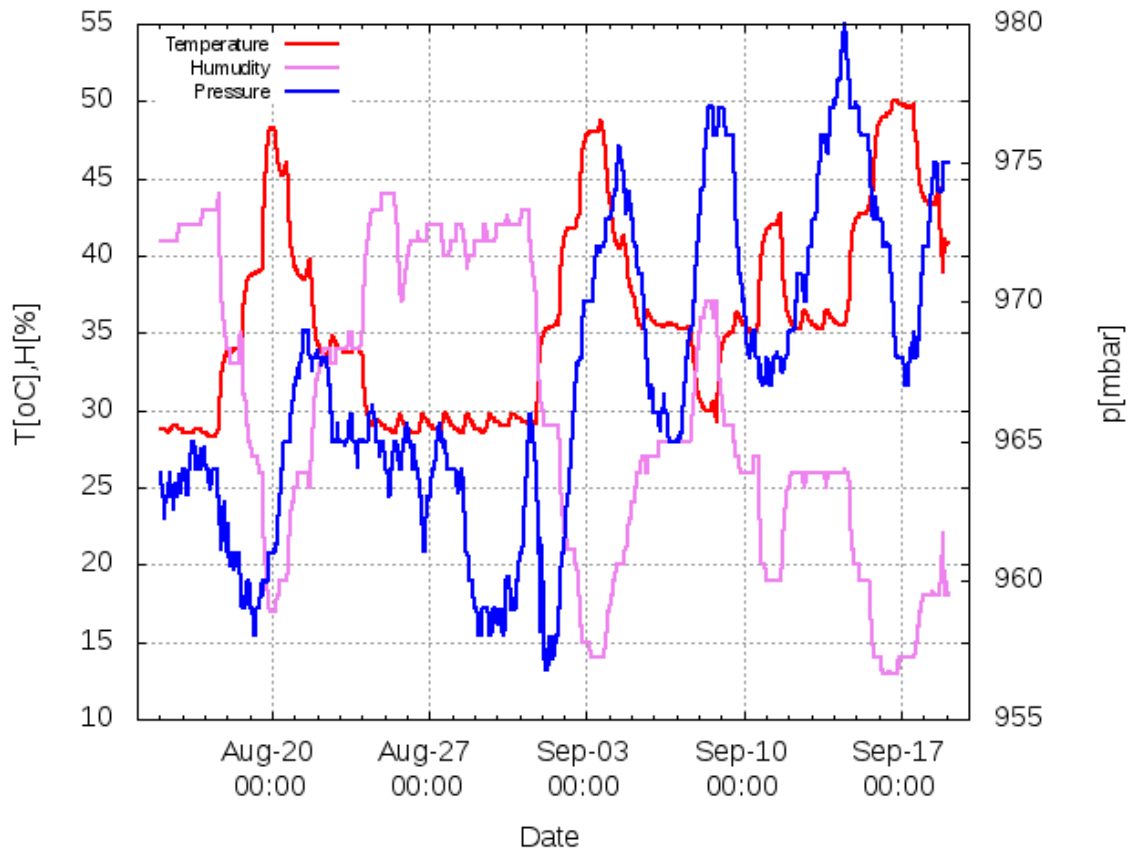


Figure 28. The environmental parameters during the measurement period inside the box. Three big cycles were maintained including heating and cooling.

To make it easily comparable with other measurements, on the one hand the relative values were taken into account by defining a rate between the actual and the mean gain of the chamber, on the other hand in the case of pressure- and temperature correction, dimensionless values will be introduced. As discussed before, the effect of the current to the gain is quite complex and indirect. The first aspect is the relationship between the temperature and the current which is represented by Figure 29.

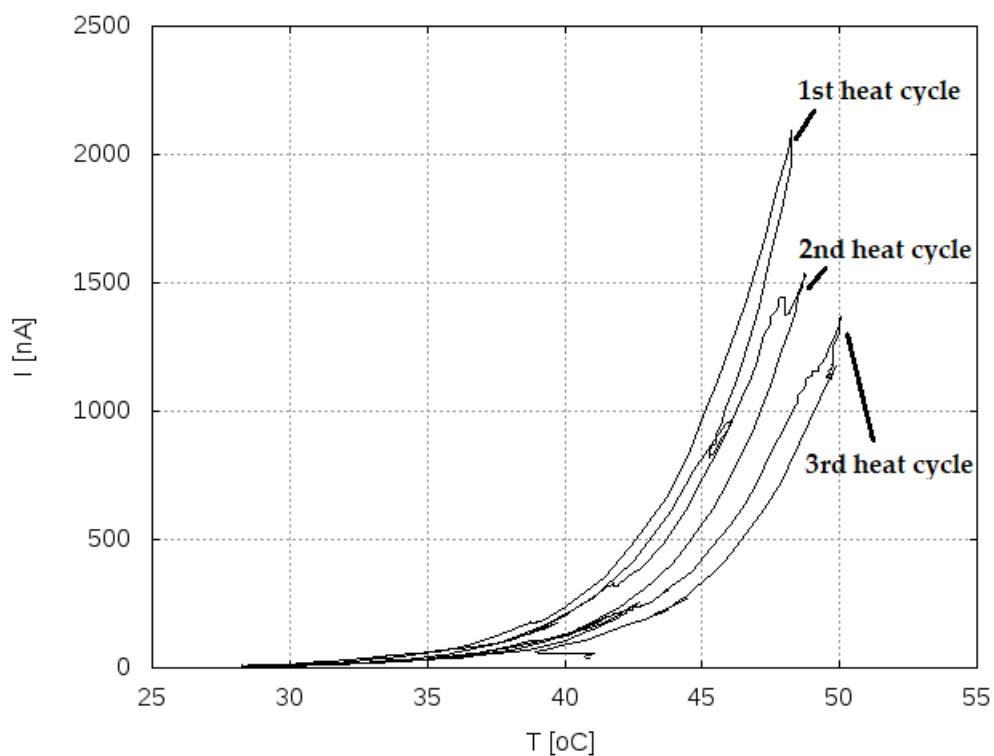


Figure 29. The temperature as a function of the current in the whole period. The exponential behaviour can be analogical to a semiconductor’s temperature dependence. Another interesting phenomenon is the “tempering” effect of each heat cycle related to the glue.

Above 40 °C the current starts to grow exponentially and a slight hysteresis effect also visible between heating and cooling. The other interesting thing that the growth rate and the maximal value of the current is decreasing with each cycle and this “tempering” process is beneficial to the detectors resulting lower values. Figure 30

shows the current-voltage relationship where the linearity can be clearly seen. The gain is extremely sensitive for the operating voltage, a few μA implies a 1-2 % voltage drop, but its effect for the gain is more than 20%.

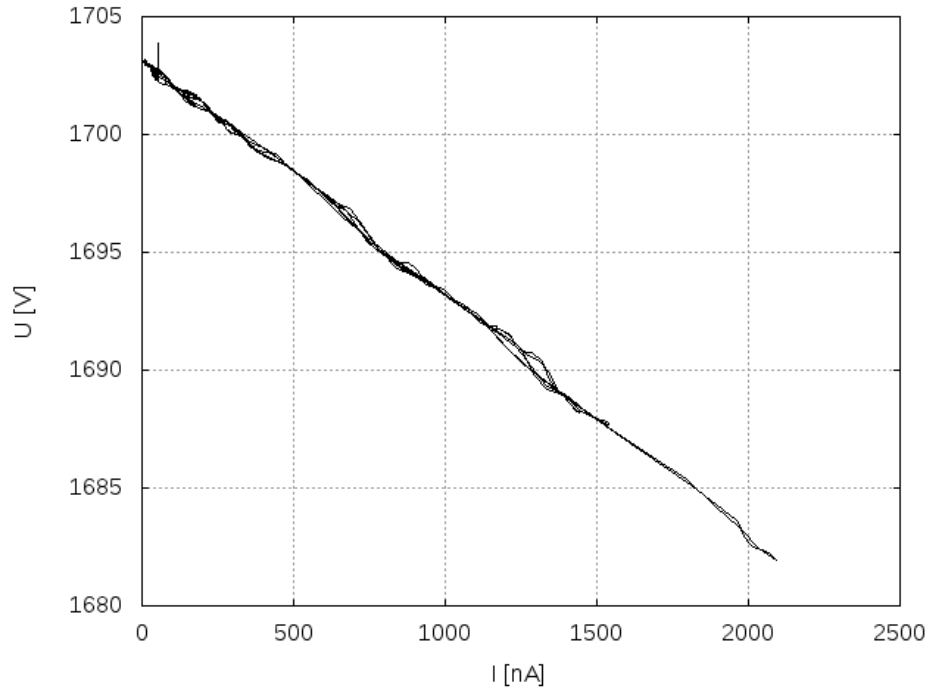


Figure 30. The current as a function of the high voltage.

First let's see the pressure- and temperature correction, the ambient values and the dimensionless functions can be introduced as well as the mean gain values:

$$p_0 = 960 \text{ mbar} \quad (14)$$

$$T_0 = 295 \text{ K} \quad (15)$$

$$T_{dimensionless} = \frac{(T_{measured} + 273) - T_0}{T_0} \quad (16)$$

$$p_{dimensionless} = \frac{(p - p_0)}{p_0} \quad (17)$$

$$\overline{G}_1 = 580 \quad (18)$$

$$\overline{G}_2 = 560 \quad (19)$$

$$\overline{G}_3 = 580 \quad (20)$$

$$\overline{G_4} = 600. \quad (21)$$

To successfully distinguish each part of the effects, special intervals have to be applied where only one of the effects changes and the others are constant. For the pressure, a one week period was selected (08.24. - 08.31.) because the temperature is almost constant, only the daily fluctuation appeared as Figure 28 shows, although the absolute change is around 1% therefore the fitting will be inaccurate. The temperature is a bit complex, because the current drastically raises with it as shown before and in this way the correction would be incorrect. Therefore the first steps of each heat cycle were used where the voltage is not decreased by the current (1. 08.17. - 08.18, 2. 08.31 - 09.01., 3. 09.08. - 09.09.).

As for the linear fitting, the fitted functions will look like:

$$(T(x))_n = (Tm)_n \cdot x + (T0)_n \quad (22)$$

$$(p(x))_n = (pm)_n \cdot x + (p0)_n. \quad (14)$$

where Tm and pm are the slopes, $T0$ and $p0$ are constants and x is the corresponding $\ln G$ values and n is the chamber number. Using the dimensionless parameters and the mean gains the following slopes can be derived:

Num.	Slope T	Std.Err. T	Slope p	Std.Err. p	Mod p
Ch 1	$Tm_1 = 1.873$	$\delta_{T1} = 8.5\%$	$pm_1 = -3.699$	$\delta_{p1} = 3.3\%$	$p_1 = -2.5$
Ch 2	$Tm_2 = 2.500$	$\delta_{T2} = 6.6\%$	$pm_2 = -3.911$	$\delta_{p2} = 3.1\%$	$p_2 = -2.5$
Ch 3	$Tm_3 = 1.956$	$\delta_{T3} = 9.8\%$	$pm_3 = -4.049$	$\delta_{p3} = 2.96\%$	$p_3 = -2.5$
Ch 4	$Tm_4 = 2.411$	$\delta_{T4} = 9.55\%$	$pm_4 = -4.809$	$\delta_{p4} = 4.1\%$	$p_4 = -2.5$

Table 4. The fitted parameters of temperature- and pressure correction and their standard error values for each chamber. Due to the weak accuracy of pressure correction and the strong presence of the current effect modification is needed.

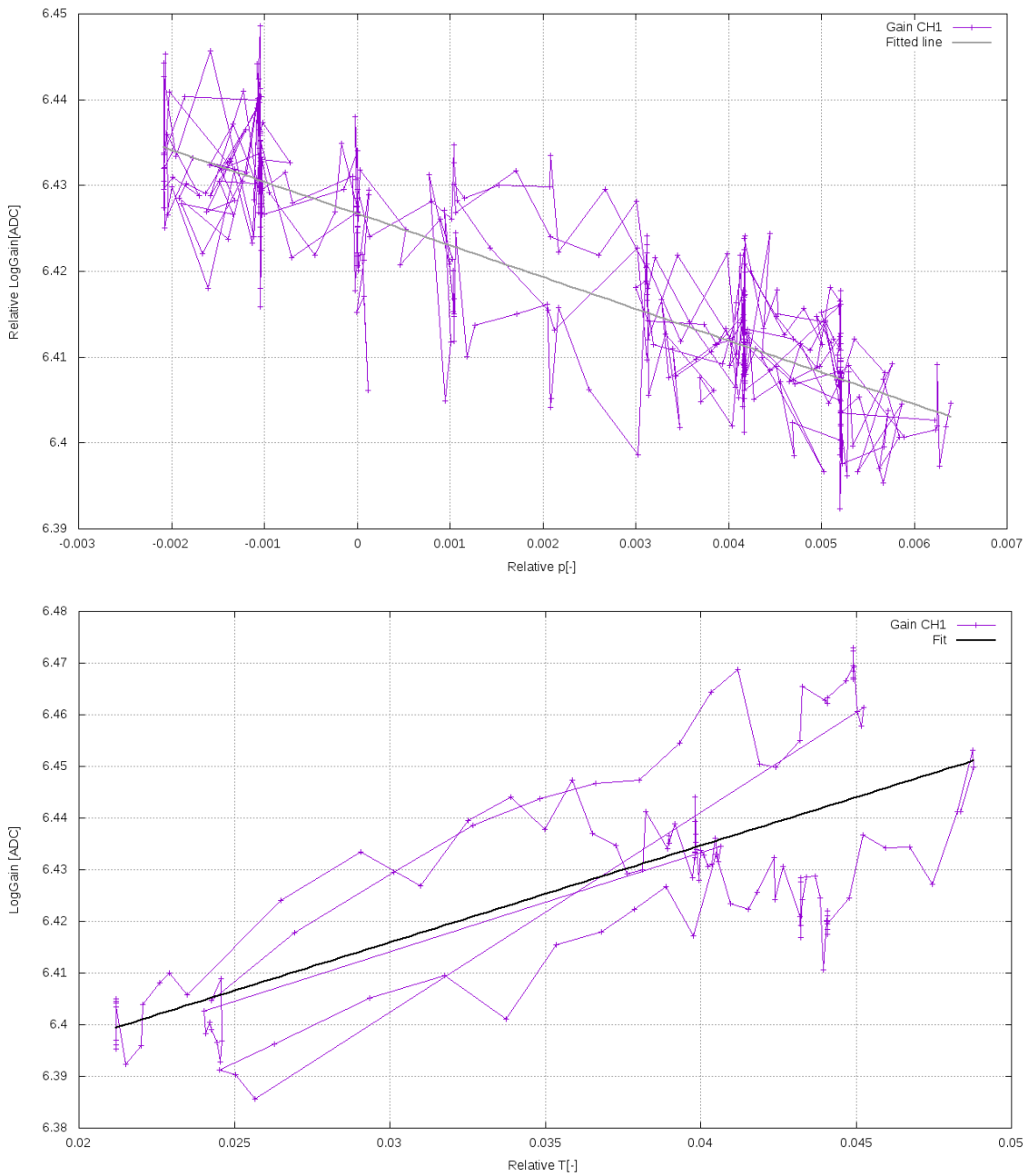


Figure 31. The temperature and pressure correction with the selected data in the case of Chamber 1. The rest can be found in the appendix.

The table shows that the pressure correction had to be modified due to inaccurate fitting regarding to the small changes. The reason behind is, that the pressure only changes by 2% in absolute value (15 mbar) while the temperature around 8% (23 K) thanks to the heat box, thus the temperature correction is much more accurate. Don't

forget about the temperature dependence of the electrical components, which is included in the temperature correction. Figure 32. Shows the applied corrections and the current as the function of temperature the rest can be found in the appendix.

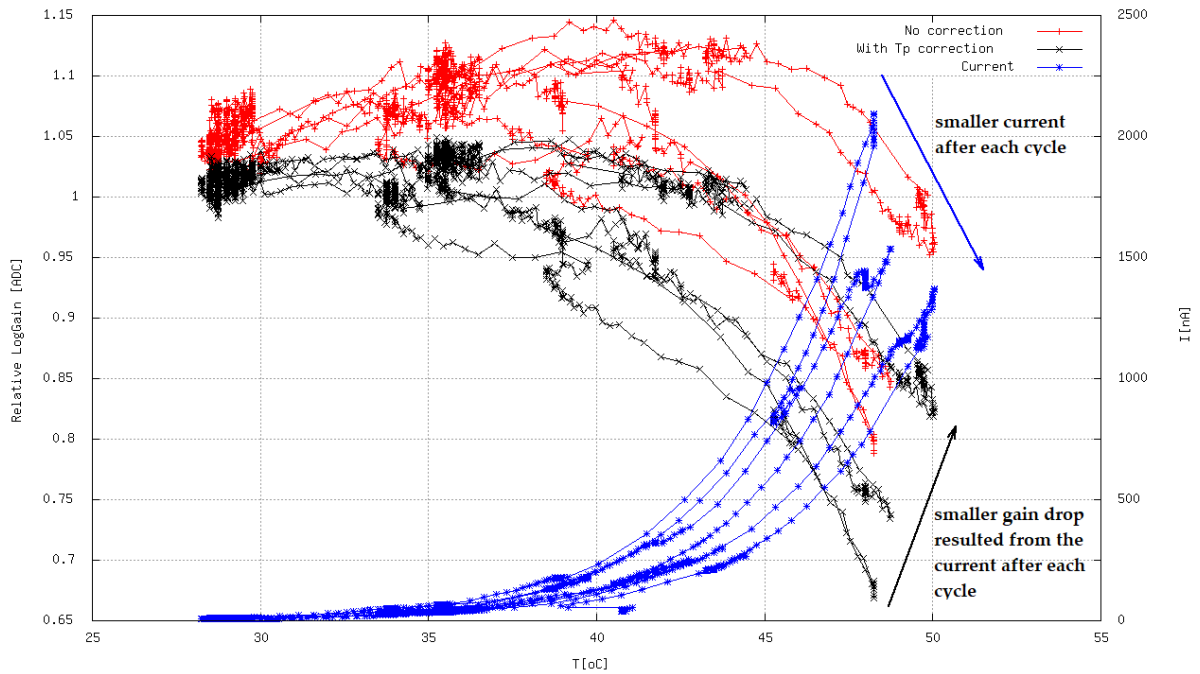


Figure 32. The fitting of the temperature and pressure for the logarithm of the gain as the function of temperature in the case of Chamber 1. After each heat cycle the current is getting smaller and results a lower gain drop. For the other chambers the results can be found in the appendix.

After the correction the gain value is almost constant for a region and starting to decrease significantly in the different cycles after a certain value. Taking the temperatures when the gain decreased by 5% are 37 °C in the first cycle, 41°C in the second cycle and 46 °C in the third cycle. This procedure allows us to moderate the effect of the current on the chambers if we apply a few heat cycles on them. In general a gain drop by 20% does not worsen the efficiency and the track rate and with this method the temperature limit of the system can be increased.

As for the current correction, it can be made with the total current because the different individual values for each chambers are not measured. Therefore some fluctuations remain in the data especially in the high current region. The method is similar to the previous fitting:

$$(I(x))_n = (Im)_n \cdot x + (IO)_n, \quad (24)$$

and the result is shown by Figure 33.

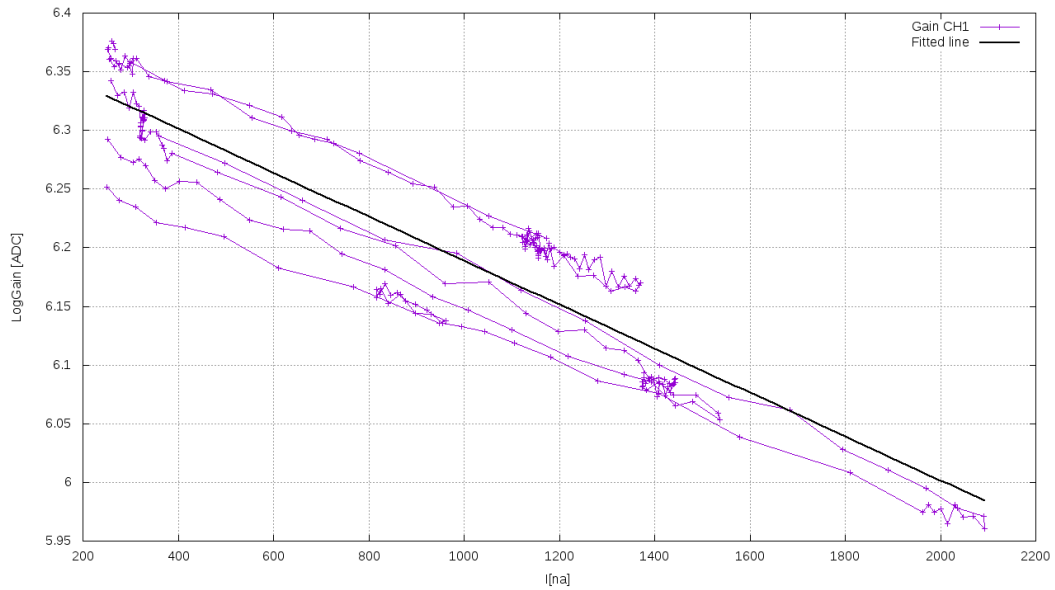


Figure 33. The current correction for Chamber 1 with the total current. The problem is that the total current is not divided equally between the chambers, which results a not fully proper correction. The rest can be found in the appendix.

Using the previous corrected data for the fitting, the total correction is shown by Figure 34 for Chamber 2 and 35 for Chamber 4. The total current correction assumes that the chambers are the same but this is not true unfortunately. Sometimes it is not enough to correct the effect and sometimes it is too much and overcorrection occurs. It is also visible that with higher current the cycles are moving away from each other. The conclusion is that with the previous methods the temperature and pressure can be corrected for any system. Applying heat cycles to the detectors results a “tempering” effect and the temperature limit for the chambers can be increased. As for the current

correction it gives a reasonable result, although the current must be measured individually for the proper correction.

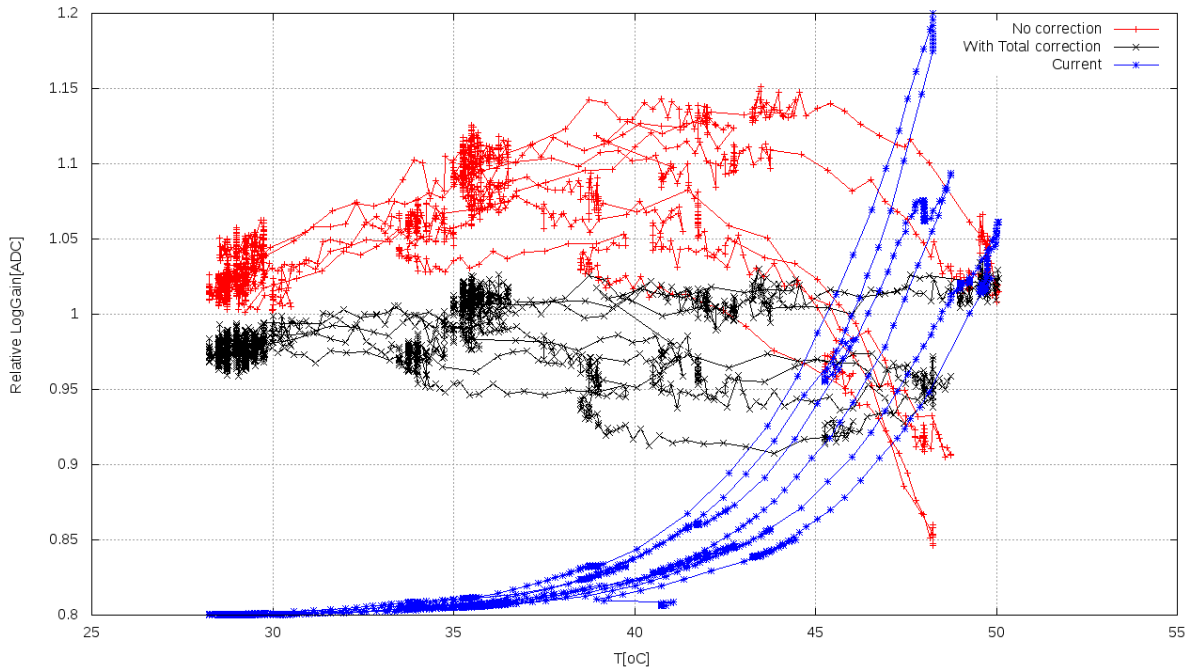


Figure 34. The total correction for Chamber 2. The current correction was not “enough” and the gain tends to be lower at high current values.

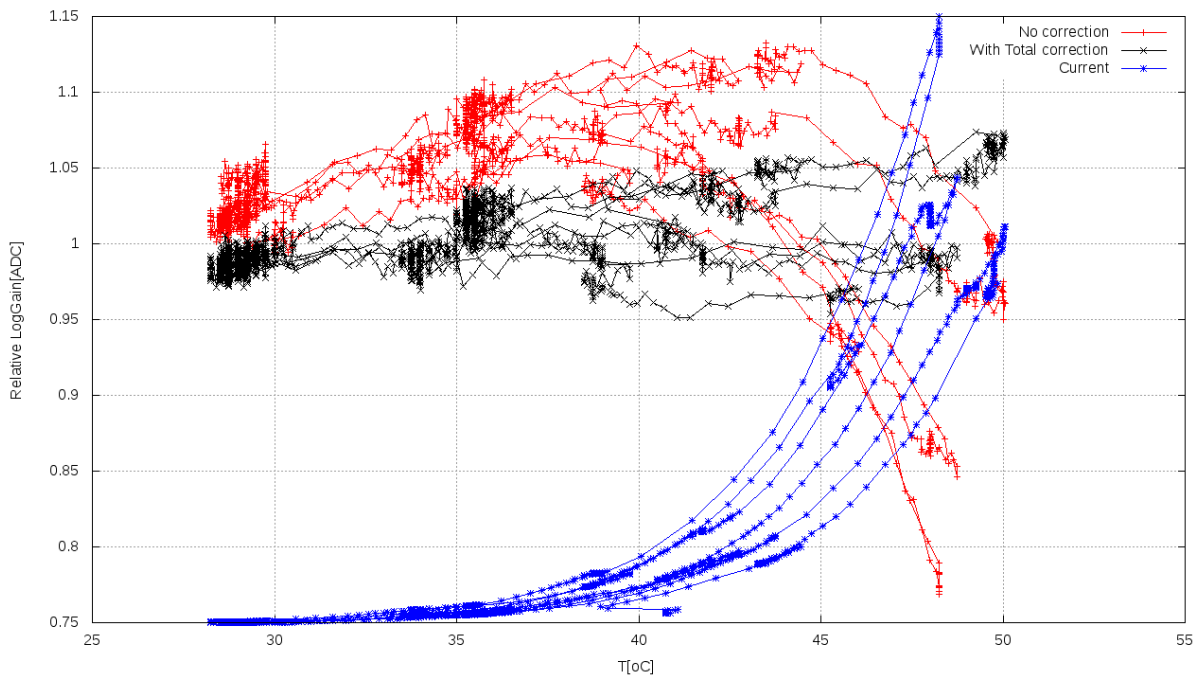


Figure 35. The total correction for Chamber 3. The current correction was “too much” and the gain tends to be higher at high current values.

4. THE PROPERTIES OF THE GLUE

The most important question is that how can we keep the different elements and the gas volume together? For this purpose it is necessary to use some kind of adhesive. In the construction section, I showed the building procedure of a MWPC type detector and the different components that make up the chamber. In the detector development in general there are a lot of experiences and guidance with glues, which fulfil some important basic criteria for a MWPC such as mechanical stability, gas tightness or sufficient dielectric strength to prevent electrical breakdown due to the high voltage.

4.1. Basics of adhesives

Until 1912 the synthetic glues were unknown and the phenolic resins began to spread a few decades later. It was used widely in the wood industry and in the aviation industry later. After 1950 the epoxy resins appeared and propagated fast due to its excellent stress parameters and easy handling. It can be used between different materials and inexpensive compared to other material joining-techniques. In general we can say that gluing has sealing- and vibration damping effect and the thermal- and electrical insulation property. The synthetic polymers - used as adhesives - can be composed by many repeating subunits (monomers) using polymerisation, polyaddition or polycondensation as the process of combining monomers. The basic aspects of these reactions and the adhesives produced by them are the following:

Polycondensation

- Secondary product arise
- Step-growth polymerization, inner products are stable
- The reaction leads to equilibrium
- Phenol formaldehyde resin, amine resin, unsaturated polyester resin, silicon resin

Polyaddition

- Secondary product does not arise
- Step-growth polymerization, inner products are stable
- The composition of the polymer is the same as the monomer
- Each step's activation energy is almost the same
- Polyurethane, epoxy resin

Polymerisation

- Secondary product does not arise
- Chain reaction
- The composition of the polymer is the same as the monomer
- Cyanoacrylate, Polybutadiene and its copolymers

In the detector development, mainly the epoxy resins are dominating. These adhesives can appear with various forms for example flexible or rigid, transparent or coloured and the pot life (the time where the adhesive can be used) can be different as well. Also its attributes can be changed with active components. Many different materials can be joined with it such as metal, wood, ceramic and polymer although the strength of the bond can be different [33, 34]. In this thesis, I mainly focus on the mechanical properties of the adhesive we use and also testing other epoxy and polyurethane glues for comparison. To predict how the adhesive will perform in use, tensile testing was applied to obtain the ultimate tensile strength in the different measurements. In detail these are the following:

1. Testing five different adhesives (four epoxy resin and one PU) between glass reinforced epoxy beams for normal - and shear stress
2. Testing the two component epoxy adhesive that currently used for the chambers with different A:B component ratios for normal stress and investigate the effect of changing ratio for the tensile strength
3. Testing the two component epoxy adhesive that currently used for the chambers between the different materials for normal stress.

The ASTM D3039 standard specifies the test specimen geometry for reinforced composite materials, although I would like to measure the tensile strength of the different adhesives and assume that the weak point of the connection is the glue, and the break will happen there, not in the material. It is reasonable to use the same materials as our group have in the laboratory, therefore the specimens will be different than in the standard. In the first two tests glass fibre reinforced epoxy material is used for every element with a geometry of 10 mm x 20 mm x 400 mm. Figure 36 shows the glued specimens for the testing of normal - and shear stress.

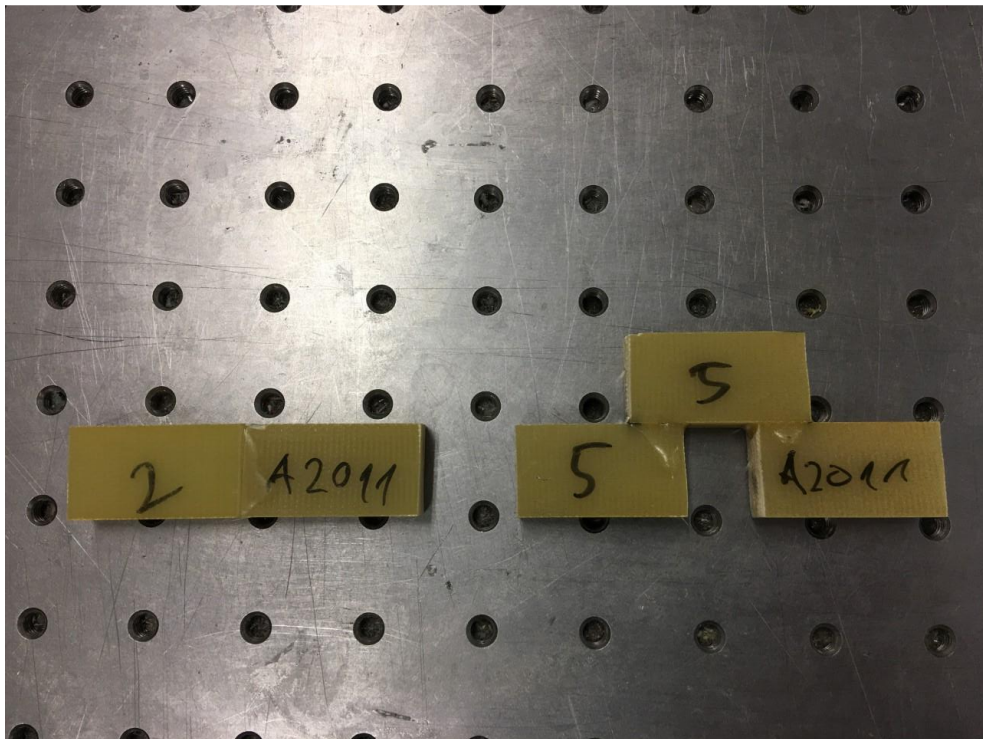


Figure 36. The test specimens for the testing of normal – and shear stress.

The data sheet of the testing machine is the following:

- ZWICK Z005 tensile machine
- Maximal force: 5 kN
- Tensile speed: 200 mm/min.

4.2. Testing of different adhesives

The different adhesives and its technical features are the following:

1. UVERAPID 5 (currently used for the chambers)
 - Mixing ratio of the two components: 1:1
 - Colourless, slightly opaque
 - Pot life: around 5 minutes [35]
2. UVERAPID 20
 - Mixing ratio of the two components: 1:1
 - Slightly claret, transparent
 - Pot life: around 20 minutes [36]
3. SikaPower - 1277
 - Mixing ratio of the two components: 2A : 1B
 - Light red, thixotropic paste
 - Pot life: around 1 hour [37]
4. Sikaflex – 591
 - White silane based polymer
 - Curing speed: $\frac{2mm}{day}$ [38]
5. ARALDITE 2011
 - Mixing ratio of the two components: 1:1
 - Pale yellow, transparent
 - Pot life: around 100 minutes [39].

Three specimens were made for each normal - and shear stress measurement using all of the glues to have information even if something happens with the specimen or the test is not proper. The tensile test results are plotted with the standard force as a function of the strain can be found in the appendix, the ultimate tensile strengths are summarised by Table 5 and Table 6. The contact area in every case:

$$A_{Normal} = 200 [mm], \quad (15)$$

$$A_{Shear} = 100 [mm]. \quad (16)$$

UVERAPID 5	Meas.	Break force [N]		Average [N]		Tensile strength [MPa]	
Normal	1.(Break)	F_{N1}	3634	$\overline{F_N}$	4320	$\overline{\sigma_n}$	21.6
	2.(Break)	F_{N2}	4631				
	3.(No Break)	F_{N3}	4695				
Shear	1.(Break)	F_{T1}	1059	$\overline{F_T}$	839.5	$\bar{\tau}$	4.2
	2.(Break)	F_{T2}	620				
UVERAPID 20							
Normal	1.(No Break)	F_{N1}	4695	$\overline{F_N}$	4536	$\overline{\sigma_n}$	22.7
	2.(Break)	F_{N2}	4377				
Shear	1.(Break)	F_{T1}	1030	$\overline{F_T}$	904	$\bar{\tau}$	4.5
	2.(Break)	F_{T2}	849				
	3.(Break)	F_{T3}	832				
SikaPower - 1277							
Normal	1.(Break)	F_{N1}	4096	$\overline{F_N}$	4244	$\overline{\sigma_n}$	21.2
	2.(Break)	F_{N2}	4392				
Shear	1.(Break)	F_{T1}	1657	$\overline{F_T}$	1230	$\bar{\tau}$	6.2
	2.(Break)	F_{T2}	862				
	3.(Break)	F_{T3}	1173				

Table 5. The calculated ultimate tensile strengths of each adhesive between the G10-G10 material connections from the measurements.

Sikaflex - 591	Meas.	Break force [N]		Average [N]		Tensile strength [MPa]	
Normal	1.(Break)	F_{N1}	228	\overline{F}_N	278	$\overline{\sigma}_n$	1.4
	2.(Break)	F_{N2}	295				
	3.(Break)	F_{N3}	311				
Shear	1.(Break)	F_{T1}	194	\overline{F}_T	194	$\overline{\tau}$	1
Araldite 2011							
Normal	1.(Break)	F_{N1}	4133	\overline{F}_N	4508	$\overline{\sigma}_n$	22.5
	2.(No Break)	F_{N2}	4695				
	3.(No Break)	F_{N3}	4695				
Shear	1.(Break)	F_{T1}	689	\overline{F}_T	655	$\overline{\tau}$	3.3
	2.(Break)	F_{T2}	649				
	3.(Break)	F_{T3}	628				

Table 6. The calculated ultimate tensile strengths based on the measurements of each adhesive between the G10-G10 material connections.

As a conclusion, the epoxy glues behaves quite similar and only the polyurethane adhesive is too weak regarding the mechanical expectations. The other most important selection criterion is the dielectric strength per unit length to avoid too large currents in the chamber. The Araldite 2011 adhesive is commonly used in detector development because it has extreme properties in the sense of resistance (even few hundred teraohms per centimetre), although it is quite expensive compared to Uverapid 5 and 20.

4.3. The testing of UVERAPID 5 with different mixing ratios

In general the mixing ratio always given for a two component adhesive, and it can be achieved accurately with measuring the masses of the parts or with precise mixing tools. Do it by feeling has much more uncertainty but what is actually happening if we apply wrong ratio? It remains the same or the mechanical attributes changes and is the difference symmetrical in both ways? These were the questions before the tensile tests of these specimens. In this measurement only normal stress was applied and the specimens were glued with the currently used Uverapid 5 epoxy adhesive. The mixing ratios are:

	1.	2.	3.	4.	5.
Uverapid A	1	2	1	3	2
Uverapid B	2	3	1	2	1

Table 7. The mixing ratios.

Three specimens were made with each ratio and the tensile results are quite interesting as Figure 37 and 38 show.

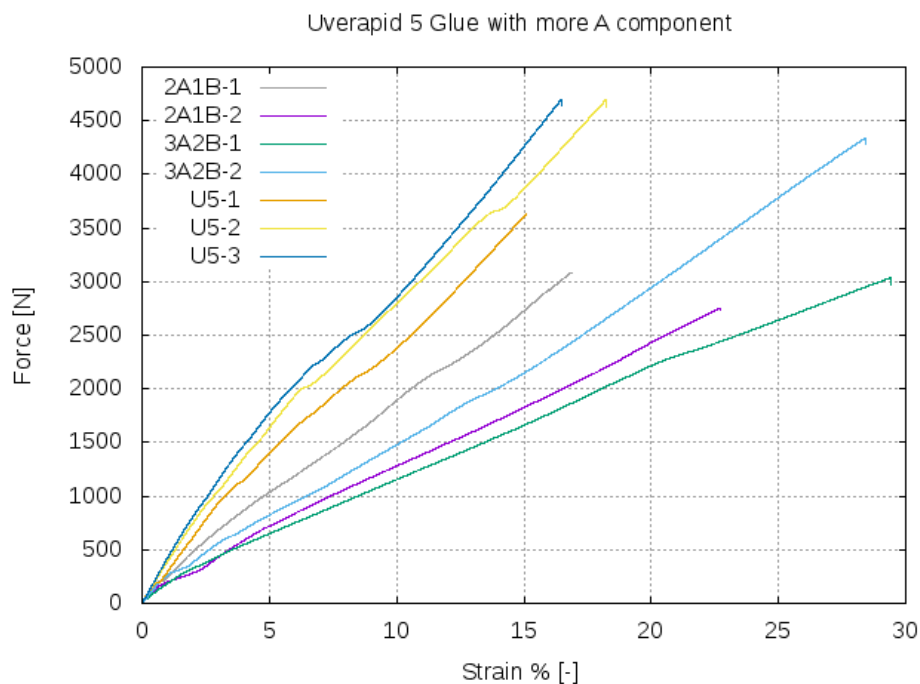


Figure 37. The tensile test of the specimens with more A component.

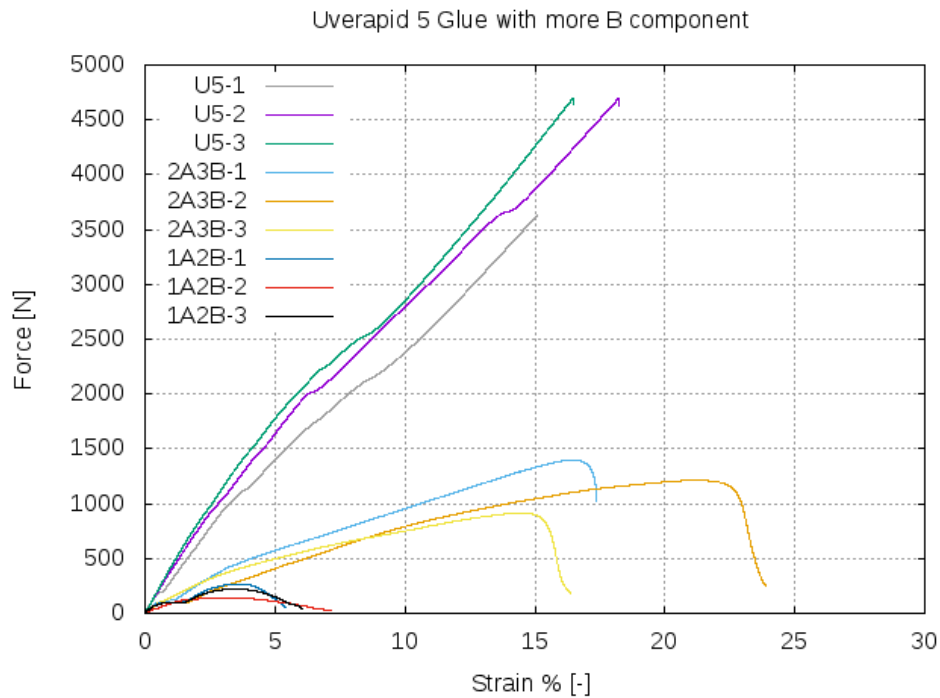


Figure 38. The tensile test of the specimens with more B component

The glue where more A component were present started to get more rigid and the tests show that the ultimate tensile strength is lower by almost a factor of two although it can be used even with the extremely wrong ratio. In the case where more B component were applied the situation is much worse and the glue with the 2:3 ratio is already useless. The glue in this case started to get “rubber-like” and with the extreme ratio the joint turned surprisingly weak. The calculated tensile strength values are summarised in Table 8. The asymmetric effect of the mixing ratio is shown by Figure 39 and the conclusion is that without measuring the ratios precisely it is better to have slightly more A component than B because it will behave almost the same as with 1:1 ratio. In the other case the adhesive will lose its strength rapidly as more and more B component presents.

2A : 1B	Meas.	Break force [N]		Average [N]		Tensile strength [MPa]	
Normal	1.(Break)	F_{N1}	3086	$\overline{F_N}$	2918	$\overline{\sigma_n}$	14.5
	2.(Break)	F_{N2}	2750				
3A : 2B							
Normal	1.(Break)	F_{N1}	3037	$\overline{F_N}$	3688	$\overline{\sigma_n}$	18.4
	2.(Break)	F_{N2}	4338				
1A : 1B							
Normal	1.(Break)	F_{N1}	3634	$\overline{F_N}$	4320	$\overline{\sigma_n}$	21.6
	2.(Break)	F_{N2}	4631				
	3.(Break)	F_{N3}	4695				
2A : 3B							
Normal	1.(Break)	F_{N1}	1397	$\overline{F_N}$	1175	$\overline{\sigma_n}$	5.9
	2.(Break)	F_{N2}	1212				
	3.(Break)	F_{N3}	915				
1A : 2B							
Normal	1.(Break)	F_{N1}	267	$\overline{F_N}$	209	$\overline{\sigma_n}$	1
	2.(Break)	F_{N2}	140				
	3.(Break)	F_{N3}	221				

Table 8. The calculated ultimate tensile strengths based on the measurements for the glues with different mixing ratios.

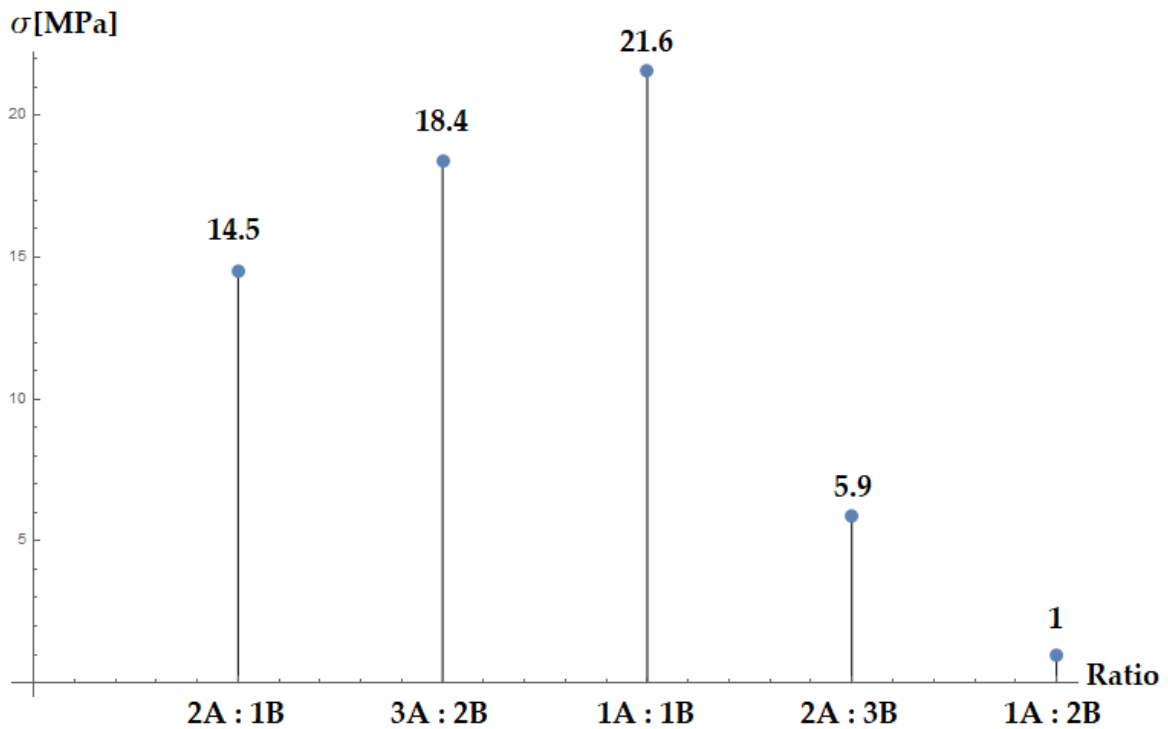


Figure 39. The effect of the mixing ratio to the tensile strength. The asymmetry is clearly visible. It is better to have more A component than B because the weakening is a slight effect comparing to the other way.

4.4. Testing the UVERAPID 5 with different materials

The construction of the chambers requires to join different materials (glass reinforced epoxy elements, copper layered elements, ABS-based polymer pillars) therefore it is a relevant information to know the behaviour of the adhesive between these parts. In section 2.5 I showed the building process of the detectors and it is obvious that the most critical part is the inner support structure. More precisely the adhesive bond between the pillars and the copper layered base plates. The other important relationship is the glass reinforced epoxy and the copper layer that have to be tested. For this purpose, special specimens were made which can be seen on Figure 40. In both cases a small rectangular shape of the base plate material were used, with holes. Unique aluminium holders were manufactured because this rectangular shape is too thin for the

tensile grip to hold it, therefore it was screwed to this aluminium part and in that way the tensile test could be done. The tensile test results are shown by Figure 41.

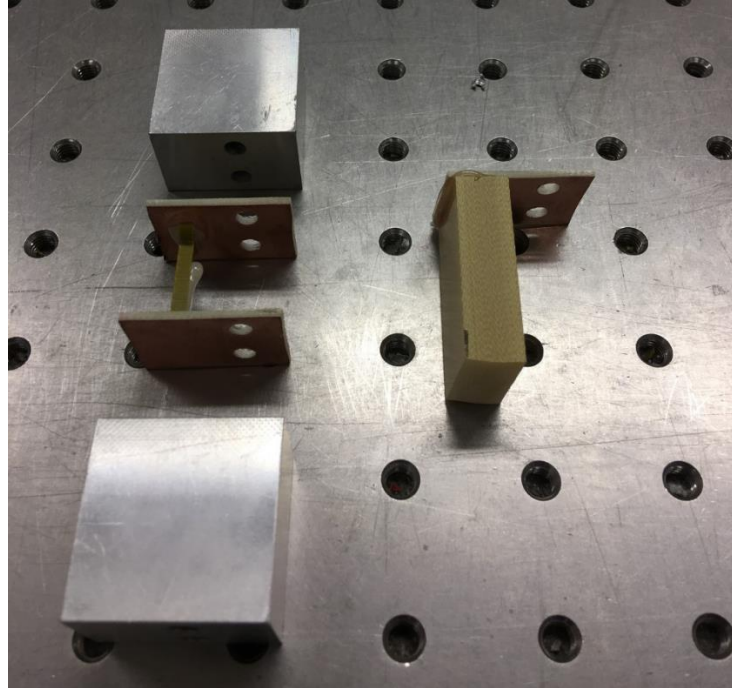


Figure 40. The test specimens with different materials and the aluminium support.

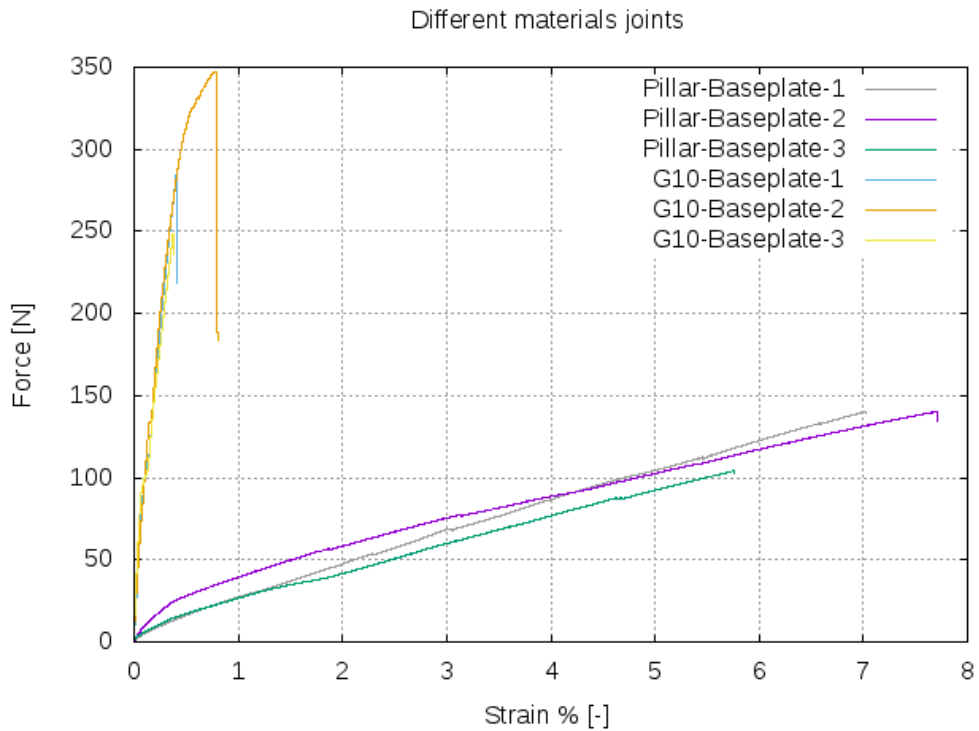


Figure 41. The tensile test of the different material joints.

The calculated values are summarised in Table 9. The corresponding areas are the following:

$$A_{PBP} = 22.4 [mm], \quad (27)$$

$$A_{G10BP} = 200 [mm]. \quad (28)$$

Pillar-base plate	Meas.	Break force [N]		Average [N]		Tensile strength [MPa]	
Normal	1.(Break)	F_{N1}	140	\bar{F}_N	128	$\bar{\sigma}_n$	5.7
	2.(Break)	F_{N2}	140				
	3.(Break)	F_{N3}	104				
G10-base plate							
Normal	1.(Break)	F_{N1}	284	\bar{F}_N	293	$\bar{\sigma}_n$	1.47
	2.(Break)	F_{N2}	347				
	3.(Break)	F_{N3}	248				

Table 9. The calculated ultimate tensile strengths based on the measurements for the different material joints.

These values will be used for comparison in the next section.

5. STUDY OF VIBRATION EFFECTS DURING TRANSPORTATION

In the international collaboration with the Japanese scientists, one of our task and responsibility was the transportation process of the detectors. It is quite a long road from the construction laboratory to the measurement site including land- and air transport. The most important requirements are the following:

- Ensure integrity and safety
- Protection from physical damage
- Easy handling during the transport
- Cost-effective.

Considering these, the boxes are made of oriented strand board (OSB) faces manufactured by an accredited packaging company. Figure 42 shows, that there are pallets fixed below the boxes for the easier handling (lifting with fork-lift).



Figure 42. The transportation boxes for the detectors (left) and the sliced polymer foams inside the box with defined sizes, acting as spacers between the detectors (right).

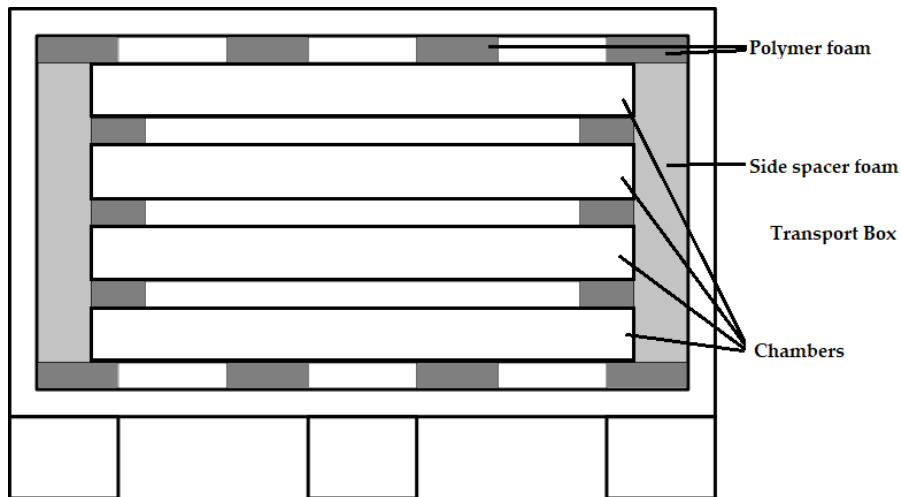


Figure 43. The schematic view of the transportation box after packing. There are usually 4 chambers in one box and polymer foam spacers lay between them.

The polymer foam material has several proper attributes such as the low density, the flexible behaviour and the simplicity of making any kind of shape from them. The role of this spacers is to reduce mainly vibration effects originated from the transportation. Another relevant feature is that the foam can distribute the different loads with their large area and they are not acting on a localized point. Although it is convenient to investigate the behaviour of the detectors during transportation. Mainly the glued parts are interesting, because these are the weak points of the chambers. First, a modal analysis will be performed for one chamber to determine the eigenfrequencies with measurement and Finite Element Method (FEM). After validating the simulation, a random vibration analysis will be carried out, imitating the air transport to achieve the stress field from the vibration and check if the bonded joints are sufficiently strong. These different connections were analysed with tensile testing in Section 4.

5.1. Modal testing of one chamber

In general the modal testing can be used for the characterization of the vibrations and to investigate the dynamic properties of a system in the frequency domain. To build up the mathematical model of a structure, it is necessary to measure the vibration parameters (eigenfrequency, damping, mode shapes etc). In this thesis, modal analysis will be used for a chamber to examine its vibration behaviour and I'm only interested in the vertical direction which is normal to the area of the chamber, denoted by z , because during the transport this is the most dangerous direction. Now I will summarize the theoretical background of the measurement. The equation of motion of the basic model for 1 DoF can be written based on the free body diagram which is shown by Figure 44:

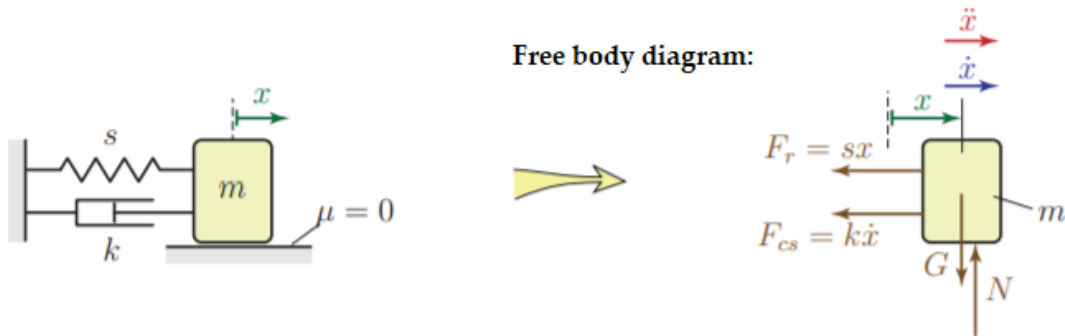


Figure 44. Basic model of the 1 DoF system with damping and the free body diagram. In the international notation k is the stiffness of the spring and c is the damping coefficient [41,42].

$$m\ddot{x} + c\dot{x} + kx = F(t) \quad (29)$$

On the right side $F(t)$ is the force excitation, in my case it will be the impact of the modal hammer. Dividing by the mass and introducing $\frac{c}{m} = 2\zeta\omega_n$, $\frac{k}{m} = \omega_n^2$ we get:

$$\ddot{x} + 2\zeta\omega_n\dot{x} + \omega_n^2x = \frac{F(t)}{m}, \quad (30)$$

where $\zeta = \frac{c}{2\omega_n m}$ is the damping ratio and ω_n is the undamped natural frequency.

Taking the Fourier transformation³ of both sides we obtain:

$$-\omega^2 X(\omega) + 2\zeta\omega_n i\omega X(\omega) + \omega_n^2 X(\omega) = \frac{\Phi(\omega)}{m}. \quad (31)$$

There are alternative forms of Frequency Response Function (FRF) such as dynamic stiffness, receptance, impedance, mobility, etc. The most usual is the receptance which is the ratio of the Fourier transformed output and input signals:

$$\frac{X(\omega)}{\Phi(\omega)} = \frac{1}{m(\omega_n^2 - \omega^2 + i2\zeta\omega_n\omega)} = \frac{1}{k} \frac{1}{(1 - \zeta_{fr}^2 + i\zeta 2\zeta_{fr})}, \quad (17)$$

where $\zeta_{fr} = \frac{\omega}{\alpha}$ the dimensionless frequency. We can calculate the damping ratio by differentiating the real part of the FRF function with ζ_{fr} . In that case a quadratic equation can be formed and the two roots are the peak and notch frequencies, with them the damping ratio can be formed:

$$\zeta = \frac{\zeta_{fr1}^2 - \zeta_{fr2}^2}{2(\zeta_{fr1}^2 + \zeta_{fr2}^2)}. \quad (33)$$

In the literature it is called “peak picking method” and can be applied to multi DoF systems. In the case of n DoF systems the equation of motion is a matrix equation:

$$\mathbf{M}\ddot{\mathbf{x}}(t) + \mathbf{C}\dot{\mathbf{x}}(t) + \mathbf{K}\mathbf{x}(t) = \mathbf{Q}(t). \quad (34)$$

The modal analysis is only good for proportional damping, thus let's assume that the damping is the linear combination of the mass and stiffness matrix:

³ $\Gamma(\omega) = \mathbf{F}(g(t)) = \int_{-\infty}^{\infty} g(t)e^{-i\omega t} dt$

$$\mathbf{C} = k_m \mathbf{M} + k_s \mathbf{K}. \quad (35)$$

The undamped natural frequencies and mode shapes can be obtained from:

$$(-\omega_n^2 \mathbf{M} + \mathbf{K})\mathbf{A} = 0 \rightarrow \omega_{nk}, \mathbf{A}_k. \quad (36)$$

Using the “orthogonality” of the mode shapes:

$$\mathbf{A}_i^T \mathbf{M} \mathbf{A}_j = 0, \quad \mathbf{A}_i^T \mathbf{K} \mathbf{A}_j = 0, \quad (37)$$

the modal transformation can be introduced:

$$\mathbf{T} = [c_1 \mathbf{A}_1 \quad c_2 \mathbf{A}_2 \quad \dots \quad c_n \mathbf{A}_n], \quad c_n = \frac{1}{\sqrt{\mathbf{A}_k^T \mathbf{M} \mathbf{A}_k}}, \quad \mathbf{x} = \mathbf{T} \mathbf{y}, \quad (38)$$

applying it to the equation of motion and multiplying with \mathbf{T}^T from the left results:

$$\mathbf{I} \ddot{\mathbf{y}} + [2\zeta_k \omega_{nk}] \dot{\mathbf{y}} + [\omega_{nk}^2] \mathbf{y} = \mathbf{T}^T \mathbf{Q}(t), \quad (39)$$

where \mathbf{I} is the identity matrix.

Making the Fourier transformation as before, the receptance can be formed. In the measurement we get the same matrix in the following way:

- In the i^{th} row there is the spectrum of the excitation
- In the j^{th} column there is the spectrum of the output signal [41,42]

$$\frac{X_i(\omega)}{\Phi_j(\omega)} = \begin{bmatrix} \frac{X_1}{\Phi_1} & \frac{X_2}{\Phi_1} & \dots \\ \frac{X_1}{\Phi_2} & \frac{X_2}{\Phi_2} & \dots \\ \dots & \dots & \dots \end{bmatrix}. \quad (40)$$

In my case the acceleration values will be used because the vertical scale is not important, only the horizontal location. It is enough to excite the system in one point, because all of the modes getting excited at the same time if that one point is not a node. In the measurement I used a classical approach and excited the detector with a modal hammer as Figure 45 shows. A 10 cm x 10 cm grid were made before the actual measurement as possible points to one quarter of the detector. Accelerometer B was put to the middle and accelerometer A to point 7 with coordinates [20 cm, 20 cm]. With the hammer four different measurement points were excited three times each, shown by Table 10.

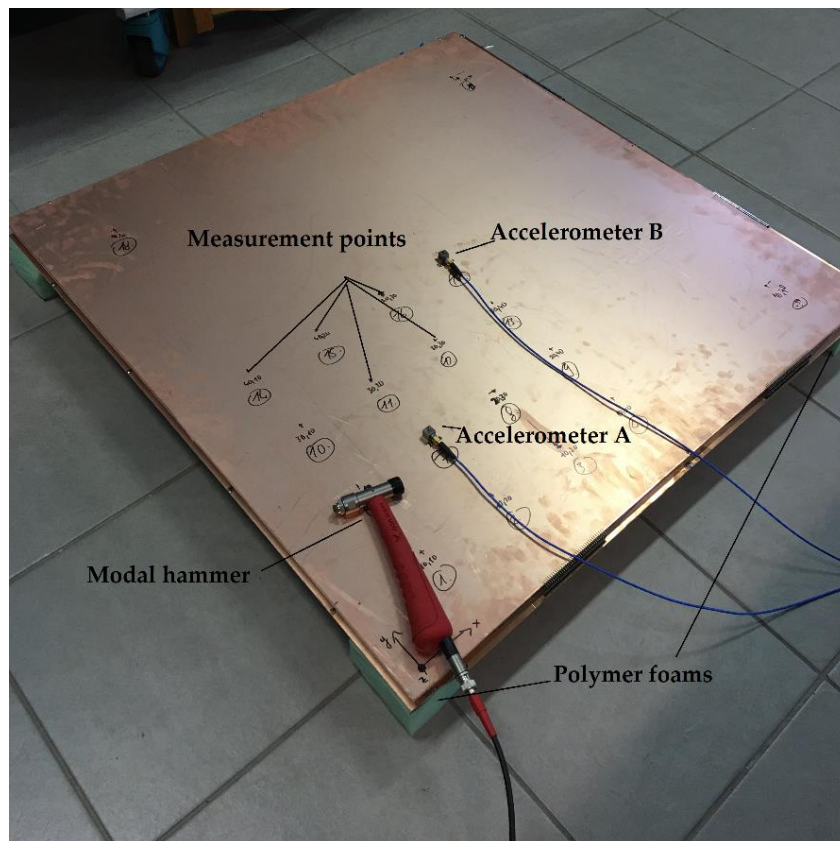


Figure 45. The measurement setup with the modal hammer and the two accelerometers. Each of them can measure in x,y,z direction. A detector without any electronics was used. The $[0, 0]$ point is located in the bottom left corner.

Hammer	Accelerometer A	Accelerometer B
1 [10,10]	7 [20,20]	17 [40,40]
11 [20,30]		
12 [30,30]		
17 [40,40]		

Table 10. The different measurements for the natural frequencies. Each layout was measured three times. The coordinate unit is in cm and measured from the bottom left of the detector. In the last measurement the impact was next to accelerometer B. Four polymer foams were placed under the detector at each corner to imitate the transportation conditions although in the real box there are foams also at the half of each side. To measure the signals of the hammer and the two accelerometers, they were connected through a compact DAQ system to a PC. The accelerometers were calibrated with a Brüel & Kjaer type exciter, which can be seen on Figure 46.

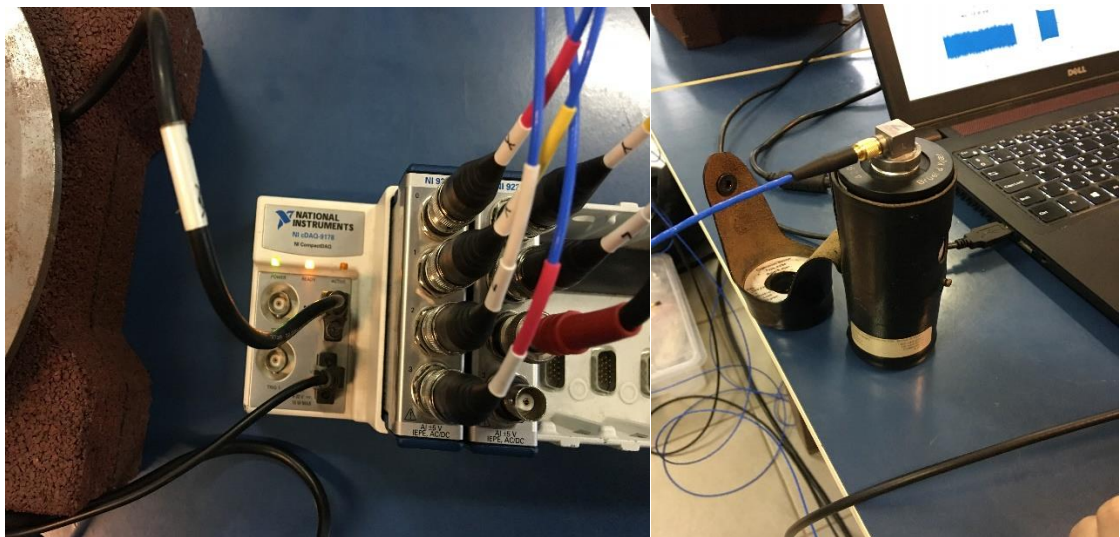


Figure 46. The compact DAQ - NI cDAQ-9178) (left) and the calibration exciter – Brüel & Kjaer type 4294 (right).

To visualize, the input and output signal can be seen on Figure 47 for measurement 23, the rest can be found in the appendix.

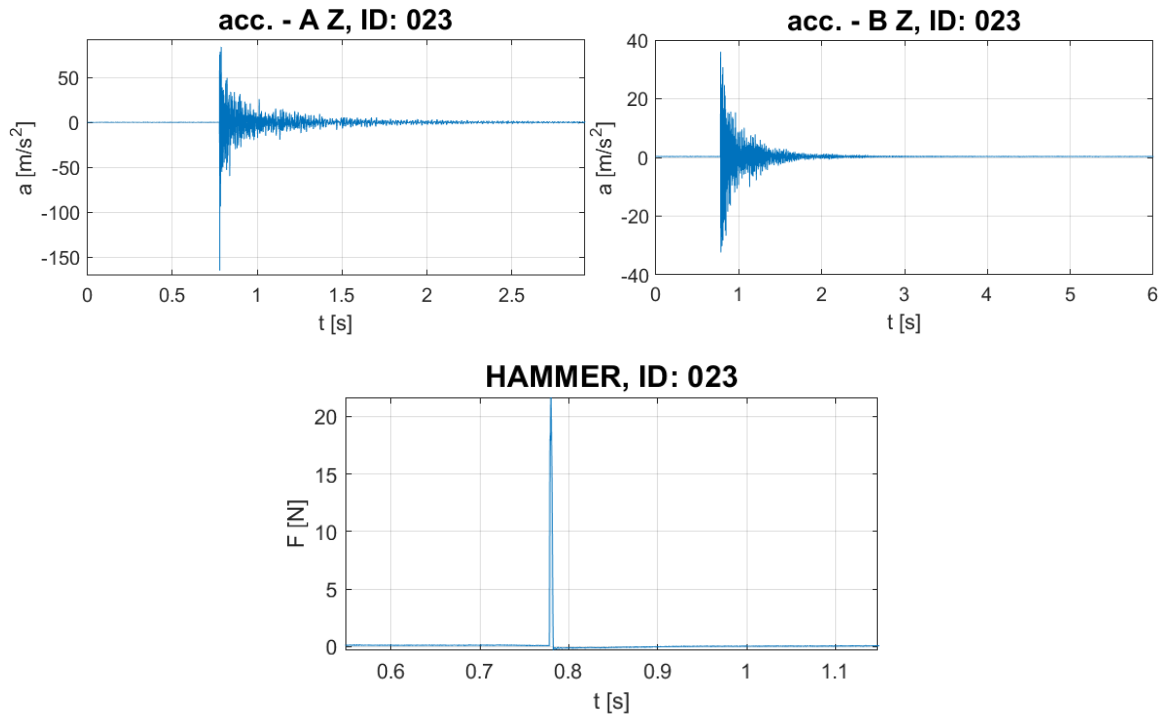


Figure 47. The output signal from the accelerometer and the input signal from the hammer. In ideal case the impact would be a Dirac-delta excitation, in reality it is finite and I paid attention to avoid the prall effect (multiple hit).

After making the Fourier transformation of every measurement, the eigenfrequencies will appear as peaks. Plotting all the foam measurements it looks like:

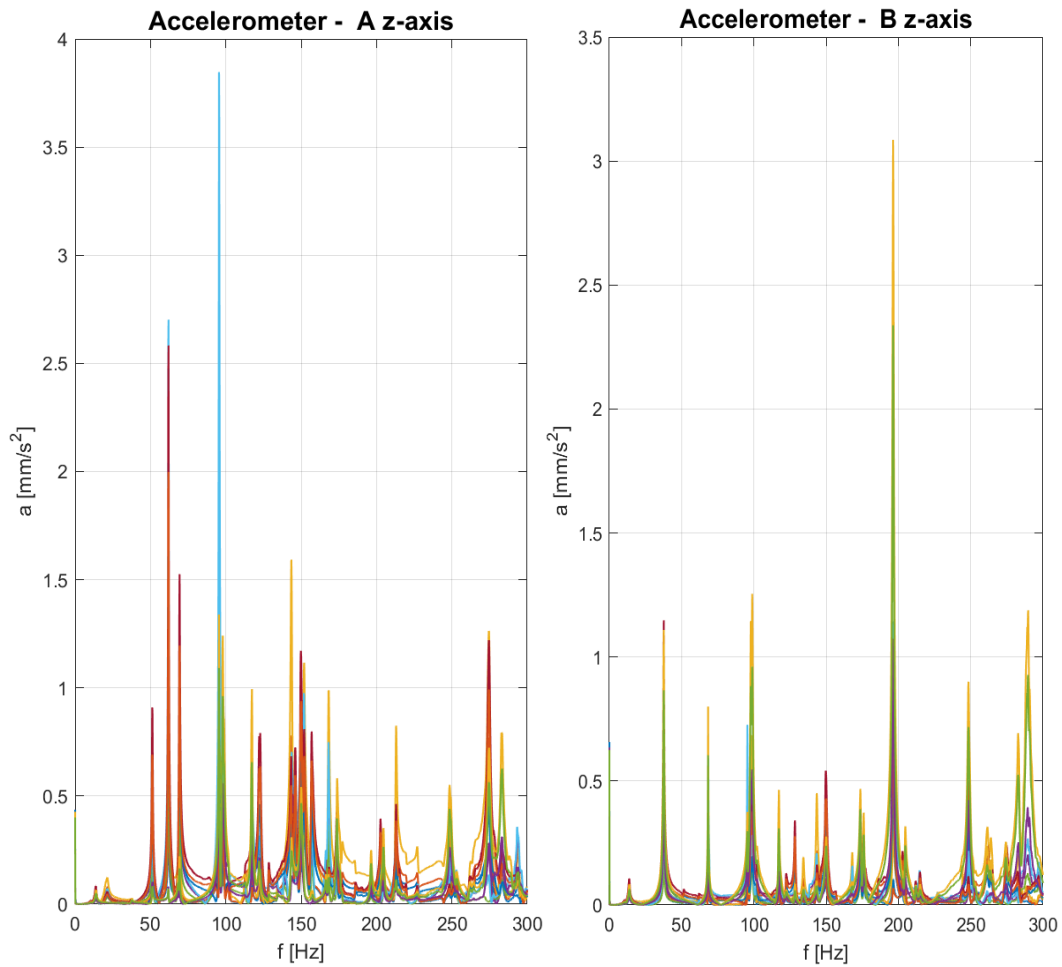


Figure 48. The FFT of the frequency response function of all the foam measurements at the two accelerometers.

Collecting the first few eigenfrequencies it is summarised in Table 11.

Accelerometer A FFT [Hz]	Accelerometer B FFT [Hz]
$f_1 = 13.667$ Hz	$f_1 = 13.883$ Hz
$f_2 = 21.333$ Hz	$f_2 = 37.667$ Hz
$f_3 = 37.667$ Hz	$f_3 = 51.5$ Hz
$f_4 = 51.167$ Hz	$f_4 = 62$ Hz
$f_5 = 62$ Hz	$f_5 = 68.333$ Hz

Table 11. The first few eigenfrequencies of the system. It seems that the second frequency in accelerometer A was not excited in the case of accelerometer B. The other frequencies are in a very well agreement.

Another modal testing was made with aluminium spacers instead of the foam to validate the measurement. The results can be seen in Table 12.

Accelerometer A FFT [Hz]	Accelerometer B FFT [Hz]
$f_1 = 21.5$ Hz	$f_1 = 21.5$ Hz
$f_2 = 33.3$ Hz	$f_2 = 33.5$ Hz
$f_3 = 44.83$ Hz	$f_3 = 45$ Hz
$f_4 = 57.33$ Hz	$f_4 = 57.33$ Hz
$f_5 = 64.17$ Hz	$f_5 = 64$ Hz

Table 12. The modal testing with aluminium cylinders, the frequencies are similar than before, just the eigenfrequency of the support changed.

In order to estimate the damping ratio for the further simulation, let's look at the solution in time for a slightly damped 1DoF system using equation (30) with the right hand side equal to 0. After some transformation we can get [41]:

$$x(t) = Ae^{-\zeta\omega_n t} \sin(\gamma t + \varepsilon) \quad [41], \quad (41)$$

where $\pm Ae^{-\zeta\omega_n t}$ is the envelope curves, A is the extremum of the envelope curve, γ is the damped angular natural frequency, ε is the phase offset. For the estimation this approach can be used, assuming that the largest amplitudes are coming from the first eigenfrequency and defining the damping ratio with that for the system. Choosing the proper damping ratio value, the envelope curves can be plotted for my measurement, as Figure 49 shows:

$$\zeta_{est} = 0.02.$$

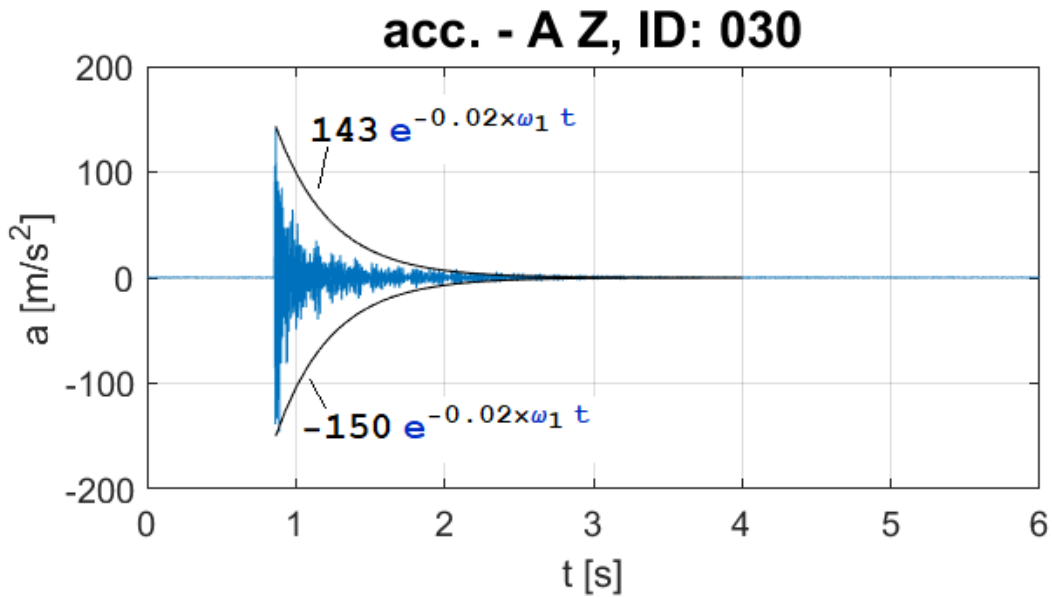


Figure 49. The envelope curves with $\zeta_{est} = 0.02$ for measurement 30, using the first eigenfrequency. To be on the safe side this value will be used for the further calculations.

5.2. Simulation of the transportation with random vibration

5.2.1. MODAL ANALYSIS

For the Finite element simulation I used the ANSYS Workbench 2020 R2 software where the materials were added with the following properties:

- FR-4/G10 (The base plates, the wire holder elements and the beams)
 - $\rho = 2000 \left[\frac{kg}{m^3} \right]$
 - $E_x = 20.4 [GPa], E_y = 18.4 [GPa], E_z = 15 [GPa]$
 - $\nu_x = 0.11 [-], \nu_y = 0.09 [-], \nu_z = 0.014 [-]$
- ABS-based 3D printer filament (support pillars)
 - $\rho = 1250 \left[\frac{kg}{m^3} \right]$
 - $E = 1.85 [GPa]$.

Like in the modal testing, in the simulation a detector without any electronics was used. The mass was measured previously by a scale with 0.1 kg accuracy:

$$m_{chamber} = 7.0 [kg].$$

To validate the model two properties have to be fulfilled:

- The mass should not differ more than 5%
- The first few eigenfrequencies should not differ more than 10%.

After setting the parameters, the model of an MWPC-80 previously created was imported into the software. The calculated mass and the error can be obtained:

$$m_{software} = 6.63 [kg] \quad (42)$$

$$\delta_{mass} = \frac{m_{chamber} - m_{software}}{m_{chamber}} = 5.3\%. \quad (43)$$

Considering that the glue is not modelled it is acceptable. The simulation structure is shown by Figure 50.

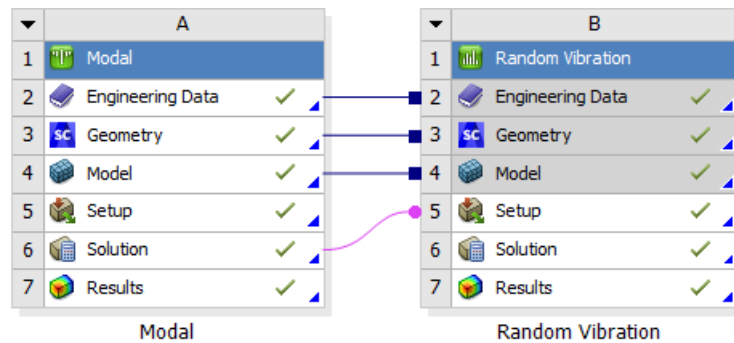


Figure 50. The simulation structure

First I used the Modal analysis system and connected with the Random Vibration module to acquire the stresses from the vibrations. The element type was the general SOLID 186, which is a 20-node, 3DoF per node element and the degrees are the x,y,z displacements. For the mesh the multizone method was applied where uniform hexa domains builds up the model. The first validation of the model neglects the numerical errors comes from the density of the mesh, therefore a mesh dependence study was performed. The number of elements in the dense and coarse meshes are:

$$N_{dense} = 3402 \quad , N_{coarse} = 1784, \quad (44)$$

and the first eigenfrequencies with them:

$$f_{1,dense} = 12.338 [Hz] \quad , f_{1,coarse} = 12.361 [Hz]. \quad (45)$$

Thus the error is:

$$\delta_{mesh} = \frac{f_{1,dense} - f_{1,coarse}}{f_{1,dense}} = 0.19 \%, \quad (46)$$

that is less than 1% therefore the simulation is independent from the mesh.

In the model the foams are represented with a spring at the four corners as Figure 51 shows.

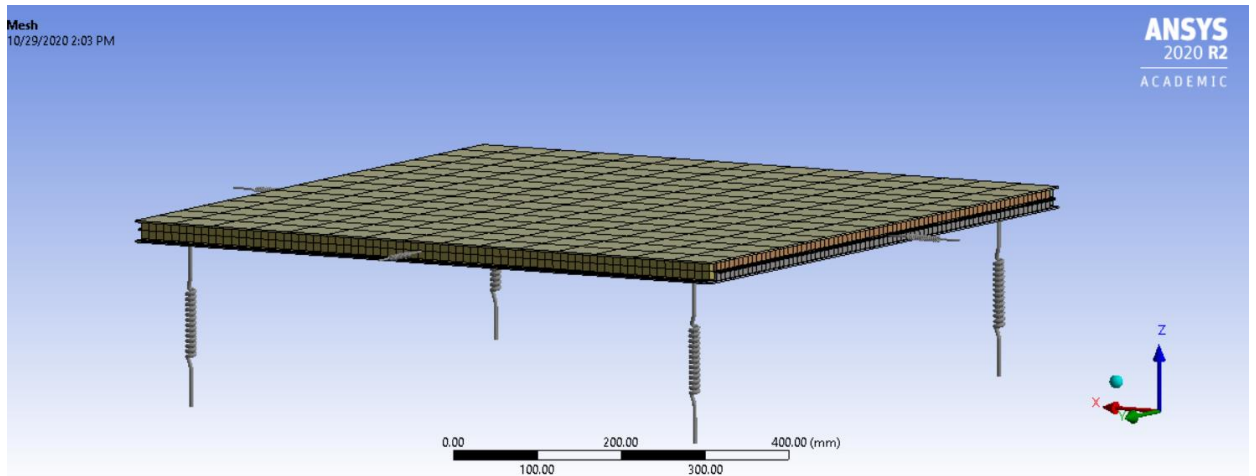


Figure 51. The meshed model with the springs at the corners. Further springs were added to each side at the x - y plane to prevent the rigid body motion, the eigenfrequencies in the z direction are the same.

The next step was to estimate the stiffness of the foam where the eigenfrequencies are in a good agreement with the measured values. For this purpose a very simple measurement was done to determine just the order of the stiffness and with adjustment in

the model the correct value could be added. It is shown by Figure 52 where the foam was placed between two plates to acquire uniform load. After that equal weights with known masses were put on the top and I measured the displacement.

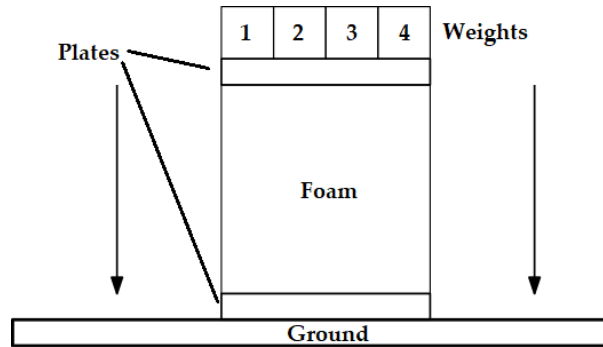


Figure 52. The simple measurement for the estimation of the stiffness.

Force [N]	Displacement [mm]	Stiffness [N/mm]
$F_1 = 6.94 \text{ N}$	$d_1 = 1 \text{ mm}$	$k_1 \approx 7 \text{ N/mm}$
$F_2 = 13.87 \text{ N}$	$d_2 = 2.5 \text{ mm}$	$k_2 \approx 5.5 \text{ N/mm}$
$F_3 = 17.34 \text{ N}$	$d_3 = 3.5 \text{ mm}$	$k_3 \approx 5 \text{ N/mm}$
$F_4 = 27.74 \text{ N}$	$d_4 = 24.5 \text{ mm}$	$k_4 \approx 1 \text{ N/mm}$

Table 13. The estimation of the stiffness values for the foam. It has a non-linearity with degressive characteristics. It is another interesting task that what happens after an impact, can the foam compressed that much and get into that state?

I'm only interested in the first part of the characteristic, which resulted a stiffness around a few N/mm so this order can be used in the model. At the end, the correct stiffness value was adjusted to the frequencies:

$$k = 11 \left[\frac{N}{mm} \right]. \quad (47)$$

The results from the simulation are summarised by Table 14.

Simulation [Hz]	Modal testing (Average value from A and B) [Hz]	Error
$f_{1,FEM} = 12.798$ Hz	$f_{1,MEAS} = 13.775$ Hz	$\delta_1 = 7.1$ %
$f_{2,FEM} = 23.258$ Hz	$f_{2,MEAS} = 21.333$ Hz	$\delta_2 = 9$ %
$f_{3,FEM} = 38.83$ Hz	$f_{3,MEAS} = 37.667$ Hz	$\delta_3 = 4$ %
$f_{4,FEM} = 39.502$ Hz		
$f_{5,FEM} = 55.214$ Hz	$f_{4,MEAS} = 51.335$ Hz	$\delta_4 = 7.6$ %
$f_{6,FEM} = 66.038$ Hz	$f_{5,MEAS} = 62$ Hz	$\delta_5 = 6.5$ %
$f_{7,FEM} = 74.07$ Hz	$f_{6,MEAS} = 68.33$ Hz	$\delta_6 = 8.4$ %

Table 14. The results from the simulation and the modal testing. It seems that the third and fourth frequencies are too close to each other and it could not be seen in the FFT.

The conclusion is that the simulation is validated because the criteria for the mass and the first six eigenfrequencies are achieved. The mode shapes can be found in the appendix.

5.2.2. RANDOM VIBRATION

In general the random vibration is the most complex type of vibration where both the input and output signals characterized by random approach. D.J.Ewins specifies the method to calculate the Auto- or Power Spectral Density (PSD) or even Cross Spectral Density (CSD) for a pair of function. [40] The PSD is useful when the resonances and harmonics are hidden in the time data and if we want to know where the energy lies. It is similar to the FFT although has a unique property that it is normalized to the frequency bandwidth. It can be formulated as:

$$S_h(\omega) = \lim_{T \rightarrow \infty} \frac{1}{2T} \left| \int_{-T}^T h(t) \cdot e^{-i\omega t} dt \right|^2, \quad (48)$$

where

- $\int_{-T}^T h(t) \cdot e^{-i\omega t} dt$ is the Fourier transform of the signal
- The absolute value and the power of two results $|H|^2$
- The $\frac{1}{2T}$ with the limit gives the “density” [42].

Of course $h(t)$ can be acceleration, velocity, displacement and even “g” acceleration. In my case the ASTM D 4169 standard was used which defines the performance testing of shipping containers and systems. In this standard well-detailed methods are given for uniform basis of evaluating the ability of transportability. The test plan consist of many steps which investigating if the equipment withstand the environmental challenge. In the cycle I’m only interested in the vibration part and assume that sudden impacts won’t appear or will appear but won’t damage the system during the transportation [43]. This standard refers to a test method which is discussed at ASTM D 4728 standard. It covers the random vibration testing of shipping units and determines the measurement techniques related to the performance of the container. Also the development and use of vibration data is discussed [44]. For the simulation I used PSD from “g” acceleration data where different assurance levels defined for the particular transportations (road,railway,air). To be on the side of safety, assurance level 1 was used which is a high level of test intensity and has a low probability of occurrence. The properties of this PSD can be found in Figure 53 and 54.

Test conditions

	ASSURANCE LEVEL 1	ASSURANCE LEVEL 2	ASSURANCE LEVEL 3
Frequency Range	2-300Hz	2-300Hz	2-300Hz
Amplitude	1.487 Grms	1.052 Grms	0.7437 Grms
Displacement	11.17 mm peak to peak	7.901 mm peak to peak	5.587 mm peak to peak
Velocity	0.2457 m/s pk	0.1737 m/s pk	0.1229 m/s pk
Z-Axis	3 Hours runtime	3 Hours runtime	3 Hours runtime

Air:

Frequency, Hz	Power Spectral Density Level, g^2/Hz		
	Assurance Level I	Assurance Level II	Assurance Level III
2	0.0004	0.0002	0.0001
12	0.02	0.01	0.005
100	0.02	0.01	0.005
300	0.00002	0.00001	0.000005
Overall, g rms	1.49	1.05	0.74
Duration, min ^B	180	180	180

Figure 53. The definition of the g acceleration PSD with the frequency range and the amplitude (Reference: <https://jtlamerica.com/services/vibration-testing/testing-standards/>).

Test profile: ASTM D4169-16 AIR Assurance Level 1

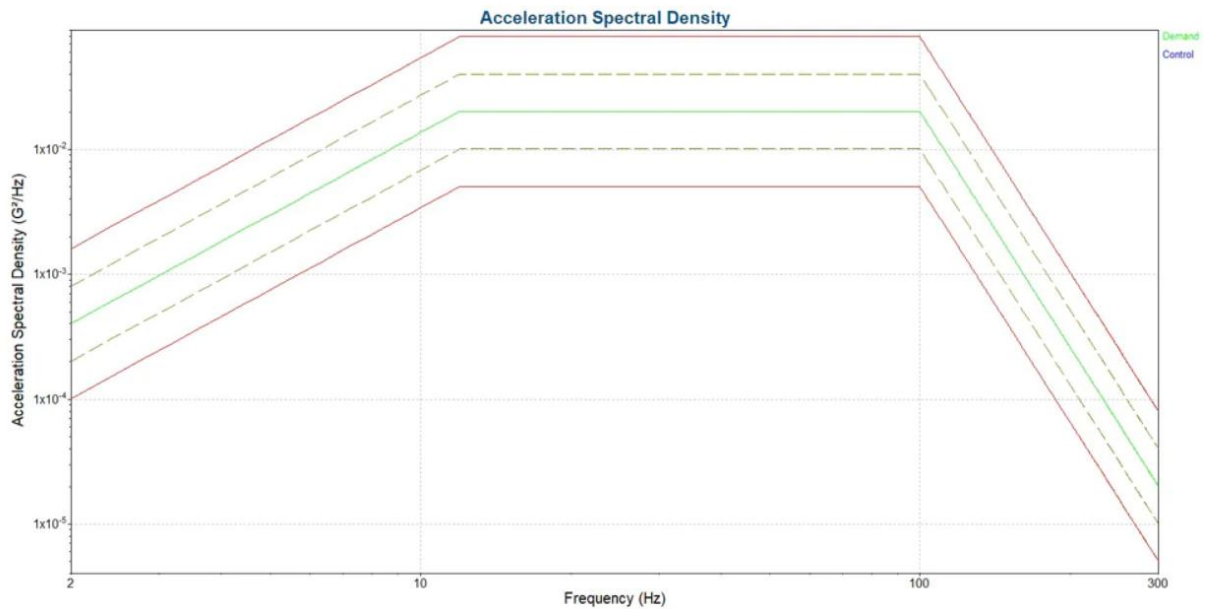


Figure 54. The test profile (Reference: <https://jtlamerica.com/services/vibration-testing/testing-standards/>)

The lack of the fatigue test implies that a quite conservative approach must be used during the simulation to somehow connect the “static” and the “dynamic” measurements. I would like to summarise these:

- The test profile is the highest level of assurance as was shown before
- The scale factor or coincidence interval is the highest (3σ or 99.73%)
- The applied damping ratio is low $\zeta = 0.02$ estimated from the modal analysis (I also checked in the literature the value which is used in the industry for initial guessing when there is no information about the damping[45,46,47,48] and it is around 0.02).
- Much more foams are used in the real transport box
- It is a one-time transportation to the measurement site
- Impacts are not included.

With these restrictions the simulation presumes a quite “dangerous” case, because I want to be on the side of safety and to say something from the tensile testing and the random vibration. Figure 55 shows the model and the imported assurance level.

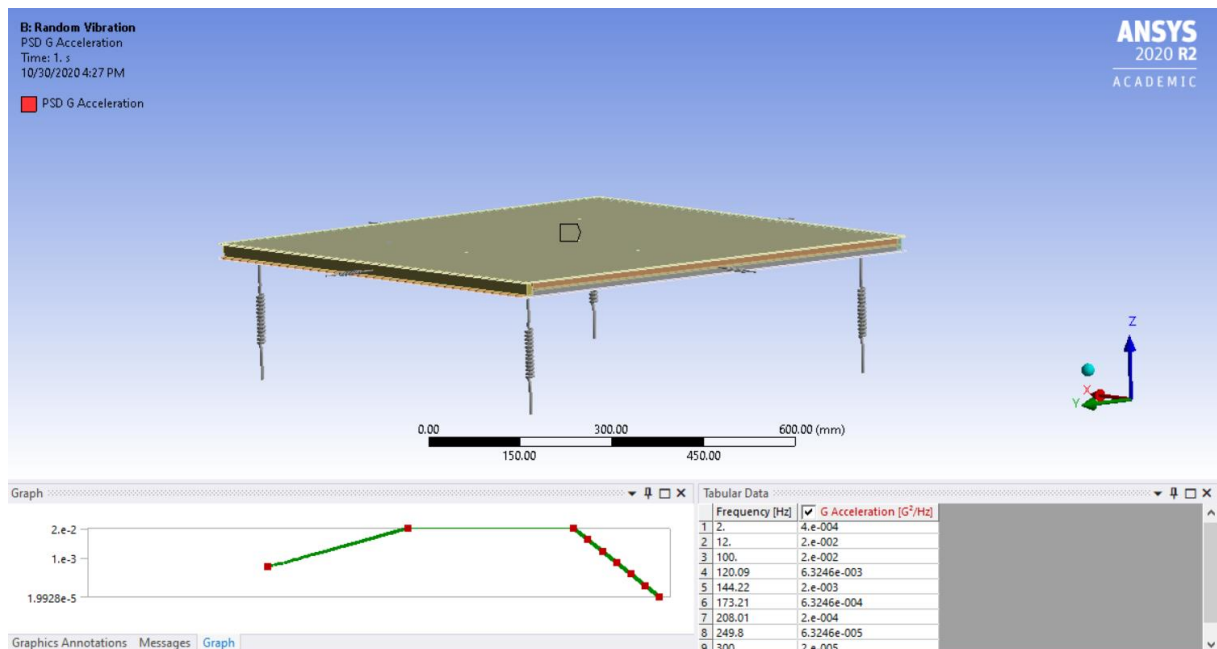


Figure 55. The model and the applied assurance level.

I'm interested in the stresses in the z direction and its effect on the glue. The reason why the glue is not modelled because the stresses can be determined with the bonded contact at each connection where the parts are glued together. These connections are:

- G10 beam – base plate
- FR4 support electronics – base plate
- FR4 support electronics – G10 beam
- ABS support pillar – base plate.

Every different connection was tested with tensile testing as was shown at Section 4. In the simulation these stress values were set at the solution part, although the weakest point of the detector is the support pillar – base plate relationship, therefore all of the pillars were investigated at the top and the bottom side. Figure 56 shows the notation for the pillars and Table 15 shows the maximal values of σ_z .

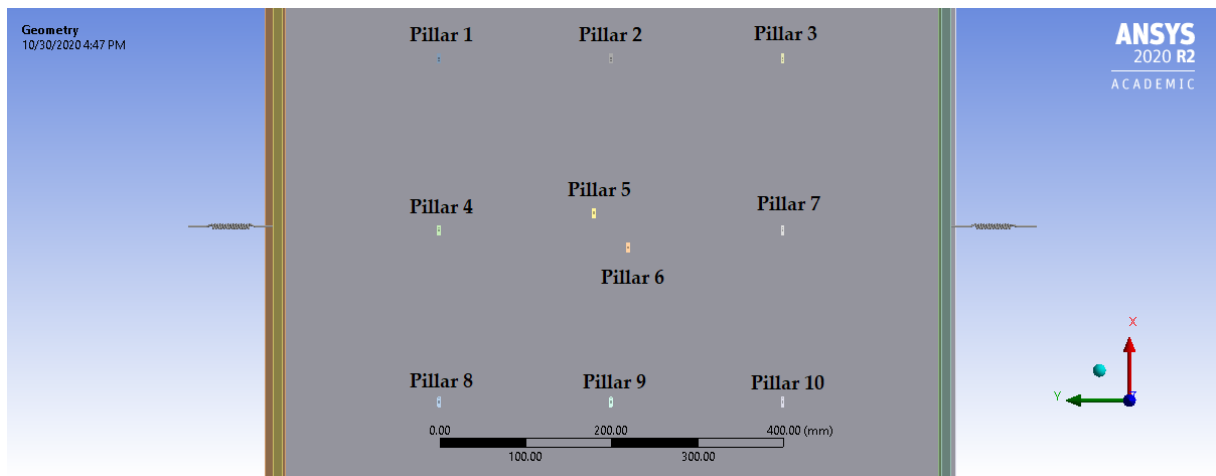


Figure 56. The notation for the pillars.

Location	Stress [MPa]	Stress [MPa]
Pillar 1	$\sigma_{z,max}^{top} = 1.63$ MPa	$\sigma_{z,max}^{bottom} = 1.35$ MPa
Pillar 2	$\sigma_{z,max}^{top} = 1.09$ MPa	$\sigma_{z,max}^{bottom} = 0.69$ MPa
Pillar 3	$\sigma_{z,max}^{top} = 1.56$ MPa	$\sigma_{z,max}^{bottom} = 1.28$ MPa
Pillar 4	$\sigma_{z,max}^{top} = 2.12$ MPa	$\sigma_{z,max}^{bottom} = 1.69$ MPa
Pillar 5	$\sigma_{z,max}^{top} = 1.02$ MPa	$\sigma_{z,max}^{bottom} = 0.67$ MPa
Pillar 6	$\sigma_{z,max}^{top} = 1.05$ MPa	$\sigma_{z,max}^{bottom} = 0.68$ MPa
Pillar 7	$\sigma_{z,max}^{top} = 2.09$ MPa	$\sigma_{z,max}^{bottom} = 1.65$ MPa
Pillar 8	$\sigma_{z,max}^{top} = 1.59$ MPa	$\sigma_{z,max}^{bottom} = 1.31$ MPa
Pillar 9	$\sigma_{z,max}^{top} = 1.09$ MPa	$\sigma_{z,max}^{bottom} = 0.66$ MPa
Pillar 10	$\sigma_{z,max}^{top} = 1.63$ MPa	$\sigma_{z,max}^{bottom} = 1.31$ MPa
G10 - base	$\sigma_{z,max} = 0.15$ MPa	
G10 – FR4	$\sigma_{z,max} = 0.03$ MPa	
FR4 - base	$\sigma_{z,max} = 0.46$ MPa	

Table 15. The maximal σ_z values at each different location.

5.2.3. COMPARISON OF RESULTS FROM THE TENSILE TEST AND THE VIBRATION SIMULATION

To emphasize again, the comparison of the “static” and the “dynamic” results are not exactly appropriate and I only rely on the conservative approach to connect the tensile test and the random vibration analysis. Table 16 shows the comparison and the safety factor for each connection. The G10 and the FR4 are quite similar materials thus the epoxy – base plate result can be used from the tensile test to both cases. For the pillars the most dangerous is taken into account.

Connection	Tensile strength [MPa]	Stress from vibration [MPa]	Safety factor
G10-base plate	$\sigma_m = 1.47$ MPa	$\sigma_{rv} = 0.15$ MPa	$n = 9.8$
FR4-base plate	$\sigma_m = 1.47$ MPa	$\sigma_{rv} = 0.46$ MPa	$n = 3.2$
Pillar-base plate	$\sigma_m = 5.7$ MPa	$\sigma_{rv} = 2.12$ MPa	$n = 2.7$

Table 16. The comparison of the results from tensile test and the vibration simulation.

Considering that the maximal stresses from the vibrations occurs only with very small percentage and even safety factor remains, the chambers can be transported without a problem, of course with the correct packaging.

6. SUMMARY

While writing this thesis, I had the opportunity to continue my work with the Innovative Particle Detector Development Research Group of the Eötvös Loránd Research Network, Wigner RCP, Institute for Particle and Nuclear Physics. My thesis aims to investigate further the development and different kind of limits of a special type gaseous detector the Multi-Wire Proportional Chamber (MWPC).

The objective of my research can be divided into two different parts. First to give a quantitative approximation for the effects of the environmental parameters (temperature, pressure) and a method to distinguish these effects from each other. Currently 10 modules of MWPCs are working in Japan near the Sakurajima volcano at the Sakurajima Muon Observatory along with other types of detectors. When there are extreme conditions (high temperature, high humidity) the gain of each chamber can drastically change which results decreased tracking efficiency. My goal was to build a measurement setup that can imitate these conditions with controlling and the effect of different parameters can be separated. The second part concentrates on the random vibration phenomenon during the transportation of these detectors. The construction of these chambers uses a two component epoxy adhesive to keep the gas volume together. The main question that I attempt to investigate is the following: Can the bonded joints withstand the stresses from the vibrations resulted from the transportation? In the meantime of my research I discovered a “tempering” effect of the chambers after each cycle of heating and cooling and an asymmetric behaviour of the adhesive while applying different mixing ratios.

In the first part of the dissertation I provide some insight into the work of Japanese and Hungarian scientists about the imaging techniques with cosmic-rays. In the second section I introduce the main principles of muography and the reason behind our collaboration with the Earthquake Research Institute focusing on the study of volcanos. After that I describe in detail our cosmic muon detectors and its construction. In

the third chapter the effect of the environmental parameters are discussed with the properties and behaviour of the gain in these kind of detectors. I show the measurements with the two different heat boxes and the results including the corrections and the “tempering” effect. In the fourth section I describe the basic properties of the adhesives and test five different glues with tensile testing along the currently used one. With the premade specimens I measure the tensile strength corresponding to the normal and shear stress for each adhesives, after that I test our current glue with different mixing ratios where I discover an asymmetric effect on the tensile strength. In the last measurement I use the proper ratio and our glue between different materials and summarise the tensile strength at each case. In the last part I present the modal testing of one chamber and with that I am able to validate my finite element simulation. After that I make the random vibration analysis with a quite conservative approach to identify the maximal stresses. Finally I compare the results from the tensile testing with the simulation relying on the conservative assumption.

6.1. Outlook

After some upgrade, the heat box can be used to simulate the effect of humidity to the system also. Our measurements near the Sakurajima volcano showed that above 90% humidity the efficiency of the detectors can drop rapidly. For the proper current correction it would be reasonable to measure the current separately due to the different behaviour of each chamber. This would result a better total correction. It will be interesting to investigate further the discovered “tempering” effect with newly constructed chambers and later adapt some kind of heat treatment step into the detector building process. As for the random vibration, a fatigue test of one chamber would be reasonable to check the endurance limit of the adhesive. Also some detailed impact test that was not part of this thesis would be useful.

7. ÖSSZEFOGLALÁS

A diplomaterv elkészítése során lehetőségem nyílt folytatni a munkám a Wigner Fizikai Kutatóközpont, Innovatív Detektorfejlesztő kutatócsoporttal. A témám a gáztöltésű detektorok egy speciális fajtájával foglalkozik amelyet Sokszálas Proportionális Kamrának neveznek. Tovább folytatva az eszköz fejlesztését két részre osztható a munkám. Egyrészt hogy egy kvalitatív becslést adjak a gain környezeti paramétereiktől (hőmérséklet,nyomás) való függésére és ezek az effektusok egymástól elválaszthatók legyenek. Ezeket a hatásokat tapasztaljuk a Sakurajima vulkán melletti mérőállomáson Japánban ahol 10 ilyen rendszer mér jelenleg is és az extrém hőmérséklet és páratartalom csökkentheti az érzékelési hatásfokot. Céлом egy mérési rendszer létrehozása volt amely hasonló körülményeket teremthet és a detektorok tesztelhetők benne. A másik részben a véletlenszerű rezgések okozta hatást vizsgálom amely az eszközök szállítása során lép fel. A detektorok egyes részeit két komponensű epoxy ragasztóval rögzítjük egymáshoz, hogy a kamrát mechanikailag egyben tartsuk és a gázzárást biztosítsuk. A dolgozat fő kérdése amelyet vizsgáltam, hogy vajon ezek a ragasztott kapcsolatok ellen tudnak e állni a szállításból adódó véletlen rezgéseknek? A mérések során felfedeztem néhány különleges jelenséget mégpedig, hogy a kamrák "edződnek" minden egyes felmelegítés és lehűtés után, illetve a ragasztó arány elrontásával asszimmetrikus gyengülés következik be és nem mindegy, hogy melyik komponensből van több. Az első részben a korábbi képalkotó kísérleteket mutatom be amelyet magyar és japán kutatók végeztek. Ezután a müográfia alapjait, a nemzetközi kollaborációnkat és eszközünket mutatom meg. A harmadik részben definiálom a gain függését a környezeti paramétereiktől és részletezem a különböző méréseket. Ezután a ragasztók szakítóvizsgálata következik. A végén pedig elvégzem a kamra modális analízisét amellyel validálom a szimulációt és meghatározom a maximális feszültségeket amelyek a véletlen rezgésből fakadnak. Végül összevetem a szakítást a szimulációval a konzervatív megközelítésre alapozva.

8. REFERENCES

1. V.F.Hess: Penetration radiation in seven free ballon flights, PZ,13, (1912)
2. Luis W. Alvarez: Search for Hidden Chambers in the Pyramids, Science vol 167., 1970
3. Street, J.: Stevenson,E.: New evidence for the Existence of a Particle of Mass Intermediate Between the Proton and Electron, Physical Review. 52(9):1003 (1937)
4. K. Nagamine et al.: Method of probing inner-structure of geophysical substance with the horizontal cosmic-ray muons and possible application to volcanic eruption prediction
5. H. Tanaka et al.: Development of a two-fold segmented detection system for near horizontally cosmic-ray muons to probe the internal structure of a volcano, NIM PR A 507 657-669, (2003)
6. H. Tanaka et al.: Radiographic measurement of the internal structure of Mt. West Iwate with near-horizontal cosmic-ray muons and future developments, NIM PR A 555 164-172 (2005)
7. H. Tanaka et al.: Development of an emulsion imaging system for cosmic-ray muon radiography to explore the internal structure of a volcano, Mt. Asama, NIM PR A 575 489-497, (2007)
8. H. Tanaka, T. Uchida, M. Tanaka, H. Shinohara, H. Taira: Cosmic-ray muon imaging of magma in a conduit: Degassing process of Satsuma-Iwojima Volcano, Japan, Geophysical Research Letters Vol. 36 Issue 1, (2009)
9. F.Sauli (1977): Principles of operation of multiwire proportional and drift chambers. Cern, Geneva
10. R&D Proposal: Development of Micro-Pattern Gas Detectors Technologies, RD51 2008-001 (2008)
11. T.Nakamura, et al., NIM PR A 556 80, (2006)

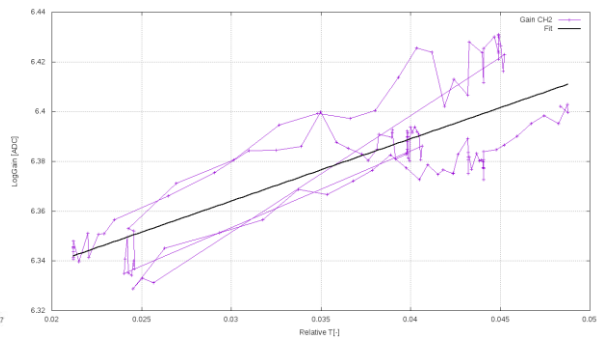
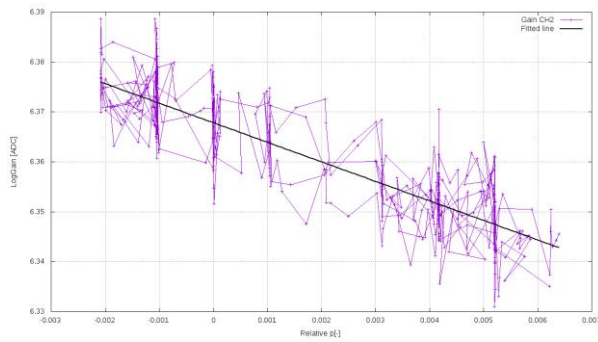
12. D.Varga, G.Hamar, G.Kiss: Asymmetric Multi-Wire Proportional Chamber with reduced requirements to mechanical precision, NIM PR A 648 163-167, (2011)
13. D.Varga, G.Surányi, L.Oláh, H.G.Meleg, G.Hamar, G.G.Barnaföldi: Portable cosmic muon telescope for environmental applications, NIM PR A 689 60-69, (2012)
14. D.Varga, Z.Gál, G.Hamar, J.S.Molnár, É.Oláh, P.Pázmándi: Cosmic Muon Detector Using Proportional Chambers, European Journal of Physics, Vol. 36, N 6, (2015)
15. P.K.F. Grieder: Cosmic Rays at Earth Elsevier (2001)
16. H.K.M. Tanaka, D.Varga, et al., Muographic Observation Instrument Japan/EU/PCT patent, ref 2016-087436 PCT/IB2017/052303, priority date 25/04/2016
17. L.Oláh, H.K.M. Tanaka, T.Ohminato, D.Varga: High-definition and low-noise muography of the Sakurajima volcano with gaseous tracking detectors, Scientific Reports 8, 3207(2018)
18. D.Varga, G.Nyitrai, G.Hamar, L.Oláh: High efficiency gaseous tracking detector for cosmic muon radiography, Hindawi Publishing Corporation, Advances in High Energy Physics, Volume 2016 , Article ID 1962317
19. Á.L.Gera: Proporciónális detektorok mechanikai struktúrájának optimalizálása, BSc thesis, University of Technology and Economics, Faculty of Mechanical Engineering, Department of Applied Mechanics (2017)
20. G. Nyitrai: Nagy felbontású minőség-ellenőrző rendszer részecskedetektorokhoz, BSc thesis, University of Technology and Economics, Faculty of Mechanical Engineering, Department of Applied Mechanics (2015)

21. D.Varga, G.Nyitrai, G.Hamar, G.Galgóczi, L.Oláh, H.K.M. Tanaka, T.Ohminato: Detector developments for high performance Muography applications, NIM PR A (2019), <https://doi.org/10.1016/j.nima.2019.05.077>.
22. D.Varga, G.Nyitrai, G.Hamar, A.Gera, L.Oláh, H.K.M. Tanaka: Tracking detector for high performance cosmic muon imaging, Journal of Instrumentation (2020), JINST 15 C05007
23. Sz.Balogh: Müöntomográfok kültéri hálózatának előkészítése vulkanikus tevékenység monitorozásához, MSc thesis, Széchenyi István University, Faculty of Electrical Engineering (2015)
24. L.Oláh: Research and Development of Particle Detectors for Muon Tomography and the CERN ALICE Experiment, PhD thesis, Eötvös Loránd University Doctorate School of Physics, Particle Physics and Astronomy Program, (2016)
25. M.E. Rose, S.A. Korff: An Investigation of the Properties of Proportional Counters, Phys. Rev. 59, 850. (1941)
26. W. Diethorn: A methane proportional counter system for natural radiocarbon measurements, NYO-6628 (1956)
27. A. Williams, R.I. Sara: Parameters affecting the resolution of a proportional counter, Int. J. Appl. Rad. Isotopes 13 229 (1962)
28. A. Zastawny: Gas amplification in a proportional counter with carbon dioxide, J. Sci. Instr. 43 179 (1966)
29. M.W. Charles: Gas gain measurements in proportional counters, J. Phys. E 5 95. (1972)
30. T. Aoyama: Generalized gas gain formula for proportional counters, NIM PR A 234 125-131 (1985)
31. W.Blum, L.Rolandi: Particle detection with drift chambers, Springer-Verlag (1994)

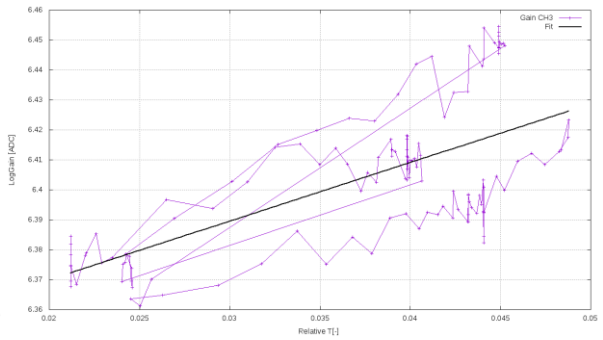
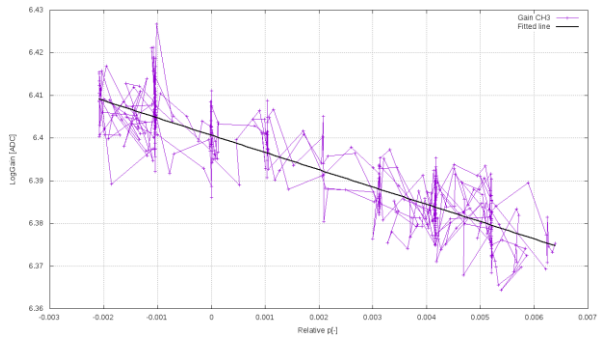
32. A. von Engel: Ionization in gases by electrons in electric fields, Handbuch der Physik, Vol 21, Springer, Berlin Heidelberg (1956)
33. F.Ferenc, F.J.Ferenc: A ragasztás kézikönyve, Műszaki Könyvkiadó, Budapest (1997)
34. Gy.Balázs: Ragasztástechnika, Műszaki Könyvkiadó, Budapest (1982)
35. Technical manual of the UVERAPID 5 two component epoxy adhesive
<http://www.uvesz.hu/IUV5M.htm>
36. Technical manual of the UVERAPID 20 two component epoxy adhesive
<http://www.uvesz.hu/IUV20M.htm>
37. Technical manual of the SikaPower - 1277 two component epoxy adhesive
https://hun.sika.com/dms/getdocument.get/3b3de052-3101-3065-a5ee-a44c14d259ed/sikapower_1277_hu2019ta.pdf
38. Technical manual of the Sikaflex - 591 PU adhesive
http://skbolt.hu/shop_ordered/3214/pic/adatlapok/M_adatlapok/flex_591_m1902.pdf
39. Technical manual of the ARALDITE 2011 two component epoxy adhesive
<http://www.farnell.com/datasheets/2879000.pdf>
40. D.J. Ewins: Modal Testing: Theory and Practice. Research Studies Press. Taunton – Somerset, (1989)
41. G.Csernák, G.Stépán: A műszaki rezgésstan alapjai, Budapesti Műszaki és Gazdaságtudományi Egyetem, Műszaki Mechanikai Tanszék, Budapest (2012)
42. Gy.Ludvig: Gépek Dinamikája, Műszaki könyvkiadó, Budapest (1973)
43. ASTM D4169-16, Standard Practice for Performance Testing of Shipping Containers and Systems, ASTM International, West Conshohocken, PA, 2016, www.astm.org, DOI: 10.1520/D4169-16

44. ASTM D4728-17, Standard Test Method for Random Vibration Testing of Shipping Containers, ASTM International, West Conshohocken, PA, 2017, www.astm.org, DOI: 10.1520/D4728-17
45. B.S.Ben, B.A.Ben, Adarsh K., K.A.Vikram, Ch.Ratnam: Damping measurement in composite materials under combined finite element and frequency response method, International Journal of Engineering Science Invention (IJESI), (2013)
46. R.Bedi, R.Sharma: Damping studies on fibre-reinforced epoxy polymer concrete using Taguchi design of experiments, International Journal of Materials Engineering Innovation 6(1), (2015), DOI:10.1504/IJMATEI.2015.069799
47. ASTM E756 -05, Standard Test Method of Measurement Vibration-Damping Properties of Materials, ASTM International, West Conshohocken, PA, 2017, www.astm.org, DOI: 10.1520/E0756-05R17
48. ISO 16940:2008: Glass in building – Glazing and airborne sound insulation – Measurement of the mechanical impedance of laminated glass, ICS: 81.040.20, (2008)

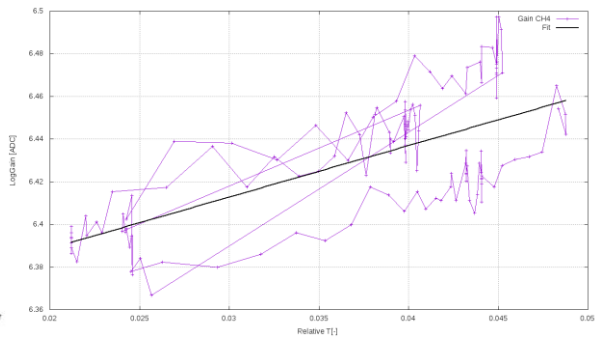
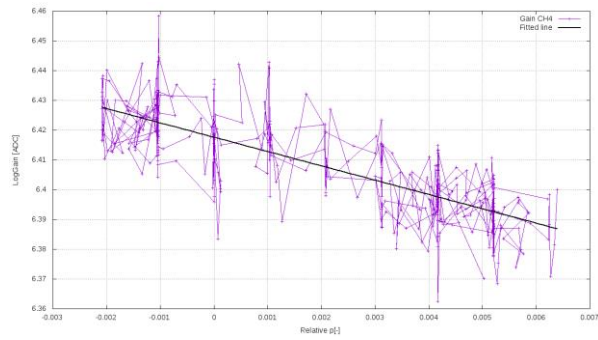
9. APPENDIX



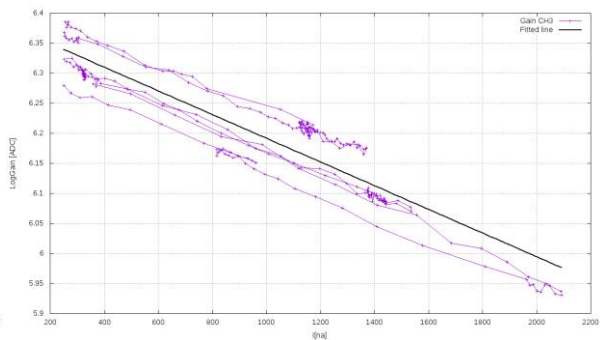
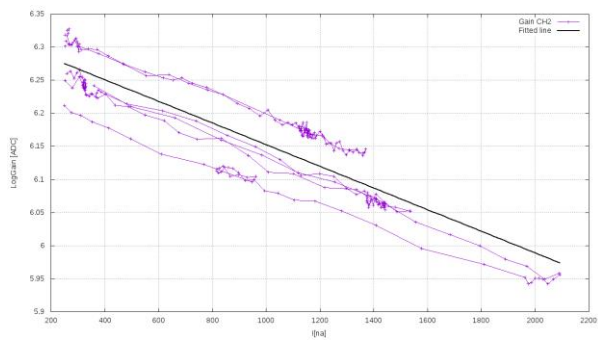
The T-p correction for chamber 2



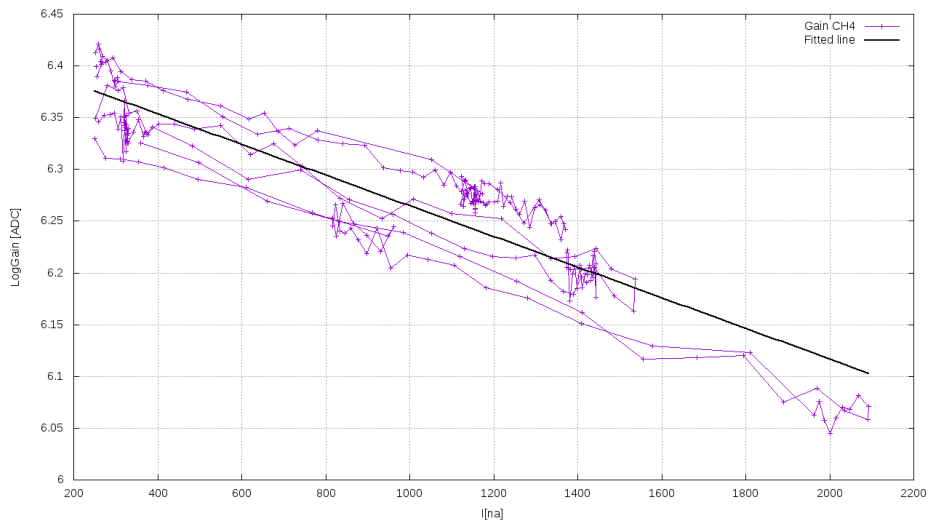
The T-p correction for chamber 3



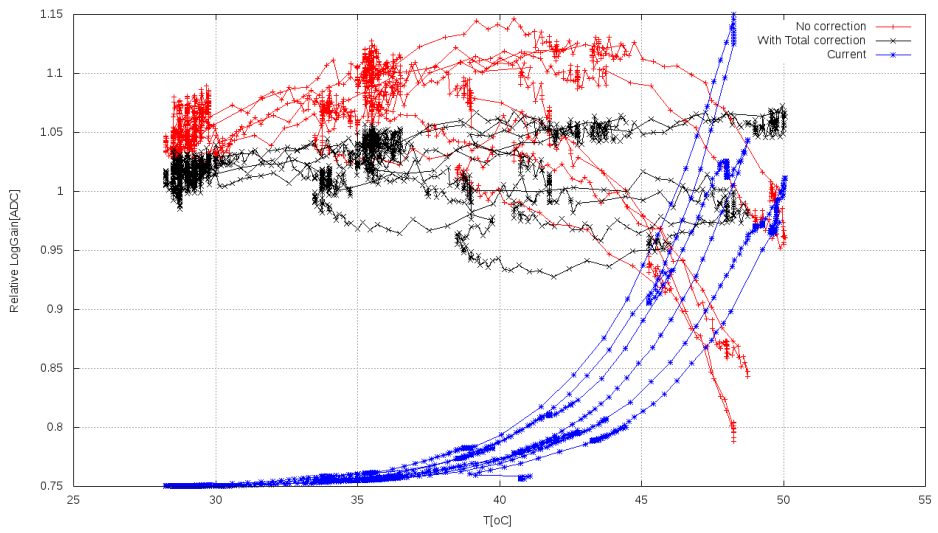
The T-p correction for chamber 4



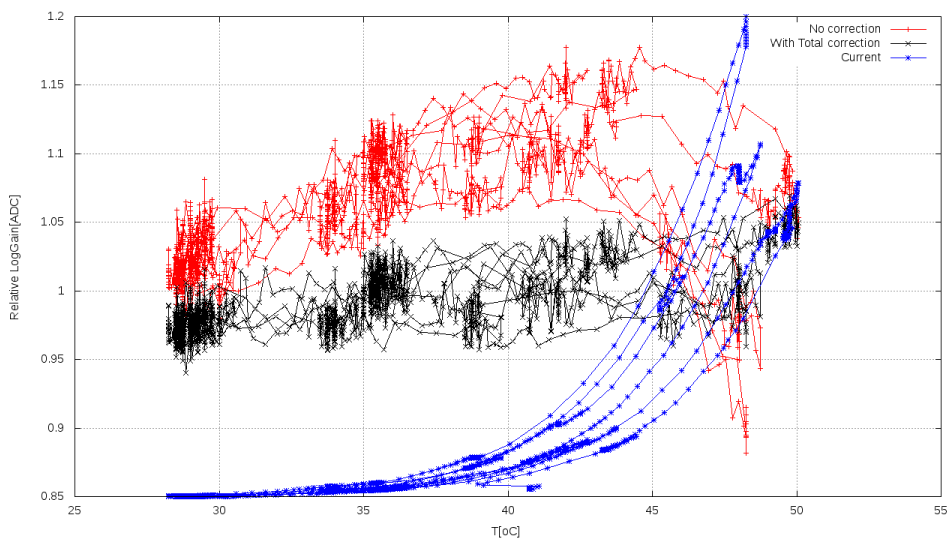
The I correction for chamber 2-3



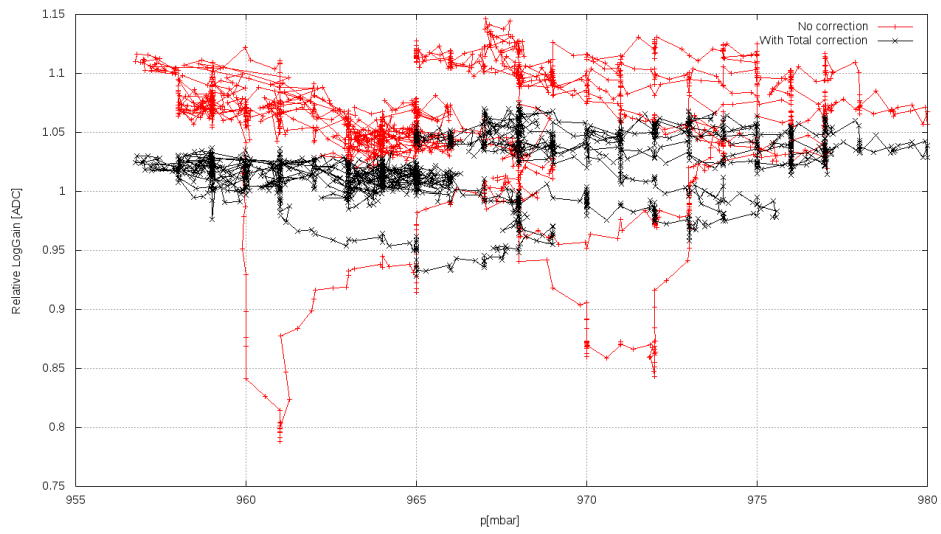
The I correction for chamber 4



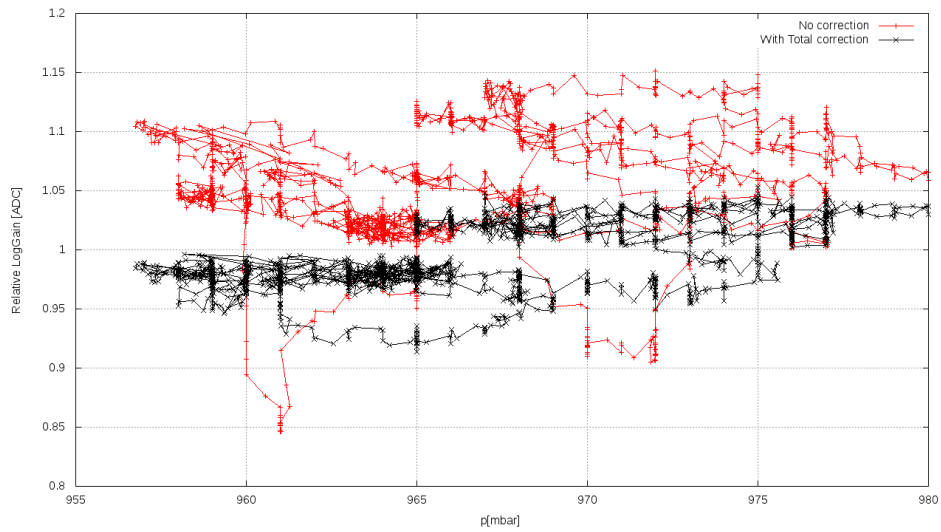
The total correction for chamber 1 as a function of temperature



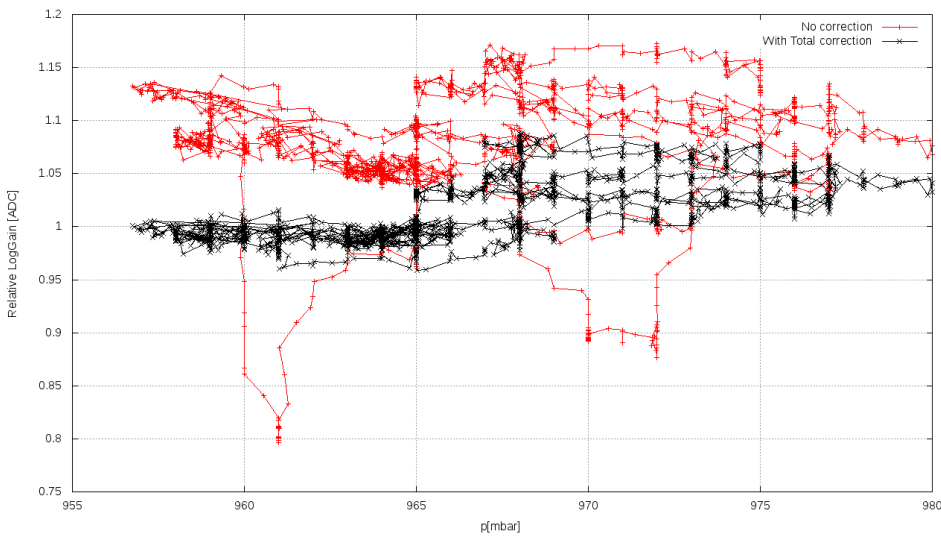
The total correction for chamber 4 as a function of temperature



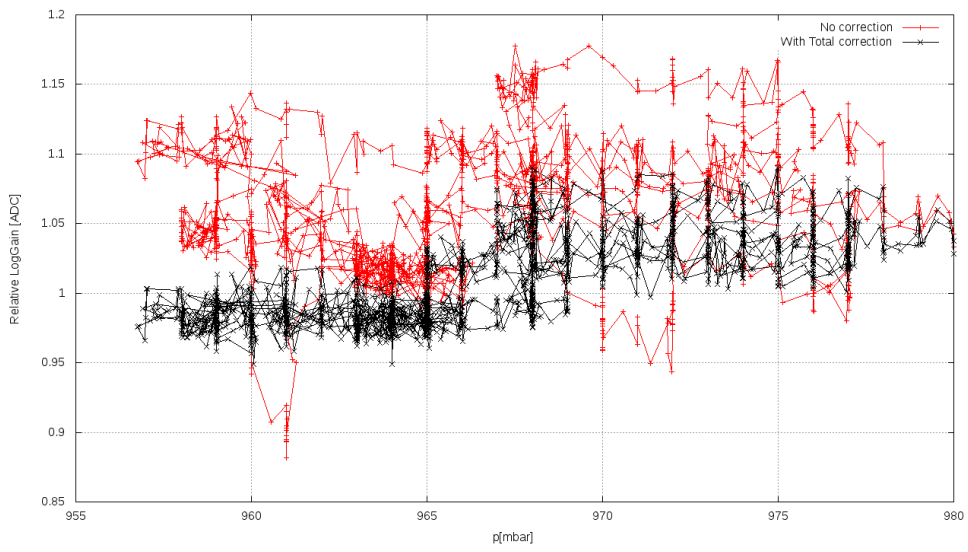
The total correction for chamber 1 as a function of pressure



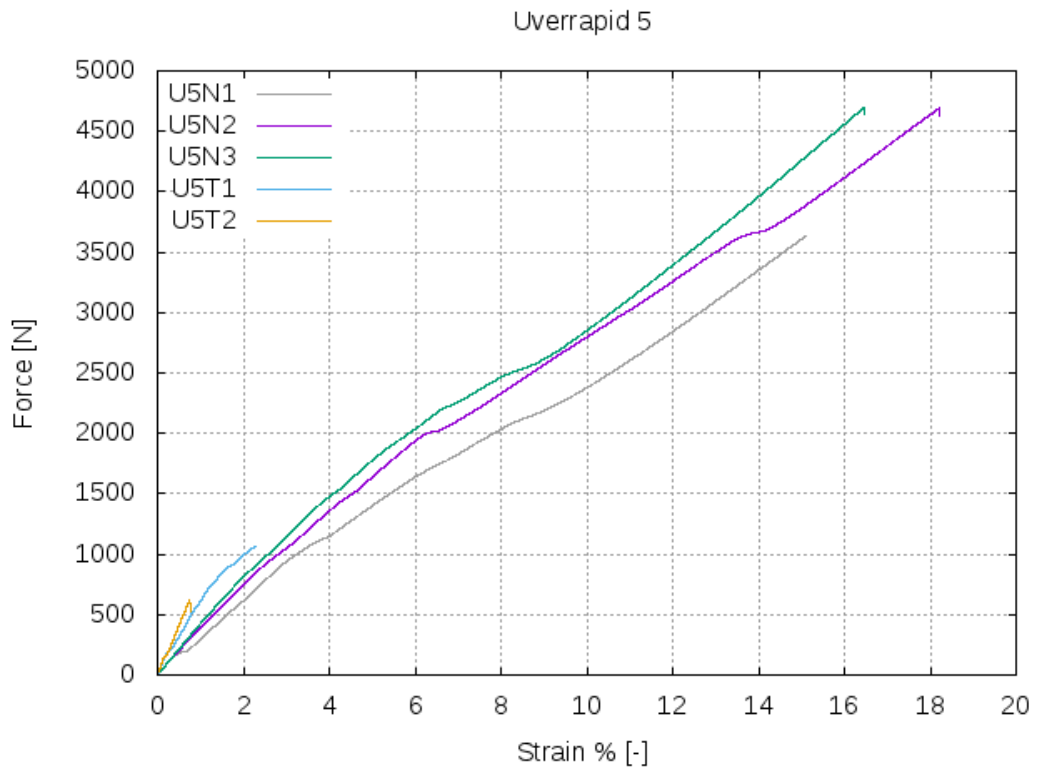
The total correction for chamber 2 as a function of pressure



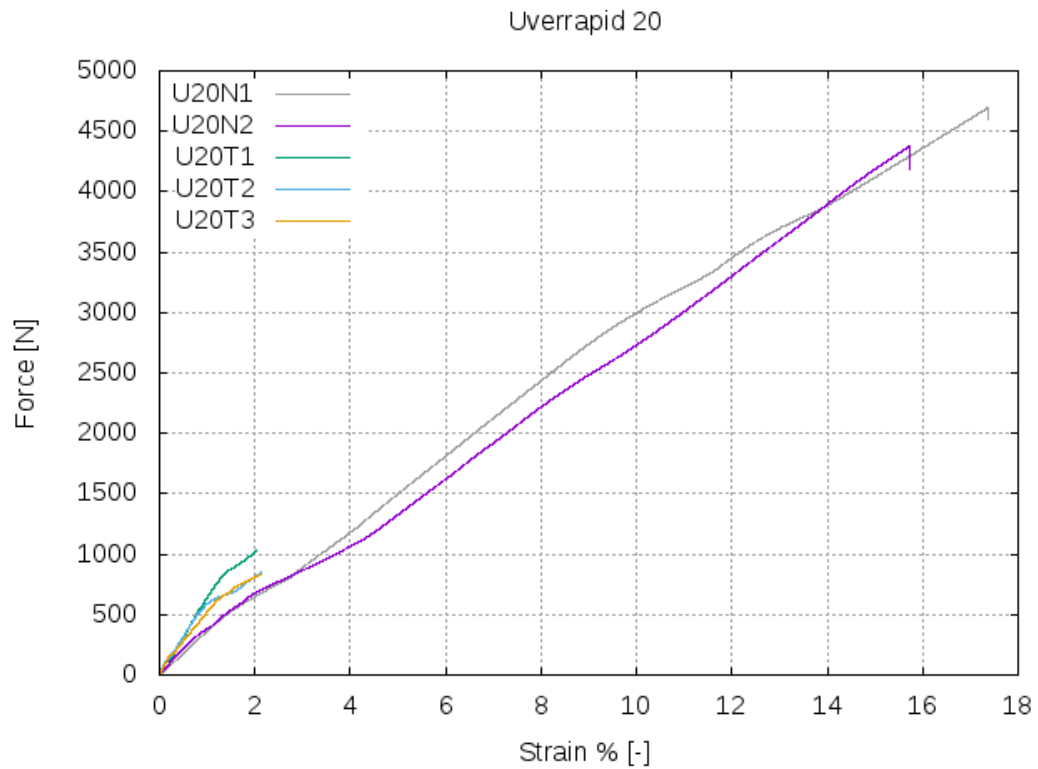
The total correction for chamber 3 as a function of pressure



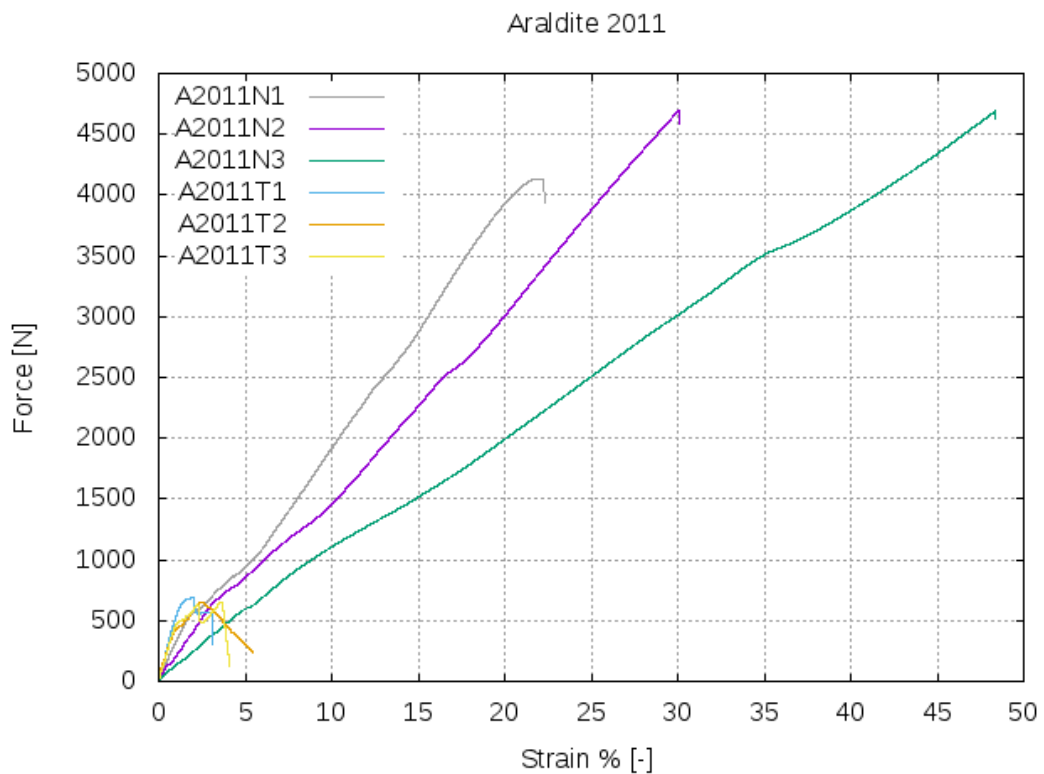
The total correction for chamber 4 as a function of pressure



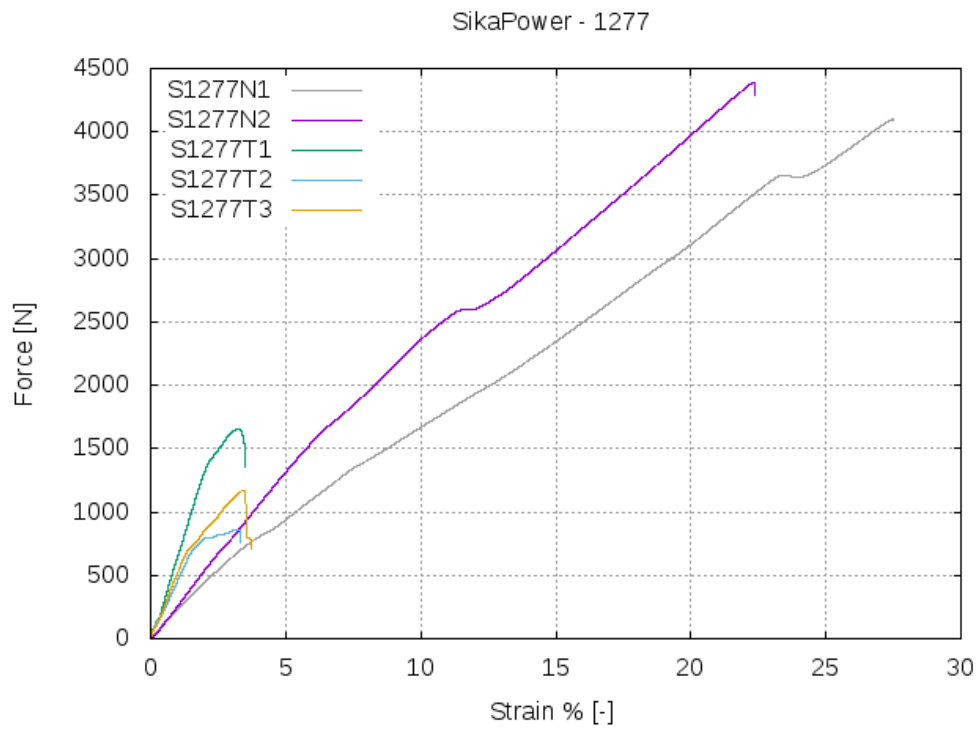
The tensile testing of UVERAPID 5 the “N” refers to the normal stress and “T” refers to the shear stress.



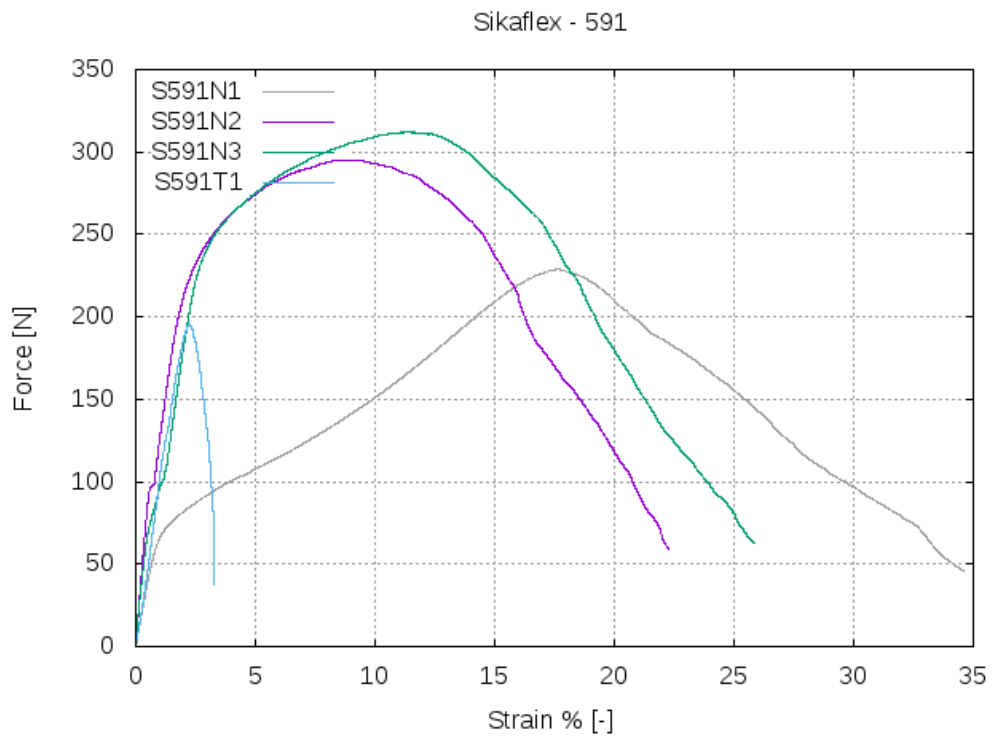
The tensile testing of UVERAPID 20 the “N” refers to the normal stress and “T” refers to the shear stress.



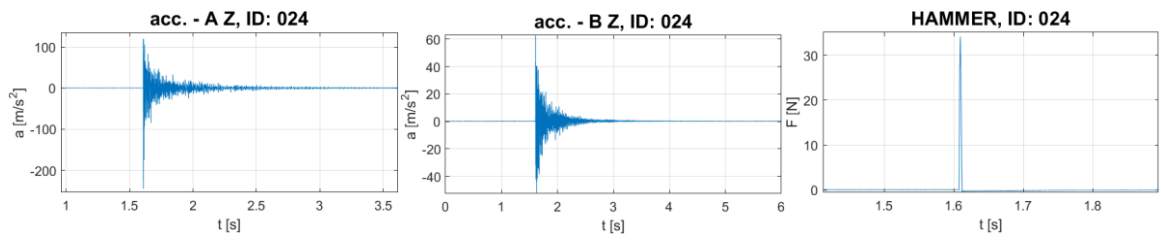
The tensile testing of ARALDITE 2011 the “N” refers to the normal stress and “T” refers to the shear stress.



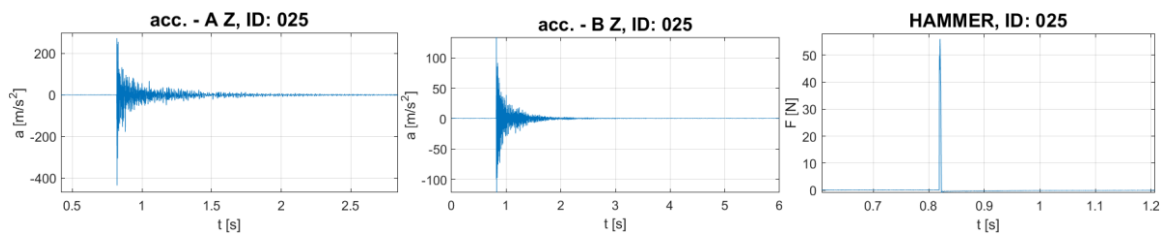
The tensile testing of SikaPower - 1277 the “N” refers to the normal stress and “T” refers to the shear stress.



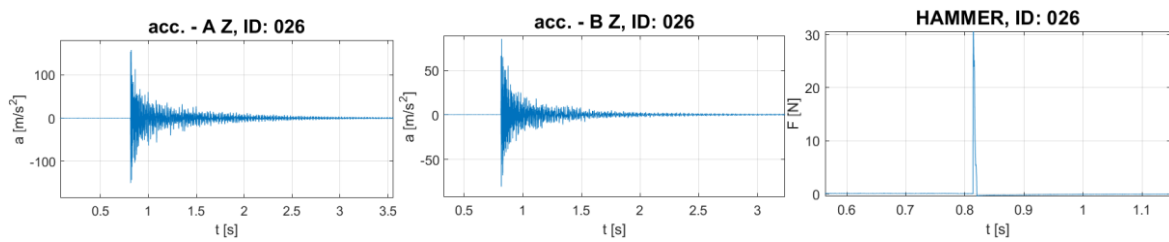
The tensile testing of Sikaflex - 591 the “N” refers to the normal stress and “T” refers to the shear stress.



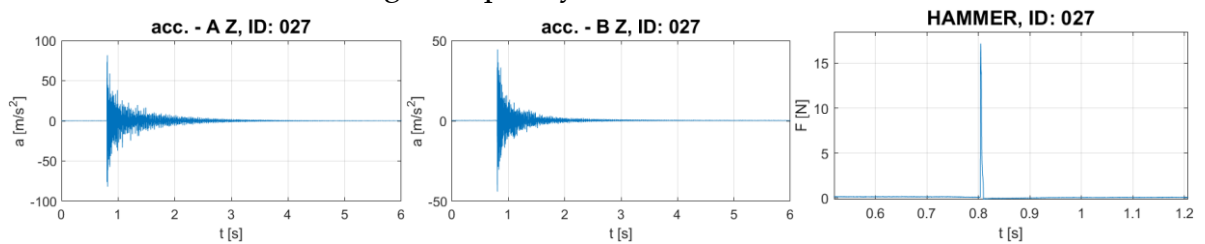
Eigenfrequency measurement ID: 24



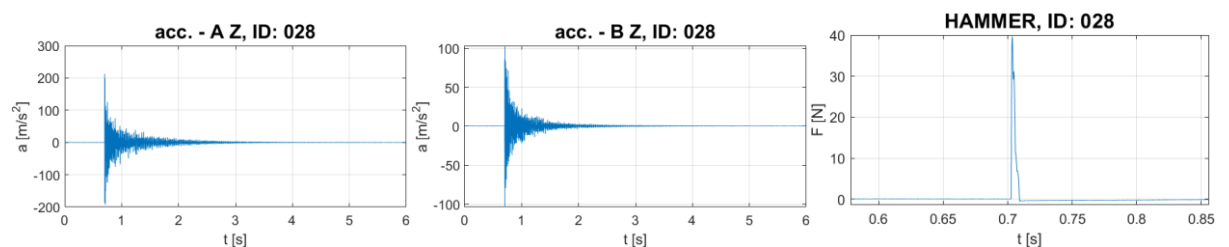
Eigenfrequency measurement ID: 25



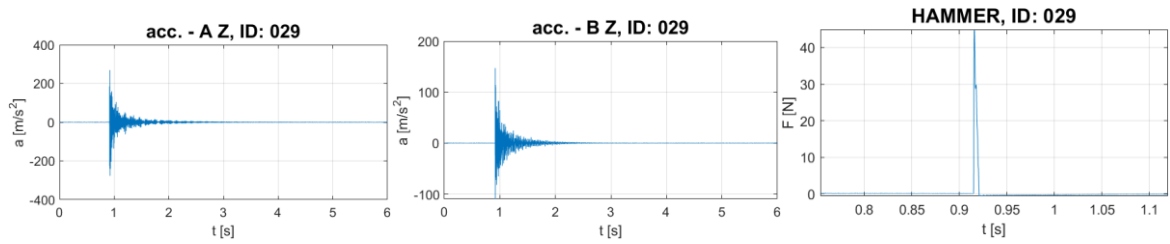
Eigenfrequency measurement ID: 26



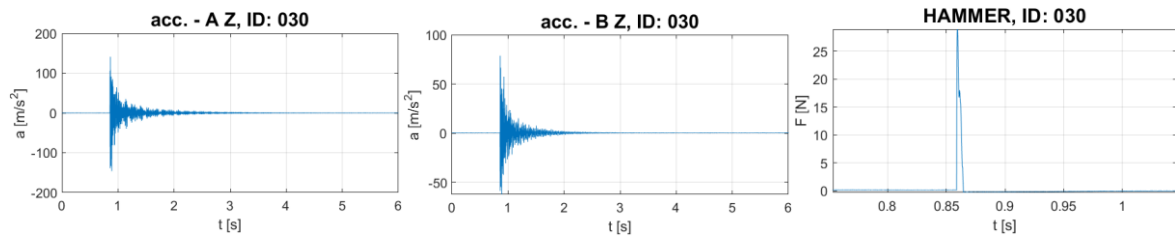
Eigenfrequency measurement ID: 27



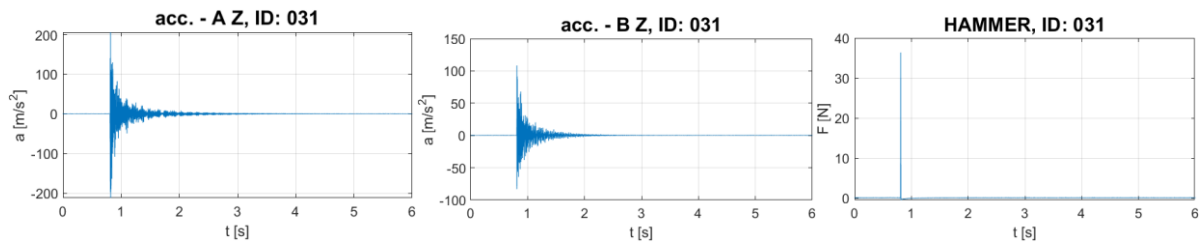
Eigenfrequency measurement ID: 28



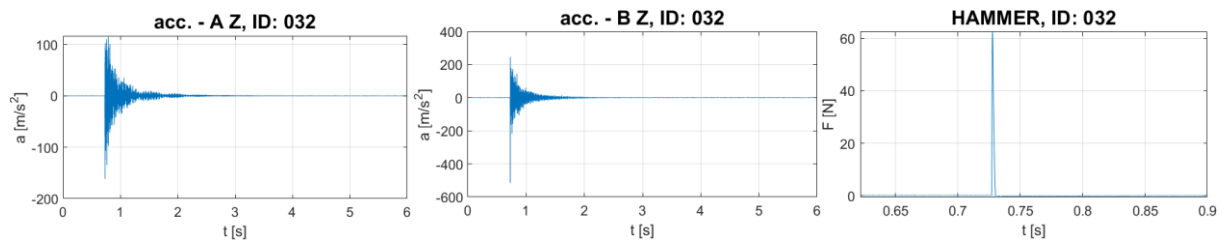
Eigenfrequency measurement ID: 29



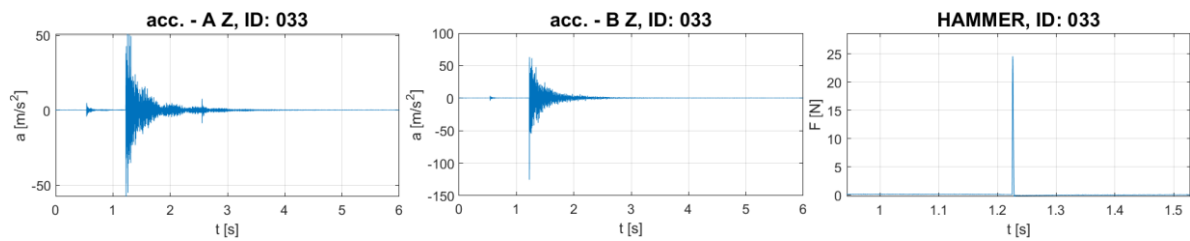
Eigenfrequency measurement ID: 30



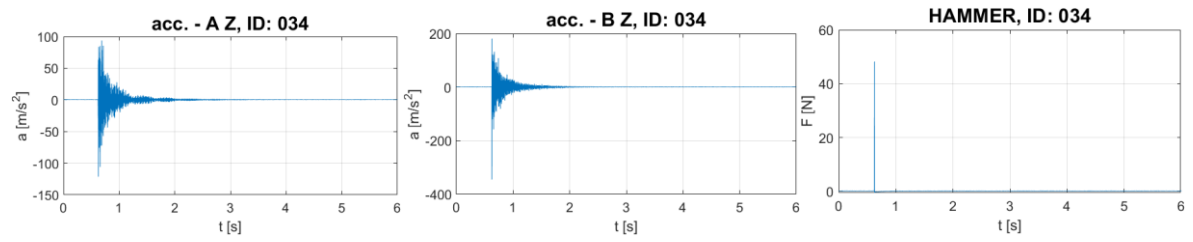
Eigenfrequency measurement ID: 31



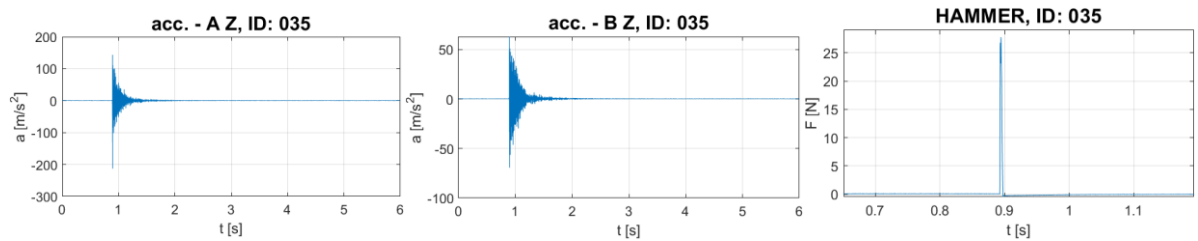
Eigenfrequency measurement ID: 32



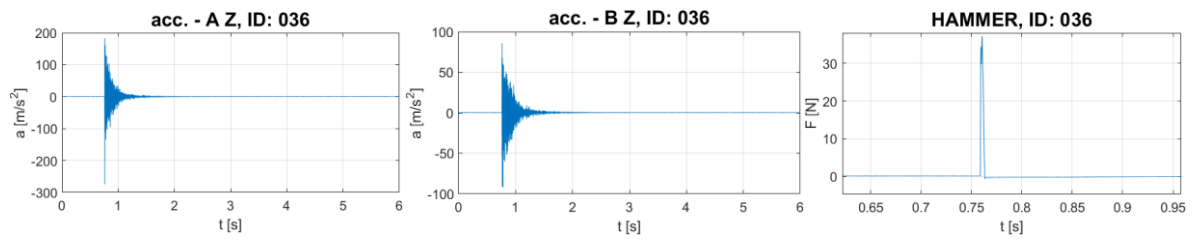
Eigenfrequency measurement ID: 33



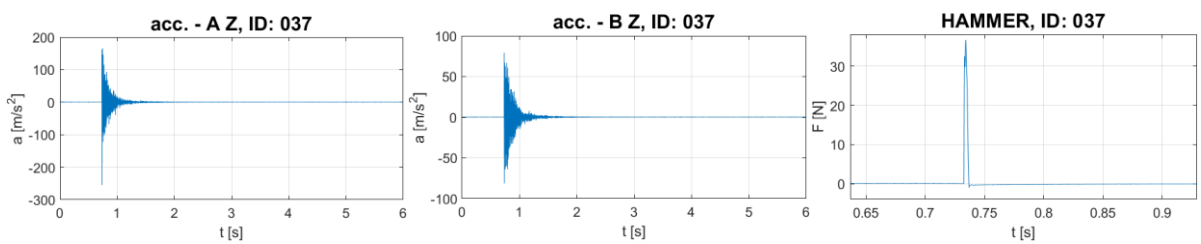
Eigenfrequency measurement ID: 34



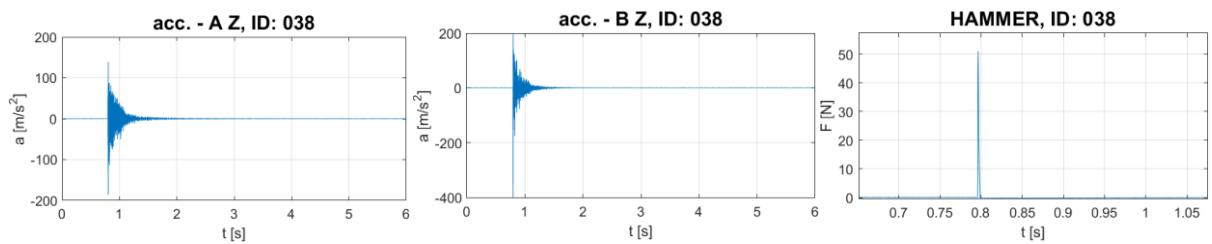
Eigenfrequency measurement with aluminium supports ID: 35



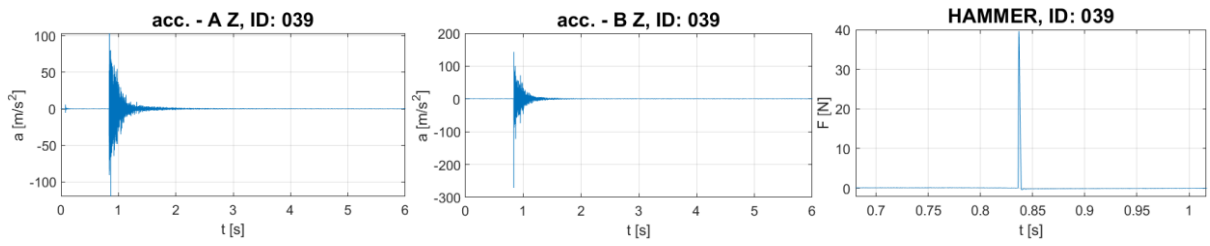
Eigenfrequency measurement with aluminium supports ID: 36



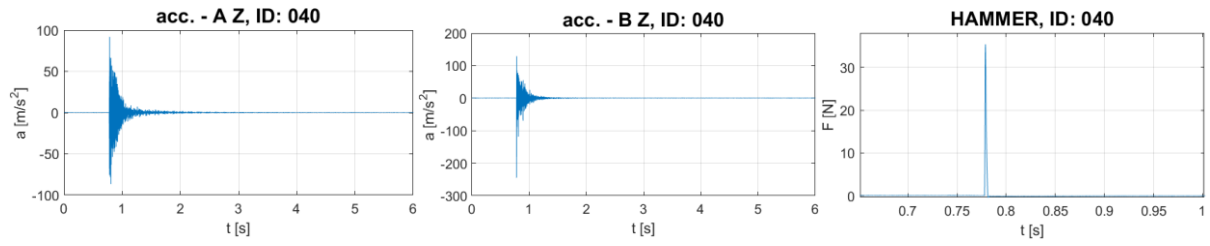
Eigenfrequency measurement with aluminium supports ID: 37



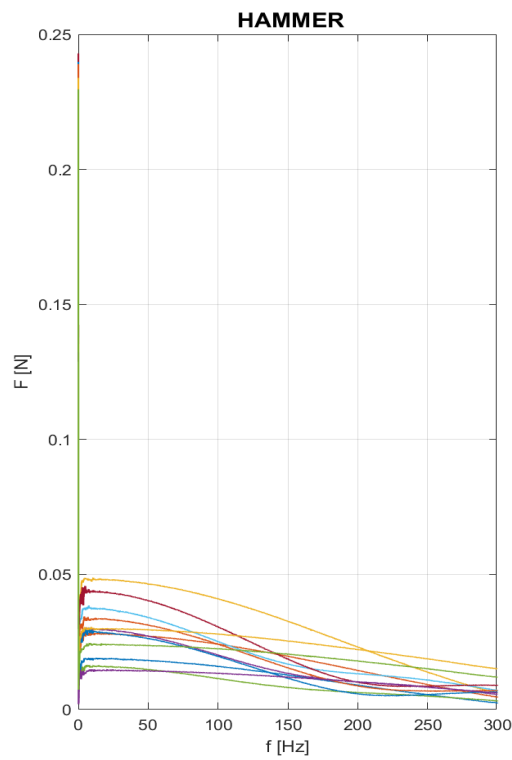
Eigenfrequency measurement with aluminium supports ID: 38



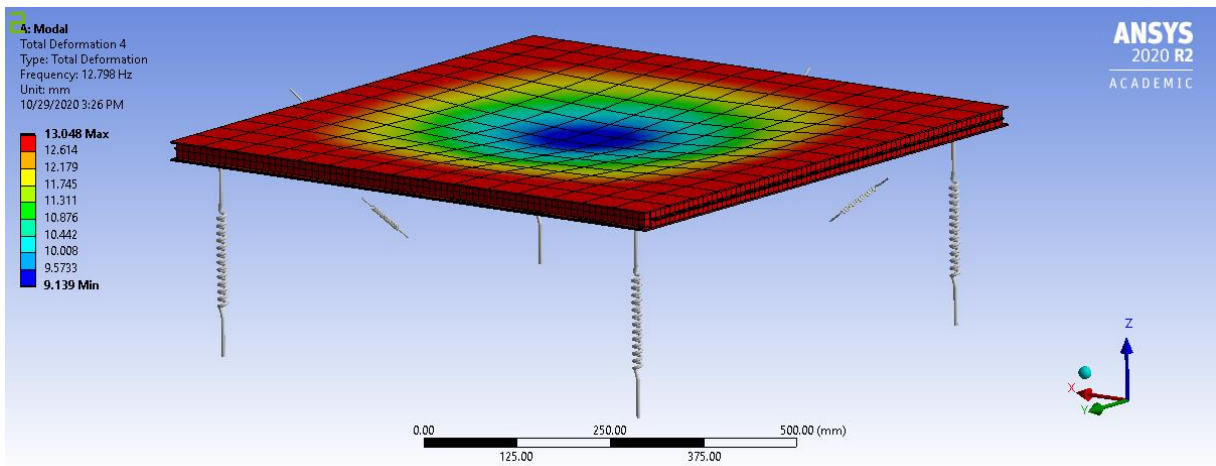
Eigenfrequency measurement with aluminium supports ID: 39



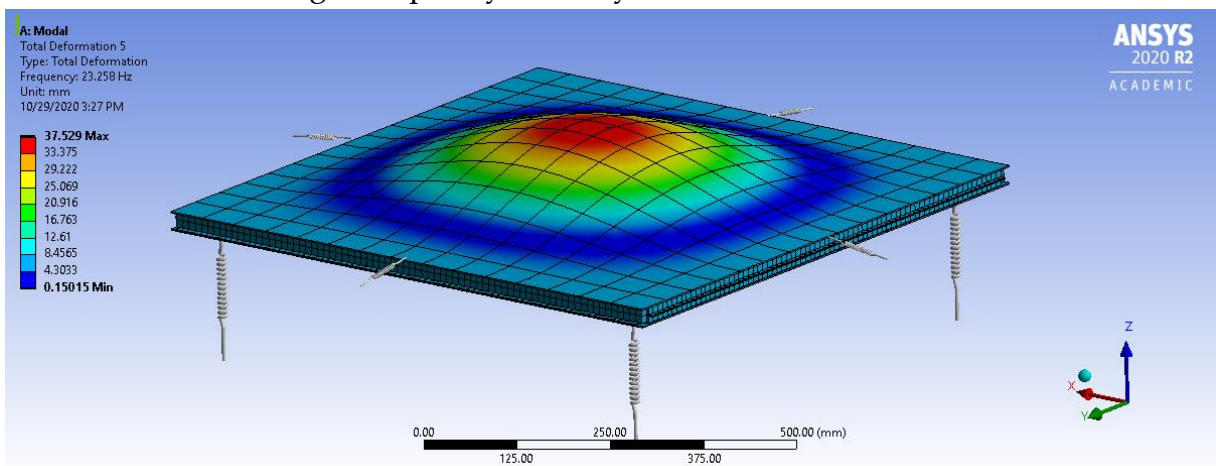
Eigenfrequency measurement with aluminium supports ID: 40



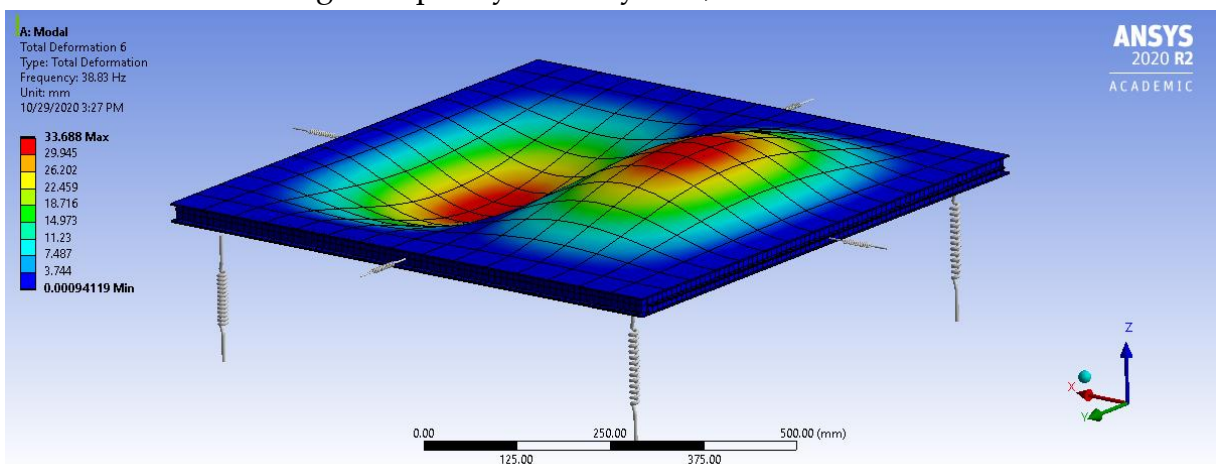
The FFT of the input signal.



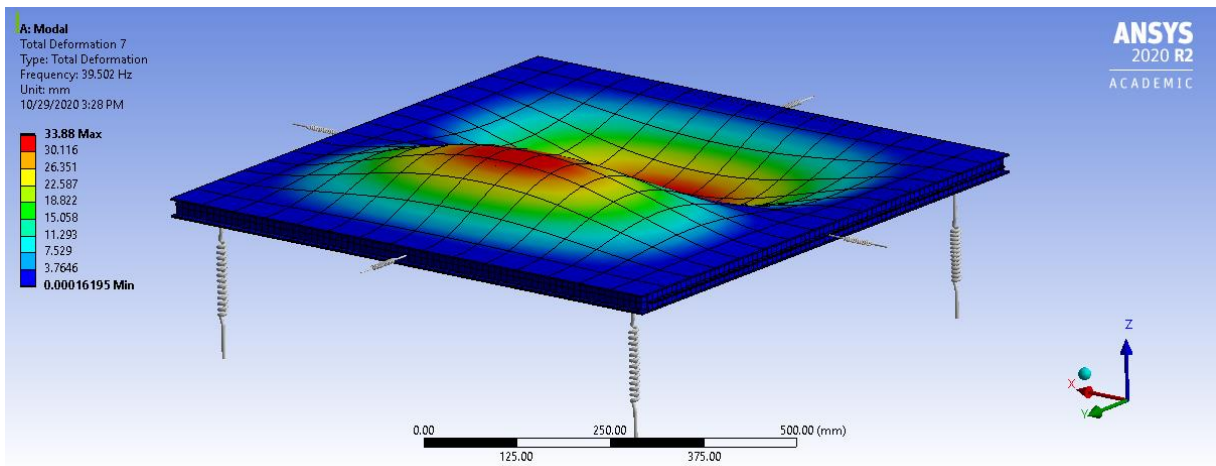
The first eigenfrequency of the system, it is related to the foams.



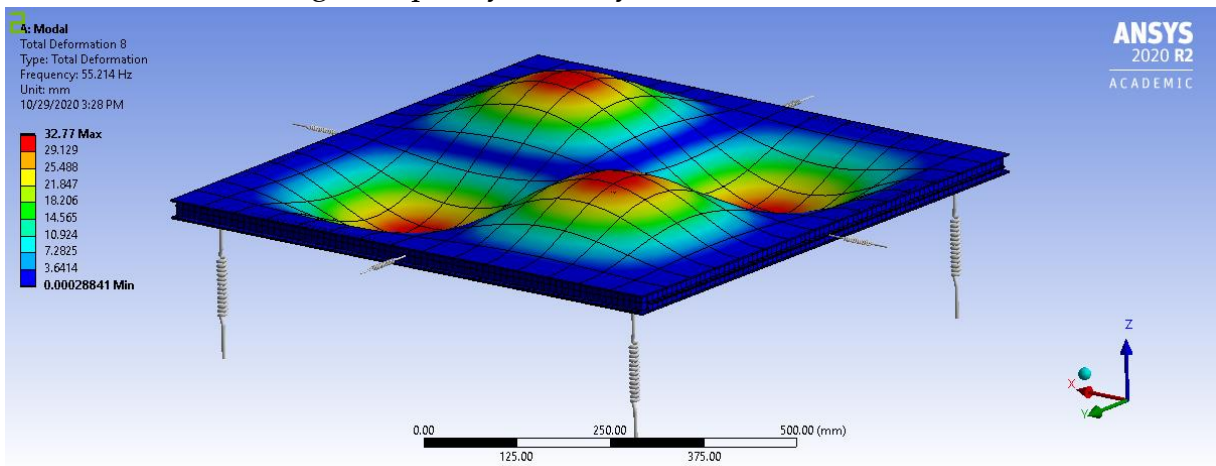
The second eigenfrequency of the system, it is related to the chamber



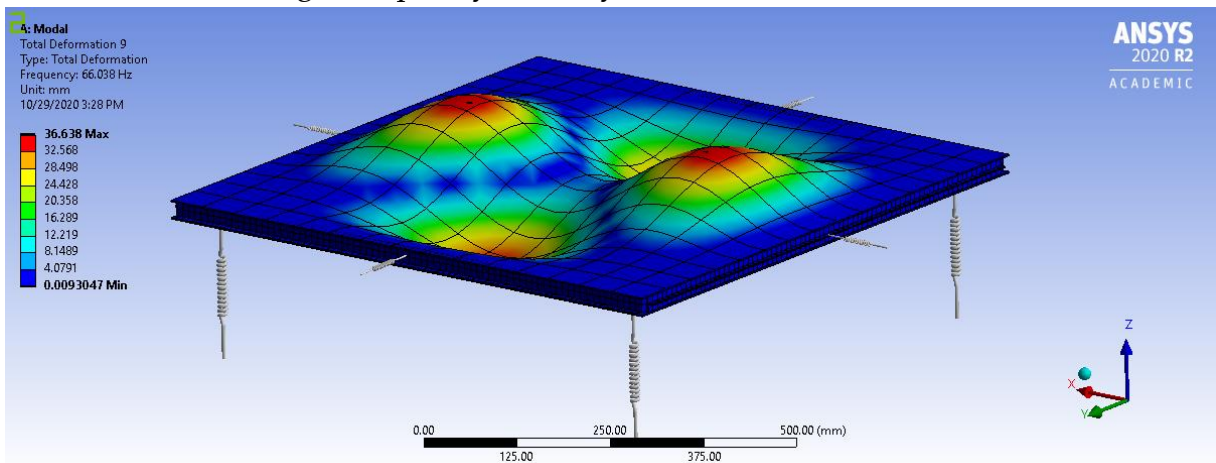
The third eigenfrequency of the system, it is related to the chamber



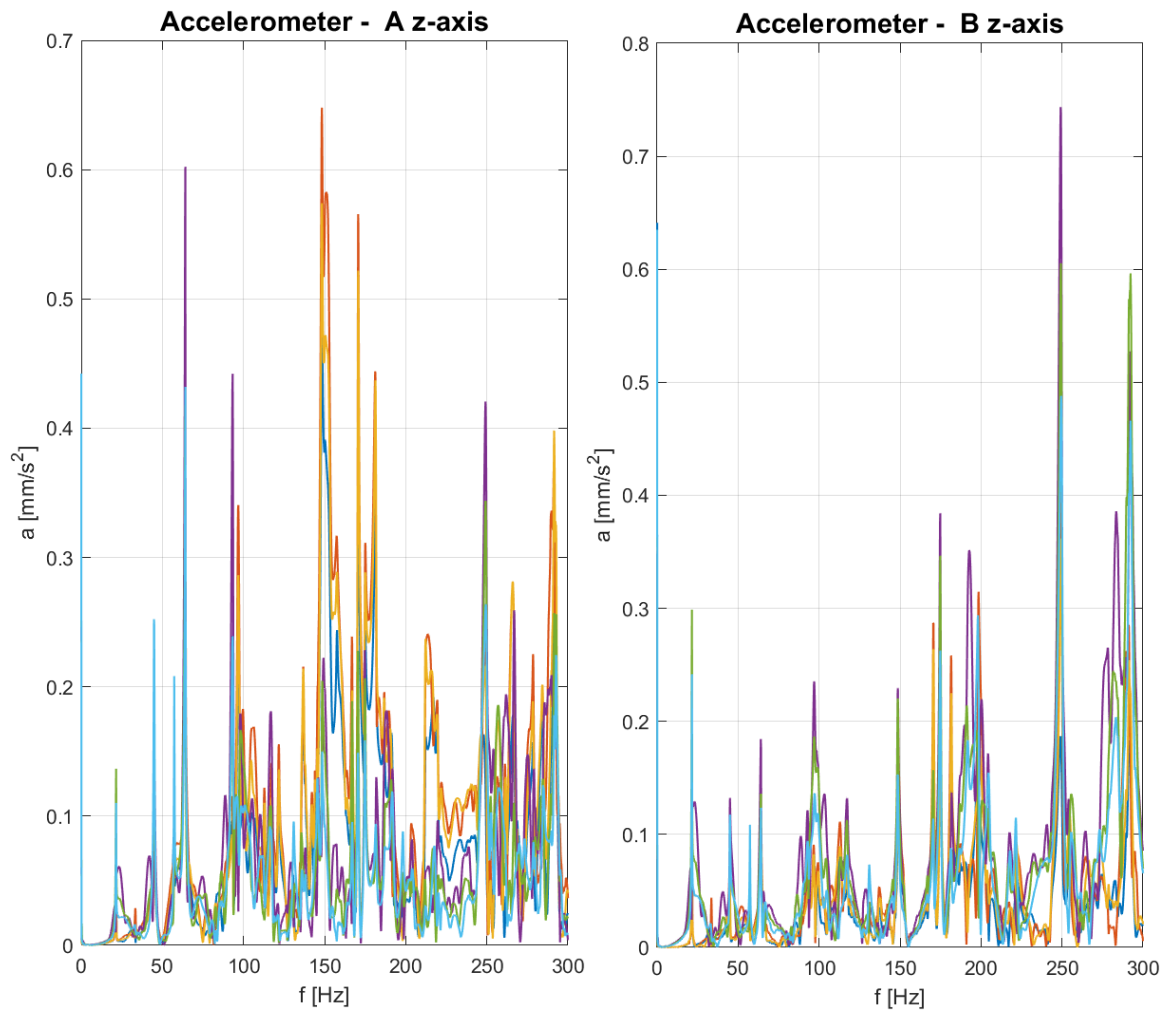
The fourth eigenfrequency of the system, it is related to the chamber



The fifth eigenfrequency of the system, it is related to the chamber



The sixth eigenfrequency of the system, it is related to the chamber



The FFT of the FRF from the modal testing with aluminium spacers